BONNER METEOROLOGISCHE ABHANDLUNGEN

Heft 66 (2014) (ISSN 0006-7156)

Herausgeber: Andreas Hense

Thorsten Simon

Statistical and Dynamical Downscaling of Numerical Climate Simulations: Enhancement and Evaluation for East Asia

BONNER METEOROLOGISCHE ABHANDLUNGEN
Heft 66 (2014) (ISSN 0006-7156)
Herausgeber: Andreas Hense

Thorsten Simon

Statistical and Dynamical Downscaling of Numerical Climate Simulations: Enhancement and Evaluation for East Asia

Statistical and Dynamical Downscaling of Numerical Climate Simulations: Enhancement and Evaluation for East Asia

Dissertation

zur

Erlangung des Doktorgrades (Dr. rer. nat.)

der

Mathematisch-Naturwissenschaftlichen Fakultät

der

Rheinischen Friedrich-Wilhelms-Universität Bonn

vorgelegt von

Thorsten Simon

aus

Nürnberg

Bonn

Juli 2014

Diese Arbeit ist die ungekürzte Fassung einer der Mathematisch-Naturwissenschaftlichen Fakultät der Rheinischen Friedrich-Wilhelms-Universität Bonn im Jahr 2014 vorgelegten Dissertation von Thorsten Simon aus Nürnberg.

This paper is the unabridged version of a dissertation thesis submitted by Thorsten Simon born in Nuremberg to the Faculty of Mathematical and Natural Sciences of the Rheinische Friedrich-Wilhelms-Universität Bonn in 2014.

Anschrift des Verfassers: Address of the author:

Thorsten Simon
Meteorologisches Institut der
Universität Bonn
Auf dem Hügel 20
D-53121 Bonn

1. Gutachter: Prof. Dr. Andreas Hense
2. Gutachter: Prof. Dr. Clemens Simmer

Tag der Promotion: 10.11.2014

Lenka
Móric
Gréta
Ava

Zusammenfassung

Das übergeordnete Ziel dieser Arbeit ist die Präsentation von Methoden, die die Evaluierung dynamischen Downscalings[1] verbessern oder statistische Downscaling Verfahren aufwerten.

Der Informationstransfer von einer grossen Skala zu einer kleinen Skala wird als Downscaling bezeichnet. Zwei unterschiedliche Ansätze werden in den Klimawissenschaften für Downscaling Zwecke verwendet: *Dynamisches Downscaling* und *statistisches Downscaling*. Um eine bessere Beschreibung der herunterskalierten Daten zu ermöglichen, werden in dieser Arbeit Methoden für beide Ansätze vorgestellt, die die Evaluierung und Interpretation der Daten und Ergebnisse fortführender Studien verbessern.

Dynamisches Downscaling basiert auf räumlich begrenzten Zirkulationsmodellen für die Atmosphäre, so genannte regionale Klimamodelle (RCM[2]). Seitliche Randbedingungen (LBC[3]) für das RCM liefert eine Klimasimulation eines globalen Zirkulationsmodells (GCM[4]). Diese Arbeit stellt Methoden zur Evaluierung von RCM Simulationen vor: Erstens wird ein eine qualitative Evaluierungsmethode, die untersucht ob spezifische Dynamiken in der Atmosphäre vom RCM aufgelöst werden, vorgestellt. Zweitens wir eine neu entwickelte Methode eingeführt, die mit Hilfe von Kreuzspektren untersucht auf welchen Zeitskalen ein RCM das Potential hat Variabilität unabhängig vom GCM, aus dem die LBC stammen, zu generieren. Dabei werden die Kreuzspektren zwischen dem RCM und einer bilinear interpolierten Version des GCM für jeden Gitterpunkt einzeln geschätzt. Beide Methoden werden veranschaulicht anhand RCM Simulationen, deren Modellgebiet Ostasien umfasst. Das RCM COSMO-CLM wurde für diesen Zweck angepasst, und mit Klimasimulationen des GCM ECHAM5 und der Re-analyse ERA-40 am Rand angetrieben. Die qualitative Evaluierung zeigt, dass sowohl Dynamiken des Sommermonsoons und des Wintermonsoons vom COSMO-CLM aufgelöst werden. Die Anaylse mittels Kreuzspektren suggeriert, dass das Potential von COSMO-CLM, zur Erzeugung von Variabilität unabhängig vom GCM, sowohl von dynamischen Merkmalen, z.B. Monsoon und Innertropische Konvergenzzone, wie auch von numerischen Modellparametern, z.B. horizontale Auflösung und Ausdehnung des Modellgebiets, abhängt.

Statistisches Downscaling basiert auf statistischen Transferfunktionen zwischen dem Modelloutput grob auflösender Klimasimulationen und lokalen Beobachtungen. Da eine Fülle statistischer Methoden für derartige Zwecke verfügbar ist, ist es von besonderer Bedeutung fallspezifisch Prediktoren zu finden, die physikalisch sinnvoll sind und so weitere Interpretationen der Ergebnisse erlauben. Die Herleitung und Anwendung solcher Prediktoren ist erläutert anhand einer statistischen Downscaling Studie für Niederschlag im Poyang Einzugsgebiet in Ost-China. Die Ja-Nein Aussage, ob der über 24 Stunden akkumulierte Regen einen bestimmten Grenzwert überschreitet, wurde von lokalen Regenmessern für die Sommermonate abgeleitet. Empirische orthogonale Funktionen (EOF) wurden für relative Vorticity auf 850 hPa und Vertikalgeschwindigkeit auf 500 hPa aus der ERA-40 Re-analyse berechnet. Beide Informationen werden mittels logistischer Regression zusammengeführt.

[1] Der Begriff des *Herrunterskalierens* ist im Deutschen nicht gebräuchlich. Das Verb *herunterskalieren* jedoch schon.
[2] *engl.* regional climate model
[3] *engl.* lateral boundary conditions
[4] *engl.* global general circulation model

Der dominierende EOF-Prediktor kann mit Störungen auf der Meso-α-skala in Verbindung gebracht werden, welche Teil der sommerlichen Monsoondynamik in der Region sind.

Es besteht eine hohe Nachfrage an herunterskalierten Daten für weiterführende Studien in Klimawissenschaften, aber auch in anderen Disziplinen. Daher sind die Entwicklung von Evaluationsmethoden zur Beurteilung der Qualität von RCM Simulationen und die Herleitung physikalisch interpretierbarer Prediktoren für statistische Downscaling Schemata wichtige Verbesserungen für Downscaling Prozesse.

Abstract

The overall aim of this thesis is to present methods, which improve evaluating dynamical downscaling approaches or enhance statistical downscaling schemes. These methods are illustrated along examples of both approaches for the East Asian region.

The transfer of information from a large scale to a smaller scale is referred to as downscaling. Two different approaches are employed in climate science for downscaling purposes, i.e. *dynamical downscaling* and *statistical downscaling*. In order to give a better description of the downscaled data, this thesis presents methods, which help evaluating and interpreting the data and results of further studies in a better way, for both approaches.

Dynamical Downscaling is based on a spatially limited atmospheric general circulation model, a so-called regional climate model (RCM). At the boundaries of the RCM lateral boundary conditions (LBC) are provided by a climate simulation performed with a global general circulation model (GCM). This thesis proposes methods for evaluating RCM simulations. First, a qualitative evaluation, that investigates whether single atmospheric dynamics are resolved by the RCM, is presented. Second, a newly developed evaluation method, that investigates by cross-spectral analysis on which temporal scales a RCM is able to generate variability independently from the GCM defining the LBC, is introduced. To this end, cross-spectra are estimated point-to-point between the RCM and a bilinearly interpolated version of the GCM defining the LBC. Both methods are illustrated along RCM simulations performed for a domain covering East Asia. The RCM COSMO-CLM has been adapted for this purpose, and was driven by climate simulations performed with ECHAM5 and the re-analysis ERA-40 at its boundaries. The qualitative evaluation shows that both summer monsoon and winter monsoon dynamics are resolved by COSMO-CLM. The cross-spectral analysis suggests that the potential of COSMO-CLM to generate variability independently from the GCM depends on both dynamical features, i.e. monsoons and inter-tropical convergence zone, and on numerical parameters, i.e. horizontal resolution and domain extension.

Statistical downscaling is based on statistical transfer functions between the output of large scale climate simulations and observations on the local scale. While an abundance of statistical methods for this kind of purpose are available, it is crucial from case to case to find physically meaningful predictors, which allow further interpretations of the results. Deriving and applying such predictors is demonstrated along a statistical downscaling study for precipitation properties in the Poyang catchment in Eastern China. The dichotomous variable, if 24 h accumulated rainfall exceeds a certain threshold, is taken from local rain gauges for summer. Empirical orthogonal functions (EOF) are calculated for relative vorticity at 850 hPa and vertical velocity at 500 hPa taken from ERA-40 re-analysis data. Both information are linked by logistic regression. The most dominant EOF-predictor can be associated with meso-α-scale disturbances, which are part of the summer monsoon dynamics in this region.

Downscaled data is often requested for further studies in climate science, but also in other disciplines. Thus, developing evaluation methods for assessing the quality of RCM simulations, and deriving physically interpretable predictors for statistical downscaling schemes are crucial enhancements for the downscaling procedure.

Contents

Chapter 1

Introduction

This study gives an overview about the key points, at which a meteorologist or climate scientist can contribute to the broad field of downscaling climate data. Downscaling refers to the transfer of information, i.e. precipitation, representative for relative large areas or volumes to smaller scales. Scientists from other disciplines have a high interest in high resolution climate data, in order to apply this data as input for their models. Due to these circumstances the field of downscaling can be thought of as an interface, where information is transferred from one discipline to another. This is by nature a critical point. On the one hand the developers of numerical weather models (NWP) and climate models, i.e. meteorologists together with oceanographers, etc., know about the potential pitfalls in analyzing climate data or applying climate data to further studies, and they know about the details, which current research is focused on to further develop weather and climate models. Main interest of developers is a model system producing realistic simulations. In this light, it is not only important to increase horizontal resolution, but also generating ensembles to assess uncertainties, and an improvement of parameterizations of sub-grid processes to improve model physics. On the other hand there is a demand for climate data from biologists, hydrologists and others dealing with impact of and adaptation to climate change. Inherent to users is the request for *more*, which is in the case of climate data often restricted to spatial resolution.

To close the gap between focuses of developers and demands of scientist from other disciplines methods are presented in this study that should help to communicate the inherent limitations of downscaled climate data. In the following chapters both sub-fields of downscaling climate data will be addressed, i.e. *dynamical downscaling* and *statistical downscaling*.

In the field of dynamical downscaling it is crucial to provide methods for evaluating of regional climate model (RCM) simulations. Two different evaluation approaches are discussed. First, it is shown how RCM simulations can be checked for processes of atmospheric physics related to the region of interest. This is an ad-hoc approach, and dependent on the region it might be easier or harder to employ (cf. section 3.1). Second, an objective evaluation approach is presented, which is also a contribution to the discussion about defining added value of RCM simulations. A cross-spectral analysis is employed to investigate the temporal scales, on which a RCM is potentially able to generate variability on its own and independently from the driving model (cf. section 3.2).

For the field of statistical downscaling it is shown that available statistical schemes should not be applied as black boxes. Instead, selecting physically meaningful predictors for downscaling can lead to results, which are interpretable with respect to physics typical for the region (cf. section 4.2).

The research conducted in this study and in the Appendices A, B, and C, was supported by the project *Extreme Events in the Past and Future: a Comparative Assessment for the Haihe River and Poyang Lake Basins*, which was embedded in the DFG/NSFC-joint funding programme *Land Use and Water Resources Management under Changing Environmental Conditions*. In the research proposal the key objectives of the project were defined as follows[1]:

- To analyze the behavior of extremes in the Haihe and Poyang catchment with the means of extreme value theory.
- To generate high-resolution future projections of extreme events and their uncertainties by statistical downscaling of GCM simulations directly.
- To evaluate the spatial structure of extreme events by dynamical downscaling of global climate runs using a regional climate model.
- To identify the characteristics of extremes in the future by statistical post-processing of regional climate simulations.
- To provide climate data to other projects of the research program.

The results of the first, the third, and the fourth objective are presented in this study. Objective number five will not be discussed as this is pure technical work, and not related to scientific results. The strategy for the second objective was formulated according to the spatial statistics proposed by Cooley et al. (2007). Eventually, the idea was rejected due to the low spatial density of observational data. Instead, the strategy was changed in order to assess a couple of additional questions that came up during the work on the project. These questions, which are related to evaluating regional climate simulations and generating physically meaningful predictors in statistical downscaling schemes, finally led to the research conducted in chapters 3 and 4.

A description of state-of-the-art of climate modelling is given in the next chapter. The limitations of climate models lead directly to the need for downscaling schemes (section 2.1). As the project's regions of interest are located in East China, major processes related to the climate system in East Asia are reviewed (section 2.2). An overview of the statistical methods, that build the basis for the developed techniques, is given in section 2.3.

In the dynamical downscaling chapter (chapter 3) the setup of the RCM simulations and within these a first evaluation of the monsoon dynamics is given (section 3.1). Afterwards, a new method is presented for evaluating the added value of the high resolution RCM simulations with respect

[1] PIs: Dr. Ohlwein, Prof. Dr. Simmer. The whole amount of work was split in two work packages. One post dealing with statistical downscaling was filled by Thorsten Simon, who is the author of this manuscript. The second post dealing with performing the dynamical downscaling was filled by Dr. Dinan Wang.

to the climate models (section 3.2), that provided boundary conditions for the RCM simulations, i.e. these are the runs that are downscaled dynamically. At the end of the chapter additional analyses on the simulated precipitation climate in the high resolution RCM simulations (horizontal resolution about 7 km) are presented (section 3.3). The considerations on statistical downscaling begin with preliminary analyses of the observational data in the two catchments of interest (section 4.1). Afterwards, a statistical downscaling study is presented, in which the focus is set on the selection of physically motivated predictors for local precipitation properties and their interpretation (section 4.2). At the end of this manuscript, we conclude on how the presented approaches could be extended, and what this implies for future research on both dynamical and statistical downscaling (chapter 5).

Outline:

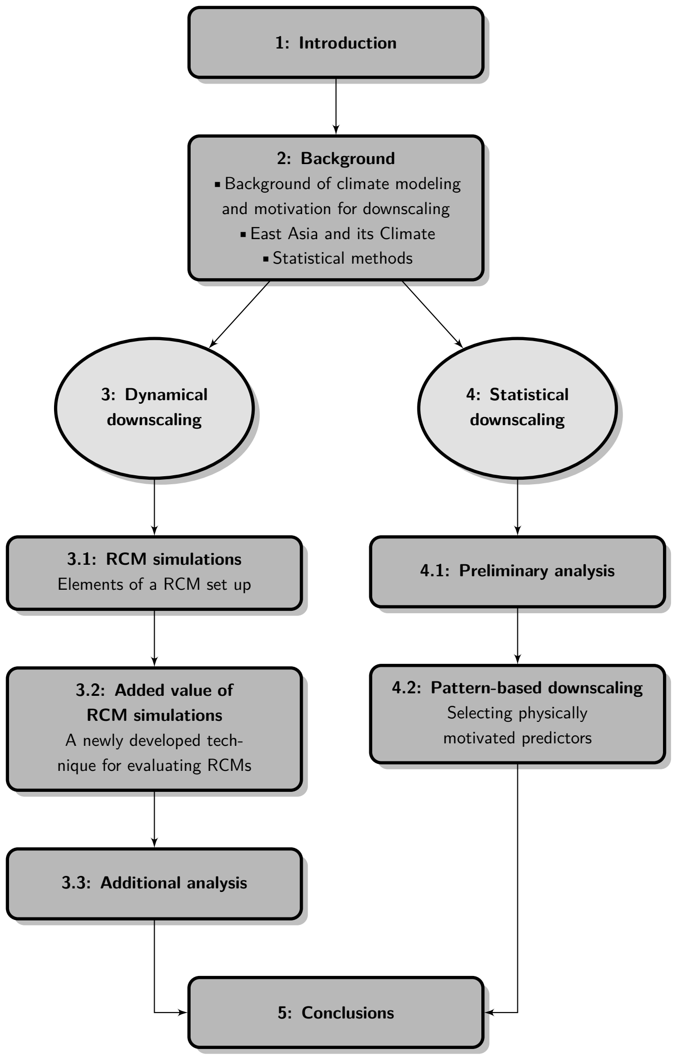

Chapter 2

Background

2.1 Downscaling of Climate Data

Climate Modeling

There is a variety of different assessments to climate modeling. This leads to a hierarchy of models, each of which seeking a trade-off between model simplicity and system complexity depending on its own purpose. On the one end of the spectrum putting emphasis on model simplicity we find low-dimensional models designed to gain a conceptual understanding of climate processes (e.g., Lorenz, 1963; Hasselmann, 1976; Saravanan and McWilliams, 1998). In the middle of the spectrum some models with intermediate complexity can be found (e.g., Fraedrich et al., 1998; Dommenget and Flöter, 2011). On the other end of the spectrum speaking about system complexity is a class of coupled general circulation models (GCM) (a summary of current GCMs can be found in Meehl et al., 2007; Taylor et al., 2012). These models couple the individual components of the climate system, which are at least atmosphere[1] and ocean[2] (hydrosphere), but can also include cryosphere, biosphere and lithosphere. This class of models is based on fundamental physics, i.e., the laws of hydrodynamics and thermodynamics. Originally general circulation models built the base of numerical weather forecasting, but also found their way into climate modeling in the end of the 1950s (Lynch, 2008).

Climate and Weather

In this light we would like to review definitions of weather and climate. By the term *weather* we understand the complete – in space and variable space – state of the atmosphere. For weather forecasting purposes the observed weather state at a certain time is used as initial condition for a GCM simulation. This makes weather forecasting with GCMs, so-called numerical weather prediction (NWP), an initial value problem. By *climate* we mean the probability density distribution (pdf) over all potential states of the atmosphere, which describes the likelihood of a certain weather to occur.

[1] A stand-alone atmospheric general circulation model is also often called AGCM.
[2] A coupled atmosphere and ocean general circulation model is called AOGCM.

Therefore, weather can be seen as a realization of a particular climate. In contrast to weather, climate does not depend on the initial state, but on the boundary conditions, which are mainly the strength of the radiative forcing, and the chemical composition of the atmosphere, and mechanical properties of the Earth like rotations rate, land sea distribution, and land-use properties. In a climate projection context a single GCM simulation also computes weather states, but these states have to be interpreted as a possible realization of the underlying climate. To assess the pdf over all potential weather states, i.e., the associated climate, an ensemble of GCM simulations has to be performed (Tebaldi and Knutti, 2007). The GCM simulations are initialized with different conditions and might use different GCMs (Taylor et al., 2012). An appropriate post-processing of the ensemble leads to an estimate of the climate state (Min and Hense, 2006; Schölzel and Hense, 2011).

Co-operative climate modeling

Generating climate simulations is associated with high efforts on both the developing side and the computational side. This is especially true in the light of ensemble generation. Consequentially, a cooperation of climate scientists involved in climate modeling was formed to bundle different model approaches and to co-organize experiments. The World Climate Research Programme (WCRP) set up the Coupled Model Intercomparison Project (CMIP) for this purpose. Experiments in the current phase 5 (CMIP5)[3] are grouped into long-term on the one side and near-term experiments on the other side (Taylor et al., 2012). Long-term experiments include simulations over a century or longer, e.g. pre-industrial control run, historical runs (1850–2005) and future projections (2006–2100 or longer). For the latter group concentration pathways of greenhouse-gases in the atmosphere serve as boundary conditions for future climates. Near-term experiments concern decadal climate predictions. Both hindcast and prediction runs are performed. Decadal predictions are no longer an isolated boundary value problem, but initialization of the ocean state including sea ice by observations, i.e. data-assimilation, has to be considered in order to gain a benefit over long-term future projections (Taylor et al., 2012).

Climate change

The major motivation for climate modeling is the detection and attribution of climate change. Therefore, a definition should be given at this point. The first two terms, *Internal variability* and *external changes* are based on their physical background. *Internal variability* refers to variability generated by the inherent chaotic behavior of the climate system (Lorenz, 1963), non-linearities (Hoerling et al., 1997), or feedbacks between sub-systems (Saravanan and McWilliams, 1998). *External changes* of the climate system are changes in the boundary conditions, i.e., changes of the solar radiation or the chemical composition of the atmosphere. Besides these two terms there are two other definitions occurring often in the discussions about climate change. These two definitions indicate a cause of climate change. *Natural variability* is the opposite to *anthropogenic climate*

[3]The downscaling studies in Appendix A and B are based on models from CIMP3 (Meehl et al., 2007), which is the phase previous to CIMP5.

change. The first includes internal variability and external changes from natural sources, i.e., changes of the solar radiation due to variability of sunspots, or a change of the composition of the atmosphere by volcanic eruptions. The latter refers to man-made change, i.e. in greenhouse-gas concentration and aerosols, or changes in land-use.

Limitations of GCMs

Technically, a GCM consists of a set of discretized differential equations, which is solved numerically. As this integration is computationally demanding the resolution of a GCM is limited to approximately several hundred km (Meehl et al., 2007; Taylor et al., 2012). Furthermore, the GCM output has to be interpreted as an average over an area associated with the effective resolution of the model, which is for numerical reasons in the order of 4 or grid boxes (Pielke Sr, 2013). In turn this leads to a reduction of variance in comparison to local-scale values, that are experienced in nature. This is often referred to as *change of support* in geostatistics (Wackernagel, 2010), and is the reason for several limitations of GCMs. Local forcing, i.e., complex topography and land-surface characteristics, are weakly represented. Furthermore, there is a lack of accuracy in the description of extreme events. GCMs provide reliable information about climate at the global to continental-scale. In the fields of climate impact assessment and development of adaptation strategies local-scale information are often required. Therefore, it is essential to post-process the GCM output in order to receive a quantification of climate at the regional to local-scale, which is called *downscaling* (Giorgi et al., 2009). The field of downscaling is separated into two categories. On the one hand *dynamical downscaling* involves circulation models that are limited to an area of interest. On the other hand in *statistical downscaling* transfer functions linking large-scale to local-scale information are employed. These two approaches are described in the following sections.

2.1.1 Dynamical Downscaling

By dynamical downscaling the integration of a limited area AGCM is meant, which is often referred to the term regional climate model (RCM). At the lateral boundaries of the limited domain boundary conditions for atmospheric variables have to be provided. These lateral boundary conditions (LBC) are taken from a global AOGCM, in order to obtain a high-resolution version for the climate scenario of the applied global model. This downscaling method is based on physics, that are included in the dynamical core of the RCM. A RCM simulation is therefore determined by three components, i.e., its dynamical core (COSMO-CLM (Rockel et al., 2008), WRF (Shamarock et al., 2008), REMO (Jacob et al., 2012),...), its lateral boundary conditions (provided by a global model, cf. CIMP3 (Meehl et al., 2007) or CIMP5 (Taylor et al., 2012)) and its numerical setting (resolution, domain, update frequency of LBC, sponge zone setting). In the framework of estimating climate an assessment of the associated uncertainties is only realizable by generating an ensemble of RCMs with equal numerical settings, but either different physics, and/or different LBC, and/or different initial conditions. Of course, the output of a single RCM simulation depends also on the initial conditions of the simulation, but these initial conditions are assumed to be chosen randomly. Therefore, the effect of the initial conditions cancels out by the application of an ensemble of RCM simulations, where each member is assumed to represent an equally likely realization of climate (Taylor et al., 2012).

The output of RCMs is physically consistent, which is the main advantage specific to the dynamical downscaling approach. In detail this means that the full multi-variate space of variables and space is simulated, and therefore a comprehensive picture of co-variability within the model physics is captured. A specific shortcoming of the dynamical downscaling approach is that is comes with high computational costs, especially in an ensemble framework.

RCM simulations are often requested from scientist not based in climate sciences, but dealing with the assessment of climate change impact, developing adaptation strategies, or applying the RCM output as forcing for hydrological or biological models. The evaluation of the RCM or its model physics cannot be assigned to the users, but the developing climate sciences are in charge of this task. That is exactly the area to which sections 3.1, 3.2, and the corresponding Appendices A and B are contributing to.

In section 3.1 first results of a set of RCM simulations are presented. The dynamical core COSMO-CLM is adapted to an East Asia domain with a horizontal resolution of 50 km, and forced with LBC from ECAHM5 20C3M, ECHAM5 A1B and ERA-40 re-analysis (Wang et al., 2013). The study does not lead to a sufficient ensemble for climate assessment, but additional contributions of regional modeling in East Asia (Sato and Xue, 2013) would be necessary to build up an ensemble. The RCM simulations were performed on super-computers of the DKRZ. Mean temperature and precipitation patterns were compared to gridded observations and strong biases in the precipitation values were found. Furthermore, the ability of the model to reproduce atmospheric dynamics typical for East Asia in the RCM output was shown. For the two monsoon systems the East Asian Summer Monsoon (EASM) and the East Asian Winter Monsoon (EAWM) associated weather events are illustrated. For the EASM an example for the propagation of a so-called South-West Vortex is shown. Together with these cyclonic disturbances heavy precipitation events are likely to occur along the Meiyu-belt, which is the major rain-belt in the EASM system. For the EAWM the development of a cold surge event was shown. These cold air outbreaks from the stationary Siberian-Mongolian high pressure system extend up to Southern China and cause very cold and dry weather conditions in the region. Despite the strong precipitation biases, the instance that the monsoon dynamics are present in the simulations point out the value of the results and the potential of the simulations for further analyses.

In the above study it was revealed that EASM variability on the seasonal scale in the RCM output is significantly correlated to EASM variability of the driving model. That means the variability was taken over from the driving model through the lateral boundary conditions (LBC). The question whether there is something like a *cut-off frequency* beyond which the RCM generates variability on its own independently from its driving model motivated the research presented in Appendix B (Simon et al., 2013b). A cross-spectral analysis was employed to evaluate the RCM simulation, i.e., COSMO-CLM East Asia (cf. above), against a bi-linearly interpolated version of its driving counterpart ECHAM5 20C3M run no.1 (anthropogenic and natural forcing). The resulting coherence pattern in space are related to the predominant dynamics, i.e., monsoons and inter-tropical convergence zone (ITCZ), in the East Asia region. This study (Appendix B) contributes to the debate about quantifying added value of RCM simulations, which is further discussed in section 3.2. Furthermore, COSMO-CLM simulations with 7 km resolution for the two catchments of interest for the research project were presented in this paper for the first time.

2.1.2 Statistical Downscaling

A transfer of information from larger to smaller scales can also be realized by statistics. Therefore statistical relationships between large-scale predictors and local-scale predictands are developed and applied to climate simulations. The climate simulation can either be global or regional. Even RCM simulations often do not reach sufficient horizontal resolutions for further hydrological and biological applications, or for impact studies and adaptation purposes. During the past three decades a multiplicity of methods have been developed by statisticians, climate sciences and hydrologists. A statistical downscaling always have to contain the following parts: *a*) Observations of the target variables at the target locations. *b*) Climate simulations, in which observed large scale forcing are employed, over the same period as the observations. This period has to extend sufficiently in time to provide an adequate database divisible into training and verification period. *c*) Climate simulations over a projection period. These simulations has to be based on the same GCM as the simulations above to prevent errors due to biases between different GCM approaches. *d*) An appropriate statistical method for developing the transfer function between large-scale predictors and local-scale predictands.

On the one hand a specific drawback of statistical downscaling schemes is the requirement for a strong observational database over at the target locations. This is often not the case in *real world* problems, i.e., a remote region located in an arid climate zone. On the other hand given appropriate data statistical downscaling leads to estimates of climate on the local-scale. Another specific advantage of this downscaling category, is that it is easy to implement and computationally feasible.

There is an abundance of statistical methods for downscaling purposes. Therefore a crucial contribution of researchers with a background in atmospheric science is the development and interpretation of predictors for variables that are poorly simulated by dynamical models. In this light a study employing statistical downscaling is summarized in section 4.2. Daily precipitation observations, taken from rain gauges located in the Poyang catchment in China, are transformed to dichotomous variable indicating the exceedance over a certain threshold. The predictors are extracted from re-analysis data, i.e., ERA-40, via different kinds of EOF analyses. A forward selection scheme identifies the predictor suiting the target variable best in a logistic regression framework. Although the EOF analysis provides an objective technique for a weather type classification, the preferred predictor pattern could be associated with a weather phenomenon typical for the summer monsoon season, i.e., South-West vortices. The focus of the study is set on delivering physically interpretable predictors for local precipitation values (Simon et al., 2013a).

2.2 East Asia and its Climate

There are two monsoon systems influencing the climate in East Asia. During summer time the East Asian summer monsoon takes place. Its dynamics are described in the following section. Afterwards, the most prominent feature of the East Asian winter monsoon is outlined.

2.2.1 East Asian Summer Monsoon

As the project is related to water management and extremes, the main focus was set on the East Asian Summer Monsoon (EASM), that can be associated with strong and high impact rain events in the regions of interest. The EASM is a mainly independent of the Indian summer monsoon (ISM), though there are some interaction taking place between the two monsoon systems. In this section important features of the EASM system are reviewed.

The phases of the EASM

The onset of the EASM is associated with the development of a cyclone over the Bay of Bengal in early May. Along with the formation of this pressure system an acceleration of the low level westerlies is initialized. In turn convective activity in both the spatial extend and its intensity increases. Afterwards the seasonal march of the EASM can be separated into three quasi-stationary periods and two abrupt northwards jumps in between these quasi-stationary periods. During the first quasi-stationary period – in May – the center of the Monsoon system lies above the Indochina peninsula and the Southern Chinese Sea (SCS). During the second phase – between mid June and mid July – a rain belt is established over the Yangtze valley and extends further eastward to the South of Japan. Afterwards the rain belt performs another jump to bring Monsoon weather to the North of China and Korea in August Ding and Chan (2005).

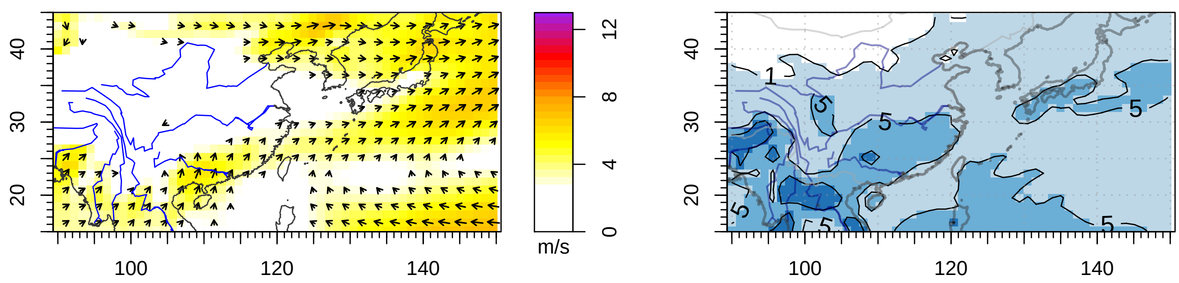

Figure 2.1: ERA 40 850 hPa wind field (left – arrows indicate direction, and colors indicate amplitude) and 24h accumulated precipitation (right – values in mm) averaged from 12th May to 17th May for the years from 1960 to 1999.

These phases are illustrated by the low level (850 hPa) wind fields and precipitation pattern in ERA-40 (Uppala et al., 2005). Figure 2.1 shows the synoptic situation during the first quasi-stationary period occurring generally in early May and persist throughout the month. In the wind field pattern two subsystems can be distinguish . Between 90°–115°E southwesterlies support the moisture transport from the Bay of Bengal and the Southern Chinese Sea further to the North. East of 125°E appears the western bound of the subtropical high located over the western Pacific. The anticyclonic system supports the transport of moist tropical air to the North. This is the time of the pre-summer rain season over the Yangtze River basin (Wang, 2006). Consistent pattern are revealed by the spatial distribution of mean precipitation. Strong monsoon-like rainfalls occur over the Indochina peninsula and in Bangladesh. The rain system extends further to the southeast of China, where the pre-summer rain season takes place.

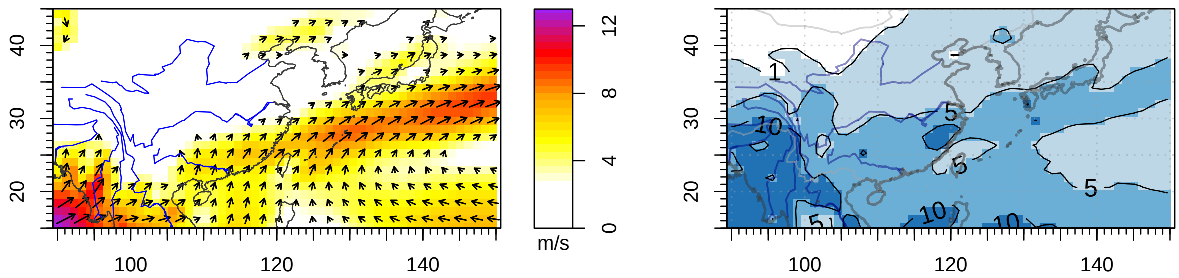

Figure 2.2: ERA 40 850 hPa wind field (left – arrows indicate direction, and colors indicate amplitude) and 24h accumulated precipitation (right – values in mm) averaged from 17th June to 22th June for the years from 1960 to 1999.

After this period the monsoon system performs an abrupt northward shift. This shift goes along with a rapid northward movement of the ITCZ and the subtropical high over the western North Pacific (Wang, 2006). Due to this shift the so-called Meiyu rain-belt is established over the Yangtze valley (figure 2.2). This rain-belt extends to the North east and also covers parts of Korea and Japan, where this synoptical feature is called Changma and Baiu, respectively. This phase persists from mid June until mid July. The precipitation associated with the Meiyu follows a different distribution than the precipitation during the pre-summer rain season. The rain events occur less frequent, but they are of stronger intensity. These event are usually associated with meso-α scale disturbances, i.e. South-West vortices, of the frontal system. A closer description of these disturbances is given in chapter 4, which highlights the potential of EOF pattern to be applied as predictors for precipitation properties at the local-scale in the Yangtze valley.

The third phase of the EASM takes place between mid July and mid August. The circulation and the rainfall pattern have changed in a rapid manner (figure 2.3). The sub-tropical high in the Western Pacific has moved to the North and the dominant Meiyu belt has dissolved. A rainfall maximum is now located over North China. The strength of this phase is an important factor for the water management in this region, as it determines the amount of water that reaches the northern part of China, which is very dry throughout the rest of the year. A strong EASM is associated with the extension of this wind and precipitation system to Northern China. Thus a strong EASM

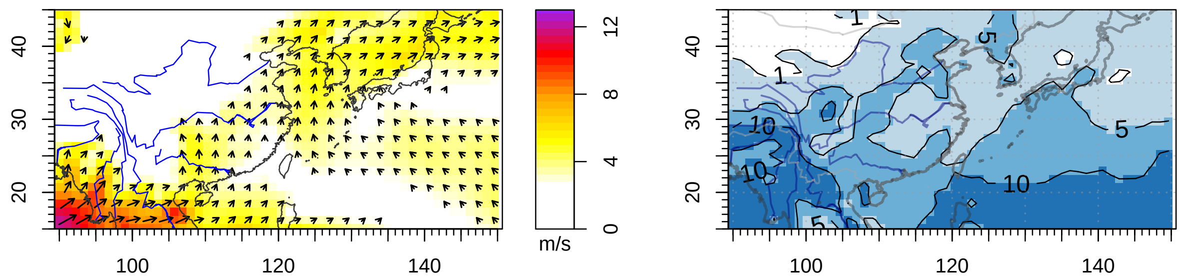

Figure 2.3: ERA 40 850 hPa wind field (left – arrows indicate direction, and colors indicate amplitude) and 24h accumulated precipitation (right – values in mm) averaged from 29th July to 3rd August for the years from 1960 to 1999.

transports the moisture to the very North of China causing a summer with a large amount of rain. In contrast a weak EASM does not develop the wind systems in the same way, but the precipitation zone remains longer above the Yangtze valley. This leads to years with stronger than normal rainfalls in this region.

Teleconnections

The El Niño Southern Oscillation is the dominant climate variability of the coupled atmosphere-ocean system in the Pacific region. The quasi-periodic warming of the central and eastern Pacific Ocean affects the atmosphere of the western part of the Pacific by its influence on the Walker circulation (Bjerknes, 1969). There is empirical evidence for a link between strong EASM events and preceding El-Niño winters. In contrast, a relation between preceding La-Niña events and weaker than normal EASM seasons is not supported by the data[4]. Hence, the topic is well discussed by scientists focusing on the EASM (Wang et al., 2000; Chang et al., 2000; Wang, 2002).

An analysis of the six major El Niño events in the second half of the 20th century suggests a possible physical explanation for the teleconnection between ENSO and EASM (Wang et al., 2000). A positive anomaly of the western North Pacific high pressure system (WNPH) is associated with the warming over the central and eastern Pacific during winter. This link is established by the so-called Pacific-East Asian teleconnection, which is a wave pattern visible in both the vorticity anomalies and SST anomalies over the western and central Pacific. At first, this teleconnection leads to a weakening of the East Asian winter monsoon (cf. below), but it also enhances the likelihood of a stronger than normal EASM when the anti-cyclonic anomaly of the WNPH persists until the following summer, i.e. EASM season (Wang et al., 2000).

[4]Tested with data from 1958 to 2002. The Niño 3.4 index averaged over boreal winter (December to February) was compared to the seasonal (June to August) EASM index suggested by Wang and Fan (1999) computed from the ERA-40 dataset. El Niño and La Niña events were identified for the Niño 3.4 index exceeding 0.5 and falling below -0.5, respectively. A t-test statistic was applied supporting the relationship between preceding El-Niño winters and strong EASM seasons at a significance level of 1%.

ENSO is not the only phenomenon influencing the EASM, but snow depth and heating processes of the Tibetan Plateau are also a key factor (Barnett et al., 1989; Qian et al., 2003; Wu and Qian, 2003). An analysis of observational data of both snow measurements over the Tibetan Plateau and rain gauges spread over East China reveals the relations between these two regions. If the snow depth over the eastern Tibetan Plateau is deeper than normal, the spatial precipitation anomaly pattern over East China is typical for a weak EASM season. The summer precipitation in the Yellow River basin and in the northern part of China is less than normal. In contrast, the precipitation anomaly along the Yangtze River basin is positive (Qian et al., 2003). With respect to Barnett et al. (1989) it is suggested than the positive snow depth anomaly over the Tibetan Plateau is memorized in the land-atmosphere system by an enhanced amount of soil-moisture that is available throughout the year. The importance of the Tibetan Plateau for heavy precipitation events over the Yangtze valley is further discussed in chapter 4, where the generation of meso-α-scale disturbances over the Plateau and their progression along the Yangtze valley is described. The occurrence of these disturbances rises the probability for local heavy rainfall events (Simon et al., 2013a).

Climate Change associated with the EASM

Observations for the second half of the 20th century show a clear change pattern of annual mean precipitation, which is often referred to *Flooding of the South and drying of the North*. While, e.g., Southern China, where the Yangtze catchment is located, experienced an increase in annual mean precipitation of about 5% per decade, the Northeast of China experienced a decrease in mean annual precipitation of about 5% (Zhai et al., 2005). This change pattern is strongest for the summer season, i.e. the EASM season, with estimated increases of 10%–15% over the Yangtze valley (Wang and Zhou, 2005).

There is a well approved reasoning to this phenomenon: In both regions precipitation during the summer monsoon season contributes the major part of the annual precipitation amount (Zhai et al., 2005). The dynamics of the EASM weakened abruptly in late 1970s (Wang and Zhou, 2005; Li et al., 2010). Subsequently the EASM did not extent to the very north of China in late summer as before, but lingers over the Yangtze valley instead. This leads to the pattern described above: The stabilized EASM over the Yangtze valley brings more precipitation to the South while the North gets less rain compared to the period before.

The reason for the shift in EASM dynamics remains an open question. There are indications that this shift is part of the internal variability of the general circulation. The EASM is characterized by strong inter annual to decadal variability that might supersede the long-term climate change in the second half of the 20th century (Li et al., 2010).

2.2.2 East Asian Winter Monsoon

As the East Asian winter monsoon (EAWM), which occurs normally between November and March (Wang, 2006), only plays a minor role in the following chapters, only a brief overview should be given here. In general, the EAWM reverses the circulation of the EASM, as prevailing surface winds north of the equator are now blowing from the Northeast. These northeasterlies are supported by the trade wind in the tropics. Over the mid-latitudes these northeasterlies are associated with the anticyclonic circulation of the quasi-stationary Siberian-Mongolian high (SMH), which is a pronounced cold-core high pressure system. The most prominent weather phenomenon, which is related to the EAWM, is an intense outbreak of cold air from the center of the SMH (Zhang et al., 1997). These cold air outbreaks, called *cold surge* in literature, extend to the South reaching the tropics within several days. In chapter 2 an example of a *cold surge* event, as it was modeled by the RCM COSMO-CLM with 50 km resolution, is presented. The example illustrates the ability of the RCM to reproduce the EAWM dynamics (Wang et al., 2013).

2.3 Statistical Methods

This chapter outlines statistical methods, which are applied in the following chapters. The statistics are assigned to three different categories: Parametric Modeling, Model Verification, and Analytic tools.

2.3.1 Parametric Modeling

Parametric modeling is based on an assumption of the distribution of the data, that has to be investigated. Following this assumption a parametric distribution can be selected, and the parameters can be fitted by numerical optimization. Here, a description of *a*) linear regression, which assumes a normal distribution of the residuals, *b*) generalized linear models, of which logistic regression is presented as a special case, and *c*) the generalized extreme value distribution (GEV), for modeling block maxima is given. For each item a test statistic is presented, allowing decisions whether to reject a reference model, or null model, in favor of an alternative model.

Linear Regression

The purpose of *linear regression* is to find a linear relationship between the *predictand variable* $\mathbf{y} = (y_1, y_2, \ldots, y_m)^T$, or *dependent variable*, and one or more *predictor variables* $\mathbf{x}_{*,1} = (x_{1,1}, x_{2,1}, \ldots, x_{m,1})^T$, or *independent variables*:

$$\mathbf{y} = \mathbf{X}\boldsymbol{\beta} + \boldsymbol{\epsilon}, \quad \text{with} \quad \mathbf{X} = \begin{pmatrix} x_{1,0} & x_{1,1} & \cdots & x_{1,n} \\ x_{2,0} & x_{2,1} & \cdots & x_{2,n} \\ \vdots & \vdots & \ddots & \vdots \\ x_{m,0} & x_{m,1} & \cdots & x_{m,n} \end{pmatrix}. \tag{2.1}$$

$\mathbf{X}$ is called *design matrix*, which bundles all n predictors, and each predictor fills one column. $\boldsymbol{\beta} = (\beta_0, \beta_1, \ldots, \beta_n)^T$ is the parameter vector. For most problems it is convenient to choose $\mathbf{x}_{*,0} = (1, 1, \ldots, 1)^T$. In turn the zero parameter β_0 works as an intercept. $\boldsymbol{\epsilon} = (\epsilon_1, \epsilon_2, \ldots, \epsilon_m)^T$ contains the residual information, which are not covered by the linear model $\hat{\mathbf{y}} = \mathbf{X}\boldsymbol{\beta}$. The single residuals have to be independent and normally distributed with zero mean and constant variance σ^2, $\epsilon_i \sim \mathcal{N}(0, \sigma^2)$, in order to allow correct inference from the model. The residuals $\boldsymbol{\epsilon}$ correspond only to uncertainties associated with the deficit of the model to represent the predictand $\mathbf{y}$. Thus, linear regression is applicable when the predictors $\mathbf{x}_{*,1}$ can be assumed to be free of errors, e.g. a time of a measurement.

Estimating the parameter $\boldsymbol{\beta}$ is straightforward via *least-squares* fit,

$$\boldsymbol{\beta} = \arg\min \sum_{i=1}^{m} (y_i - \hat{y}_i)^2 = \arg\min \sum_{i=1}^{m} \epsilon_i^2, \tag{2.2}$$

which minimizes the variance σ^2. This estimator is equivalent to the maximum likelihood estimator (MLE).

Suppose that there are two models on hand $\mathcal{M}_0$ and $\mathcal{M}_1$ for representing a time series $\mathbf{y} = (y_1, y_2, \ldots, y_m)^T$ generated from a random variable Y. $\mathcal{M}_1$ is characterized by the parameters $\boldsymbol{\beta}^1$, and $\mathcal{M}_0$ is characterized by a subset of these parameters $\boldsymbol{\beta}^0 \subset \boldsymbol{\beta}^1$. A decision has to be made, whether it is worth rejecting $\mathcal{M}_0$ in favor of $\mathcal{M}_1$. Given the assumption of normally distributed residuals, which can be described by their variance σ^2 only, it is reasonable to base the decision for rejecting $\mathcal{M}_0$ in favor of $\mathcal{M}_1$ on the ability of $\mathcal{M}_1$ to reduce the variance of the residuals $\sigma_1^2 < \sigma_0^2$. For a simple linear regression, i.e. $\boldsymbol{\beta}^1 = (\beta_0^1, \beta_1^1)^T$ and $\boldsymbol{\beta}^0 = (\beta_0^0)$, this decision can be assessed by the F-ratio.

The F-ratio is the ratio of the *mean squared regression*

$$MSR = \sum_{i=1}^{m} (\hat{y}_i - \bar{y})^2, \tag{2.3}$$

where $\bar{y}$ is the mean of the predictand, and the *mean squared error*

$$MSE = \frac{1}{m-2} \sum_{i=1}^{m} (y_i - \hat{y}_i)^2, \tag{2.4}$$

$F = MSR/MSE$. F follows a Fisher-distribution with one, and $m-2$ degrees of freedom. Thus, if F is located in the upper p% of the corresponding Fisher-distribution, $\mathcal{M}_0$ can be rejected in favor of $\mathcal{M}_1$ at the *significance* level p. Significance is the probability of wrongly rejecting a true null model in favor of an alternative model.

Generalized Linear Model

Linear regression can be grouped into *generalized linear models* (GLM). After all, assumptions about the distribution have to be made. Generalized means that there is a common likelihood for representing different distributions in the exponential family,

$$f(y_i|\theta, \phi) = \exp\left(\frac{y_i\theta - b(\theta)}{a(\phi)} + c(y_i, \theta)\right). \tag{2.5}$$

y_i is one element of the vector $\mathbf{y} = (y_1, y_2, \ldots, y_m)^T$, which is assumed to be a realization of a random variable Y. $a(\phi)$, $b(\theta)$ and $c(y_i, \theta)$ are specific functions corresponding to the specific distribution in the exponential family, and θ and ϕ are parameters associated with the distribution. Expectation and variance of Y in this generalized framework are

$$E(Y) = \boldsymbol{\mu} = \frac{\partial b(\theta)}{\partial \theta}, \quad \text{and} \quad VAR(Y) = a(\phi)\frac{\partial^2 b(\theta)}{\partial \theta^2}, \tag{2.6}$$

respectively. The predictors, or co-variates, build the linear predictor

$$\eta = \mathbf{X}\boldsymbol{\beta}, \tag{2.7}$$

which is linked to the expectation by the *link function* g. Every distribution in the exponential family has a *canonical*, or natural, link function. Its inverse is called the *response function* $h = g^{-1}$:

$$\eta_i = g(\mu_i) = \mathbf{X_i}\boldsymbol{\beta}, \quad \text{and} \quad \mu_i = h(\eta_i) = h(\mathbf{X_i}\boldsymbol{\beta}). \tag{2.8}$$

For instance, the normal distribution $Y \sim \mathcal{N}(\mu, \sigma^2)$ can expressed in a generalized version by substituting,

$$a(\phi) = \phi, \quad b(\theta) = \frac{\theta^2}{2}, \quad \text{and} \quad c(y_i, \phi) = -\frac{1}{2}\left(\frac{y_i^2}{\phi} + \log(2\pi\phi)\right), \tag{2.9}$$

with $\theta = \mu$ and $\phi = \sigma^2$ into equation (2.5). In this case the canonical link function is the identity function, thus $\mu = \mathbf{X}\boldsymbol{\beta}$, and the variance σ^2 is constant. This leads to the linear regression described above.

When the predictand variable follows a Bernoulli distribution $Y \sim \mathrm{Be} = p^y(1-p)^{1-y}$, and $Y \in \{y = 0, y = 1\}$, substituting the specific functions

$$a(\phi) = 1, \quad b(\theta) = \log(1 + \exp\theta), \quad \text{and} \quad c(y_i, \phi) = 0, \tag{2.10}$$

with $\theta = \log(p/1-p)$ into equation (2.5) yields

$$f_{Bernoulli}(y_i|p) = \exp\left(y_i \log\left(\frac{p}{1-p}\right) + \log(1-p)\right). \tag{2.11}$$

In this case the expectation $E(Y) = p$, and the *logit function* is the canonical link function:

$$g(p) = \log\left(\frac{p}{1-p}\right), \quad \text{and} \quad g^{-1}(\eta) = h(\eta) = \frac{1}{1+e^{-\eta}}. \tag{2.12}$$

Estimating the parameters of the linear predictor (equation 2.7) is solved by maximizing the log-likelihood

$$l(\mathbf{y}|\boldsymbol{\theta}) = \sum_{i=1}^{m} \frac{y_i\theta_i - b(\theta_i)}{a(\theta)} + c(y_i, \theta_i). \tag{2.13}$$

It is possible assessing whether it is worth rejecting a reference model, or null model, $\mathcal{M}_0$ in favor of an alternative model by *likelihood-ratio* test. For the likelihood-ratio test a test statistic summarizing the difference of the log-likelihoods corresponding to $\mathcal{M}_0$ and $\mathcal{M}_1$, and thus the logarithm of the ratio of the likelihoods,

$$D = 2\left(l(\mathcal{M}_0) - l(\mathcal{M}_1)\right), \tag{2.14}$$

is introduced, which is denoted as D as it is often call *deviance*. $l(\mathcal{M}_0)$ and $l(\mathcal{M}_1)$ refer to the log-likelihood of the null model and alternative model, respectively. Assume that $\mathcal{M}_1$ contains n parameters, and $\mathcal{M}_0$ contains $n-k$ parameters. It it worthwhile rejecting $\mathcal{M}_0$ in favor of $\mathcal{M}_1$ at significance level p, if $D < q_p$, where q_p is the $1-p$ quantile of the χ^2_k distribution (McCullagh and Nelder, 1989).

Extreme Value Theory

Not all distributions can be included in the framework of generalized linear models. For instance, the *generalized extreme value distribution* (GEV), which is based on extreme value theory (EVT) (Fisher and Tippett, 1928). Assume $\mathbf{y} = (y_1, y_2, \ldots, y_m)$ is a sequence of independent realizations of the random variable Y with the marginal distribution F. The sequence $\mathbf{y}$ is now split into blocks of the length n, and $M_n = \max(y_1, y_2, \ldots, y_n)$ represents a process of the maxima of the single blocks. If one element of the sequence undershoots the threshold z with the probability $p = F(z)$. Under the assumption of independent realizations the probability that all n elements are less than z is p^n, which is equal to the probability that the maximum $M_n < z$,

$$P(M_n \leq z) = (F(z))^n . \tag{2.15}$$

In practice the marginal distribution F is often unknown, or a parametric approach for the whole distribution lacks precision at the tails. Motivation of EVT is to give a distribution describing $(F(z))^n$, without further assumptions about F. For the block-maxima approach EVT according to Fisher and Tippett (1928) leads to

$$G(z) = \begin{cases} \exp\left\{-\left[1+\xi\left(\frac{z-\mu}{\sigma}\right)\right]^{-1/\xi}\right\} & \xi \neq 0 \\ \exp\left[-\exp\left\{-\left(\frac{z-\mu}{\sigma}\right)\right\}\right] & \xi = 0, \end{cases} \tag{2.16}$$

which is the cumulative distribution function (cdf) of the so-called the generalized extreme value distribution (GEV), and is described by three parameters: the location parameter μ, the scale parameter σ, and the shape parameter ξ (Coles, 2001). $\mathbf{z} = (z_1, z_2, \ldots, z_l)$ is a sequence of realizations of the random variable Z describing the block maxima. The corresponding probability density function (pdf), is

$$f_{GEV}(z_i|\mu,\sigma,\xi) = \begin{cases} \frac{1}{\sigma}\left[1+\xi\left(\frac{z_i-\mu}{\sigma}\right)\right]^{-(1+1/\xi)} \exp\left\{-\left[1+\xi\left(\frac{z_i-\mu}{\sigma}\right)\right]^{-1/\xi}\right\} & \xi \neq 0 \\ \frac{1}{\sigma}\exp\left\{-\left(\frac{z_i-\mu}{\sigma}\right)\right\}\exp\left[-\exp\left\{-\left(\frac{z_i-\mu}{\sigma}\right)\right\}\right] & \xi = 0. \end{cases} \tag{2.17}$$

The shape parameter ξ plays a special role, as it defines the character of the distribution. For $\xi < 0$, $\xi = 0$, and $\xi > 0$ correspond to the Weibull, Gumbel, and Fréchet families, respectively. The Weibull has an upper bound, the Gumbel has an exponentially decreasing tail, and the Fréchet's tail decays as a power function. The roles of the three parameters is illustrated in figure (2.4a–c).

In practice when the chosen blocks correspond to a certain time period, e.g. one year, one season or one day, it is convenient to express the distribution in terms of extreme quantiles obtained by setting the cdf (equation 2.16) equal to $1-p$ and inverting the equation,

$$z_p = \begin{cases} \mu - \frac{\sigma}{\xi}\left[1-\{-\log(1-p)\}^{-\xi}\right] & \xi \neq 0 \\ \mu - \sigma\log\{-\log(1-p)\} & \xi = 0. \end{cases} \tag{2.18}$$

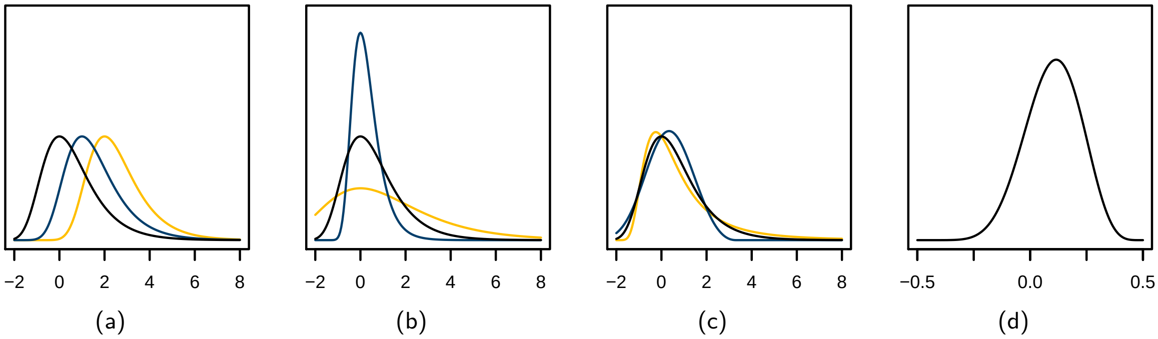

Figure 2.4: (a)–(c) The roles of GEV's parameter, all plots show probability density functions (pdf) with the parameters $\theta = (\mu, \sigma, \xi)$. (a) Changes in the location parameter μ. Black: $\theta = (0, 1, 0)$, Blue: $\theta = (1, 1, 0)$, and Yellow: $\theta = (2, 1, 0)$. (b) Changes in the scale parameter σ. Black: $\theta = (0, 1, 0)$, Blue: $\theta = (0, .5, 0)$, and Yellow: $\theta = (0, 2, 0)$. (c) Changes in the shape parameter ξ. Black: $\theta = (0, 1, 0)$, Blue: $\theta = (0, 1, -.3)$, and Yellow: $\theta = (0, 1, .3)$. (d) $\mathrm{Beta}(6, 9)$ as a prior density for the shape parameter ξ, the maximum is at $\xi = 0.1$.

z_p is called the *return level* corresponding to the *return period* p^{-1}. z_p is exceeded by the maximum of each block with probability p (Coles, 2001).

Estimation of the parameters can be solved by maximum likelihood estimation (MLE), with the likelihood

$$L(\mathbf{z}|\mu, \sigma, \xi) = \prod_{i=1}^{l} f_{GEV}(z_i|\mu, \sigma, \xi). \tag{2.19}$$

However, MLE can lead to poor estimates of the parameters, in particular of the shape parameter ξ, when the sample size is small. In order to provide better estimates for ξ with respect to geophysical and environmental applications, Martins and Stedinger (2000) suggested a beta distribution as a prior density,

$$\pi(\xi) = \mathrm{Beta}(\alpha, \beta) = \frac{(0.5 - \xi)^{\alpha-1}(0.5 + \xi)^{\beta-1}}{\mathrm{B}(\alpha, \beta)}, \quad \text{with} \quad \alpha = 6, \beta = 9, \tag{2.20}$$

for the shape parameter ξ (figure 2.4d). α and β are the parameters of the beta distribution, and $\mathrm{B}(\alpha, \beta) = \Gamma(a)\Gamma(b)/\Gamma(a, b)$ is the Beta function, and Γ is the Gamma function. Multiplying the GEV's pdf $f_{GEV}(z_i|\mu, \sigma, \xi)$, which is a conditional probability here, with the prior density $\pi(\xi)$ yields the generalized likelihood function,

$$GL(\mathbf{z}|\mu, \sigma, \xi) = \prod_{i=1}^{l} f_{GEV}(z_i|\mu, \sigma, \xi)\pi(\xi), \tag{2.21}$$

which can be employed as an estimator for the parameters of the GEV. With the parameter of the beta distribution set to $\alpha = 6$ and $\beta = 9$ the maximum of the prior is located at $\xi = 0.1$. Thus, the generalized likelihood (equation 2.21) slightly favors a Fréchet type of the distribution.

The likelihood-ratio test, which was introduced for GLM, is also valid for significance tests of linear models of the GEV parameters, i.e.

$$\mathcal{M}_0 : \mu = \mu^0,\ \sigma = \sigma^0,\ \xi = \xi^0, \quad \text{vs.} \quad \mathcal{M}_1 : \mu = \beta_0 + \beta_1 x,\ \sigma = \sigma^1,\ \xi = \xi^1, \tag{2.22}$$

where the null model $\mathcal{M}_0$ assumes all three parameters to be constant, and the alternative model $\mathcal{M}_1$ includes a linear component for the location parameter.

In order to assess uncertainties associated with the estimated return levels the *profile log-likelihood* technique can be employed. Solving the return level equation (2.18) for μ, and substituting μ into the log-likelihood (log of equation 2.19) or generalized log-likelihood (log of equation 2.21) yields re-parameterized versions of the log-likelihoods, now depending on (z_p, σ, ξ). This re-parameterized log-likelihood can be optimized with respect to (σ, ξ) for a range of values for a certain return level, e.g. 10-year return level, which results in a profile of the log-likelihood at z_p. Now we can adjust the deviance formula (equation 2.14),

$$D = 2\left(l(z_p, \sigma, \xi) - l(z_p = const., \sigma, \xi)\right) \sim \chi_1^2, \tag{2.23}$$

where $l(z_p, \sigma, \xi)$ is the likelihood optimized with respect to (z_p, σ, ξ), and $l(z_p = const., \sigma, \xi)$ is the likelihood with z_p hold fixed and optimized with respect to (σ, ξ). Thus, $conf_\alpha = \{z_p : D \leq q_\alpha\}$, where q_α is the $(1-\alpha)$ quantile of the χ_1^2 distribution, yields to the $(1-\alpha) \times 100\%$ confidence interval (Coles, 2001).

2.3.2 Model Verification

This section deals with model verification. First, scoring rules, which are functions for assessing a model's quality, are described. Afterwards, the principles of cross-validation, which is a method to split the complete dataset into a subset for model training and a subset for model verification, are outlined.

Scoring Rules

Assessing the quality of a forecast is the main purpose of *scoring rules*. Thus, scoring rules are functions depending on the prediction and on the corresponding observation. In the following we denote an unspecified scoring rule as $S(\mathbf{p}, \mathbf{y})$, where $\mathbf{p} = \{p_1, p_2, \ldots, p_n\}$ and $\mathbf{y} = \{y_1, y_2, \ldots, y_n\}$ denote the forecasts and the observations, respectively. With respect to the applications of scoring rules in further chapters, a restriction of the sample space Ω of $\mathbf{p}$ and $\mathbf{y}$ is made. As scoring rules are mainly applied to assess the quality of probabilistic forecasts of dichotomous events (cf. Simon et al., 2013a), we define the sample space $\Omega = [0,1]^n$, and $\mathbf{p}, \mathbf{y} \in \Omega$. However, the single observations y_i can only take the values 0 and 1, and thus $\mathbf{y}$ describes $\{0,1\}^n \subset \Omega$ which is a subspace of Ω.

Following the definition given by Gneiting and Raftery (2007) a scoring rule S is attributed *proper*, if

$$S(\mathbf{y}, \mathbf{y}) \leq S(\mathbf{p}, \mathbf{y}), \qquad \forall\ \mathbf{p}, \mathbf{y} \in \Omega. \tag{2.24}$$

Furthermore, a scoring rule S is attributed *strictly proper*, if $S(\mathbf{y}, \mathbf{y}) = S(\mathbf{p}, \mathbf{y})$ holds if and only if $\mathbf{p} = \mathbf{y}$. In practice often averaged scores,

$$\mathcal{S} = \frac{1}{n} \sum_{k=1}^{n} S(p_k, y_k), \tag{2.25}$$

are calculated to assess the quality of a forecast. Scores calculated for different forecasts schemes are comparable is they are based on the same forecast period, and thus on the same forecasts. The concept of scores can be extended to *skill scores*,

$$\mathcal{SS} = \frac{\mathcal{S}_{fcst} - \mathcal{S}_{ref}}{\mathcal{S}_{perf} - \mathcal{S}_{ref}}. \tag{2.26}$$

Here $\mathcal{S}_{fcst}$ refers to the forecaster's score, which has to be evaluated. $\mathcal{S}_{perf}$ is the score of a perfect forecast, within the framework of a probabilistic forecast for dichotomous events the perfect forecast would predict 100% in advance of an event, and 0% when no event takes place. $\mathcal{S}_{ref}$ is the score of a reference forecast, which can be a mean value of the binary variable over a reference period, e.g. *climatological* forecast. Another often employed reference forecast is the *persistence* forecast, e.g. it assumes that today's observation will be repeated tomorrow. By design the skill score reaches its maximum 1, if $\mathcal{S}_{fcst} = \mathcal{S}_{perf}$, which is valid only for $\mathbf{p} = \mathbf{y}$ in the framework of strictly proper scoring rules. If $\mathcal{S}_{fcst} = \mathcal{S}_{ref}$, the numerator of equation (2.26) diminishes, and if $\mathcal{S}_{fcst} < \mathcal{S}_{ref}$ it gets negative, i.e. $\mathcal{SS} \leq 0$ means no benefit of using the analyzed forecast instead of the reference forecast.

The Brier Score... Probably the most famous and most often applied scoring rule for probabilistic forecasts of dichotomous events is the averaged *Brier score*,

$$BS(\mathbf{p}, \mathbf{y}) = \frac{1}{n} \sum_{k=1}^{n} (p_k - y_k)^2, \tag{2.27}$$

which was introduced by Brier (1950), and is strictly proper. Single probabilistic predictions contribute to the averaged Brier score via the score functions,

$$BS(p_k, y_k = 1) = (p_k - 1)^2 \quad \text{and} \quad BS(p_k, y_k = 0) = p_k^2, \tag{2.28}$$

depending on whether the event occurred $y_k = 1$, or not $y_k = 0$. In a perfect forecast system $\mathbf{p}$ equals $\mathbf{y}$, and thus in every single case the corresponding scoring rule diminishes, leading to an averaged Brier score $BS(\mathbf{p}_{perf}, \mathbf{y}) = 0$, which is the minimum of the Brier Score. This means the Brier score is negative orientated, where smaller values of the score correspond to better forecasts. Substituting equation 2.27 into equation 2.26, and without further specifications of the reference forecast the Brier skill score reduces to

$$BSS = 1 - \frac{BS(\mathbf{p}_{fcst}, \mathbf{y})}{BS(\mathbf{p}_{ref}, \mathbf{y})}. \tag{2.29}$$

...and its decomposition In order to assess different attributes of a forecast's quality, scores can be decomposed. For the Brier score the *calibration-refinement factorization* (CRF) is most common (Murphy and Winkler, 1992). The CRF is based on factoring the joint distribution $P(p, y)$ of forecasts and observations,

$$P(p, y) = P(y|p)P(p), \tag{2.30}$$

where $P(y|p)$ denotes the conditional probability of observations given the forecast, and $P(p)$ denotes the marginal probability of the forecasts. Next to the CRF is it also possible to decompose the joint distribution conditioned on the observation $P(p, y) = P(p|y)P(y)$, which refers to as likelihood-baserate factorization, and will not be further discussed here.

In order to decompose the BS via CRF, the sample space of a single forecast has to be discretized, e.g. $p_i \in \{0.05, 0.15, \ldots, 0.95\}$, and the number of discrete values will be denoted as I, e.g. $I = 10$. Furthermore, the relative frequency of a discrete forecast value is $P(p_i) = N_i/n$, where N_i is the number of forecasts assigned to a discrete forecast values p_i. The sample space of a single observation $y_j \in \{0, 1\}$ is discrete by nature with two levels $J = 2$. Now, the BS can be rewritten as:

$$BS = \sum_{i=1}^{I}\sum_{j=1}^{J} P(p_i, y_j)(p_i - y_j)^2. \tag{2.31}$$

Here, the values of $(p_i - y_j)^2$ are pre-defined by the discretization, and thus all information is now comprised in the joint probability $P(p_i, y_j)$. Note, that due to the discretization the equality $p_i = 1/N_i \sum_{k|p_i} p_k$ is not necessarily fulfilled. Algebra yields

$$BS = \frac{1}{n}\sum_{i=1}^{I} N_i(p_i - \bar{y}_{p_i})^2 - \frac{1}{n}\sum_{i=1}^{I} N_i(\bar{y}_{p_i} - \bar{y})^2 + \bar{y}(1 - \bar{y}), \tag{2.32}$$

with the conditional mean $\bar{y}_{p_i} = \sum_{j=1}^{J} P(y_j|p_i)y_j$ and the unconditioned mean of the observations $\bar{y} = \sum_{k=1}^{n} y_k = \sum_{i=1}^{I} P(p_i)y_{p_i}$. The first term of equation (2.32) is called *reliability*, or *conditional bias*, it summarizes the forecast performance conditioned on a forecast. Smaller values of the reliability are associated with better forecasts. The second term is often reffered to as *resolution*, it gives a measure of the quadratic deviation between the conditional observation $\bar{y}_{p_i}$ and unconditional observation $\bar{y}$. Higher resolution values are associated with better forecasts. The third term, the *uncertainty*, summarizes the marginal distribution of the observations, and is independent of the forecast (Murphy, 1996).

To visualize the CRF the *reliability diagram* can be used. The x-axis of the reliability diagram contains the discrete forecast values p_i, the y-axis shows the mean conditional observations $\bar{y}_{p_i}$ given a the discrete forecast values. A forecast is perfectly calibrated, if the conditional probability of events equals the forecast value, i.e. the reliability diagram is a perfect diagonal. However, the reliability diagram is only presenting the full joint probability distribution, when it also reveals the relative frequency of the forecasts $P(p_i) = N_i/n$, i.e. the refinement curve. A forecast is perfectly refined, or confident, when only probability values of 100% and 0% are predicted. Thus the refinement curve shows an attribute of the forecast only. The calibration is a joint attribute of forecast and observation (Murphy, 1996).

The Winkler Score By design the Brier score is symmetric, which means that the forecast p given the occurrence of an event is rewarded in the same way as the forecast $1-p$ given no event (cf. equation 2.28). In addition to the Brier score, the Winkler score is introduced. It's score functions are based on the construction rule:

$$WS(p,1) = \frac{S(p,1) - S(c,1)}{T(c,p)}, \quad WS(p,0) = \frac{S(p,0) - S(c,0)}{T(c,p)}, \tag{2.33}$$

where S is the score function of a symmetric score. $T(c,p) = S(0,0) - S(c,0)$ if $p \leq c$, and $T(c,p) = S(1,1) - S(c,1)$ if $p > c$. c works as reference probability. By construction the Winkler score reaches a maximum at 1 for a perfect forecast $p = y$, gets 0 for $p = c$, and is negative for forecast worse than the reference. This scaling equals the scaling of skill scores. Thus the Winkler score offers an alternative to skill scores. If S is a proper scoring rule, it turns out that WS is also a proper scoring rule (Gneiting and Raftery, 2007). Substituting the score functions of the Brier score (equation 2.28) into the construction rule for the Winkler score (equation 2.33) yields

$$WS_{BS}(p,1) = \frac{(p-1)^2 - (c-1)^2}{-(c - H(p-c))^2}, \quad WS_{BS}(p,0) = \frac{p^2 - c^2}{-(c - H(p-c))^2}, \tag{2.34}$$

with the Heaviside step function $H(p-c)$, which is zero for $p \leq c$, and one for $p > c$. Figure 2.5 illustrates the symmetric and asymmetric rewarding of the Brier and the Winkler score, respectively. Note, the Brier score is negative orientated, i.e. higher values mean penalty, and the Winkler score is positive orientated, i.e. higher values mean benefit.

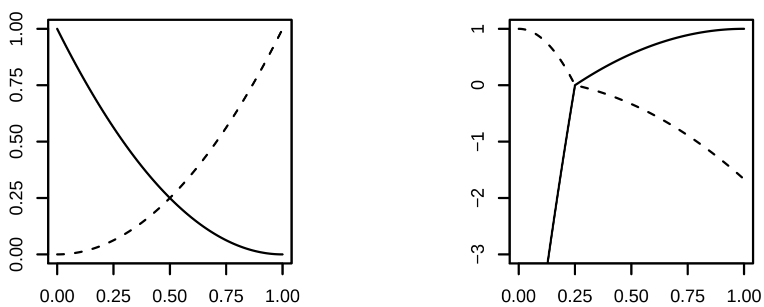

Figure 2.5: Score functions of the Brier score (left) and the Winkler score with $c = 0.25$ (right), solid lines and dashed lines correspond to $S(p,1)$ and $S(p,0)$, respectively.

Cross-validation

Cross-validation is a simple way to split the whole data into a dependent and independent subset of the joint distribution of forecast and observation. Cross-validation is especially applicable when data availability is limited, i.e. when not enough data is on hand to provide one sufficient subset

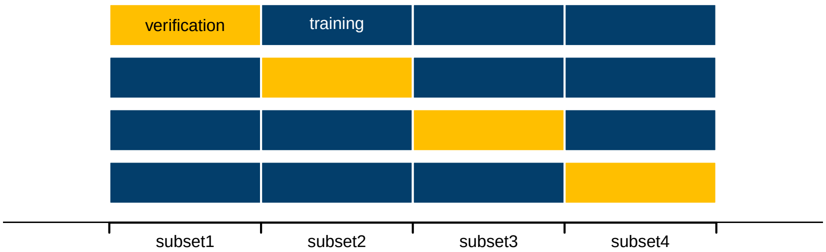

Figure 2.6: A 4-fold cross-validation: Yellow indicates verification subsets, blue training subsets. Each line shows one of four training-and-verification sets, in which three subsets provide training data and one subset verification data.

for training $\mathcal{T}$ and one for verification $\mathcal{V}$. In principle a *k-fold cross-validation* splits the data into k equally sized subsets, $k-1$ of which is assigned to training and the remaining subset is for verification. In total a k-fold cross validation offers k training-and-verification sets. For instance figure (2.6) illustrates a 4-fold cross-validation.

4-fold is a typical choice for cross-validation, but also 5-fold or 10-fold are typical and recommended (Hastie et al., 2008). Given the problem on hand the k might be adjusted. For instance k can be choosen in a way, that the resulting subsets cover temporal scales with non-diminishing auto-correlations: Simon et al. (2013a) applied a 4-fold cross-validation resulting in 10 yrs long subset in order to account for auto-correlations implied by ENSO.

Employing the Brier score (equation 2.27) within a 4-fold cross-validation yields

$$BS_{CV} = \sum_{k=1}^{K=4} \sum_{l \in \mathcal{V}_k} (p_l - y_l)^2. \tag{2.35}$$

The first sum in equation (2.35) runs over the four different training-and-verification sets, i.e. the rows in figure 2.6, and the second sum covers the corresponding verification subset $\mathcal{V}_k$. p_l is the forecast, trained on $\mathcal{T}_k$, for the verification subset $\mathcal{V}_k$.

2.3.3 Analytic Tools

This section summarizes further statistical methods, that were applied as analytic tools in the following chapters. First *empirical orthogonal functions* (EOF) are described, and second spectral analysis is explained. However, the broad spectrum of applications of these methods is not restricted on pure analytics.

Empirical Orthogonal Functions

As mentioned above the EOF analysis is not only a multi-variate analytic tool. As datasets in climate science reveal strong auto-correlations among the variables, the EOF analysis was applied by Lorenz (1956) to reduce the dimensionality of a dataset by accounting for these auto-correlations. The EOF analysis can be thought of as a rotation, or linear transformation, of a dataset onto its principal components, thus the EOF analysis is often refer to as *principal component analysis* (PCA). Within the new rotated system, a major part of the variability is focused on a few modes. In doing so the dimensionality of the dataset is reduced to these few modes. The name says it, the single EOF modes are orthogonal to each other. Though it is common to draw physical meanings out of EOFs, it is important to be aware of pitfalls, e.g. generating artificial modes, coming along with the EOF analysis (Dommenget and Latif, 2002).

The mathematical basis of the EOF analysis is as follows: Assume $\mathbf{X}$ is a $k \times m$ data matrix, with spacial dimension k and temporal dimension m. Further assume that $k < m$. The $k \times k$ co-variance matrix of $\mathbf{X}$ will be denoted as Σ. Solving the eigenvalue problem,

$$\mathbf{\Sigma E} = \mathbf{E\Lambda}, \tag{2.36}$$

yields the $k \times k$ matrix $\mathbf{E}$, where each column represents an EOF E_i. The EOFs are orthonormal to each other, $\mathbf{EE}^T = \mathbf{I}_k$. $\mathbf{\Lambda}$ is a $k \times k$ diagonal matrix containing the corresponding eigenvalues λ_i on the main diagonal. The eigenvalues leads directly to the explained variance $f_i = \lambda_i / \sum_{j=1}^{k} \lambda_j$ of the single mode. Finally, the temporal evolution, or amplitudes $\mathbf{A}$, of the modes can be calculated by

$$\mathbf{A} = \mathbf{\Lambda}^{-1/2}\mathbf{E}^T\mathbf{D}. \tag{2.37}$$

The ith row of the $k \times m$ matrix $\mathbf{A}$ correspond to the temporal evolution of the spatial pattern E_i. This decomposition of the data leads to unit standard deviation of the amplitudes, $\frac{1}{m-1}\mathbf{AA}^T = \mathbf{I}_k$. In general, the mean state and the elements of the co-variance matrix can be estimated via standard estimators in most applications.

The construction of EOFs leads to k modes. A truncation criterion for the modes sorted by decreasing explained variances is given by Bretherton et al. (1999),

$$N_{eff} = \frac{\left(\sum_{i=1}^{k} \lambda_i\right)^2}{\sum_{i=1}^{k} \lambda_i^2} = \left(\sum_{i=1}^{k} f_i^2\right)^{-1}. \tag{2.38}$$

N_{eff} is an estimate for the *effective number of spatial degrees of freedom* associated with the time-varying field X. Thus, it is reasonable to keep the N_{eff} leading modes only.

There are several variation of the EOF decomposition, e.g. the Varimax rotation (Kaiser, 1958) takes J leading EOFs as a subset the original k EOFs, and seeks a new basis by maximizing the so-called *simplicity* of the spatial patterns,

$$\mathbf{E}_{VARIMAX} = \arg\max \left(\sum_{j=1}^{J} \left(\sum_{i=1}^{k} e_{i,j}^4 - \frac{1}{k} \left(\sum_{i=1}^{k} e_{i,j}^2, \right)^2 \right) \right). \tag{2.39}$$

where $e_{i,j}$ denotes the element of $\mathbf{E}_{VARIMAX}$ in row i and column j. This maximizes if only a few space points have large amplitudes. The outcome of this optimization problem is a basis containing more compact or localized patterns, i.e. high order multi poles are suppressed, than found by EOF analysis.

Cross-spectral Analysis

Before introducing cross-spectra, a definition of the uni-variate spectrum Γ_{xx} of the random process X should be given,

$$\Gamma_{xx}(\omega) = \mathcal{F}\left\{\gamma_{xx}\right\}(\omega) = \sum_{\tau=-\infty}^{\infty} \gamma_{xx}(\tau) e^{-2\pi i \tau \omega}, \quad \forall\, \omega \in [-0.5, 0.5], \tag{2.40}$$

where $\mathcal{F}$ is the Fourier transform, and γ_{xx} is the auto-covariance function of X. The spectrum is real-valued and symmetric, i.e. $\Gamma(-\omega) = \Gamma(\omega)$. The cross-spectrum of the random processes X and Y,

$$\Gamma_{xy}(\omega) = \mathcal{F}\left\{\gamma_{xy}\right\}(\omega) = \sum_{\tau=-\infty}^{\infty} \gamma_{xy}(\tau) e^{-2\pi i \tau \omega}, \quad \forall\, \omega \in [-0.5, 0.5], \tag{2.41}$$

is the Fourier transform of the cross-covariance function γ_{xy} of X and Y. The cross-spectrum is complex-valued,

$$\Gamma_{xy}(\omega) = \Lambda_{xy}(\omega) + i\Psi_{xy}(\omega) = A_{xy}(\omega) e^{i\Phi_{xy}(\omega)}, \tag{2.42}$$

with the real part Λ_{xy} and the imaginary part Ψ_{xy} in Cartesian coordinates, and with the amplitude spectrum A_{xy} and the phase spectrum Φ_{xy} in polar coordinates. The latter can also be expressed in dimensionless units,

$$\kappa_{xy} = \frac{A_{xy}^2(\omega)}{\Gamma(\omega)\Gamma_{yy}(\omega)}, \tag{2.43}$$

where κ_{xy} is denoted as *coherency spectrum*, or *squared coherency spectrum*. The coherency can be thought of as the squared correlation depending on the frequency (von Storch and Zwiers, 2002).

Estimators for the spectrum and cross-spectrum are based on the *periodogram* and *cross periodogram*, respectively. The periodogram of the time series $\mathbf{x} = \{x_1, x_2, \ldots, x_T\}$, and the cross periodogram of the time series $\mathbf{x}$ and $\mathbf{y} = \{y_1, y_2, \ldots, y_T\}$ are defined by,

$$I_{xx,j} = \frac{T}{4}\left(a_{x,j}^2 + b_{x,j}^2\right), \quad \text{and} \quad I_{xy,j} = \frac{T}{4}\left((a_{x,j} + ib_{x,j})(a_{y,j} - ib_{y,j})\right), \tag{2.44}$$

where $a_{x,j}$ and $b_{x,j}$ denote the coefficients of a discrete Fourier transform of the time series $\mathbf{x}$,

$$a_{x,j} = \frac{2}{T}\sum_{t=1}^{T} x_t \cos(2\pi\omega_j t) \quad \text{and} \quad b_{x,j} = \frac{2}{T}\sum_{t=1}^{T} x_t \sin(2\pi\omega_j t). \tag{2.45}$$

Analog the Fourier transform coefficients of the time series $\mathbf{y} = \{y_1, y_2, \ldots, y_T\}$ are defined as $a_{y,j}$ and $b_{y,j}$. However, periodograms are not good estimators for the spectra. In particular, the periodogram and the cross periodogram lead to unity at all frequencies for the estimated coherency spectrum,

$$\hat{\kappa}_{xy}(\omega_j) = \frac{|I_{xy,j}|^2}{I_{xx,j} I_{yy,j}}. \tag{2.46}$$

Thus, smoothing techniques for the periodograms have to be applied. In the following the *Daniell Spectral Estimator* and the *Chunk Spectral Estimator* are introduced (von Storch and Zwiers, 2002).

The Daniell Spectral Estimator is a moving average applied over the values of the cross periodogram,

$$\hat{\Gamma}_{xy}(\omega_j) = \frac{1}{n} \sum_{k=j-(n-1)/2}^{j+(n+1)/2} I_{xy,k}, \tag{2.47}$$

or the periodogram, which can be calculated in an analog way. n is an odd integer, and defines the window, on which smoothing is applied. For the assessment of confidence intervals, it is important to know the equivalent degrees of freedom r of a spectral estimator. In case of the Daniell estimator r is determined by $r = 2n$.

For the Chunk Spectral Estimator the data is split into m equally sized chunks. The cross periodogram for each chunk is estimated independently. Finally, the cross spectrum is estimated by averaging the cross periodograms,

$$\hat{\Gamma}_{xy}(\omega_j) = \frac{1}{m} \sum_{l=1}^{m} I^l_{xy,j}. \tag{2.48}$$

The superscript l corresponds to the cross periodogram calculated for chunk l. The spectrum can be estimated in an analog way replacing cross periodogram with periodogram. The Chunk Spectral Estimator results in $r = 2m$ equivalent degrees of freedom.

Given the equivalent degrees of freedom r of the spectral coherency estimator $\hat{\kappa}_{xy}$, one can approximate the $\alpha \times 100\%$ confidence intervals by

$$conf_\alpha = \left(\tanh\left(\tanh^{-1}\left(\sqrt{\hat{\kappa}_{xy}(\omega)}\right) \pm \frac{q_{(1+\alpha)/2}}{\sqrt{r}}\right)\right)^2, \tag{2.49}$$

where $q_{(1+\alpha)/2}$ is the $(1+\alpha)/2$ quantile of the standard normal distribution $\mathcal{N}(0,1)$ (von Storch and Zwiers, 2002).

Chapter 3

Dynamical Downscaling

In this chapter the aspects regarding dynamical downscaling are highlighted. First, the technical side of the generation of RCM simulations, and a first evaluation of the simulated physical processes are discussed (section 3.1). Afterwards, the evaluation of the added value of RCM simulations with respect to their driving GCM is discussed (section 3.2). In particular, a method is presented for the first time to quantify the temporal scales, on which the RCM simulation has the potential to generate variability on its own. The method will be applied on the RCM data presented previously. This example illustrates, how the method helps to understand the dynamical downscaling procedure better. To close the chapter, additional analyses concerning the calibration of precipitation distribution and the detection of changes in the second nesting step are presented (section 3.3).

3.1 RCM Simulations

The developing phase of a RCM setup is intensive in the amount of work and includes designing, performing and evaluating the simulations. The simulations or rather the experiment has to be planned with care, and there are several points within the planning phase where experimental design and simulation design are overlapping. In the following the general aspects of design, and some specific examples of the development of the COSMO-CLM setup for the East Asia domain are presented.

- All available RCMs represent best-effort attempts to simulate dynamics on higher resolutions, and to allow for a coupling of the limited area model with its LBC. Thus, the *choice of RCM* is to a certain degree arbitrary. One possible selection criterion is the experience that the model performs well in the area of interest, but also the technical experience of the researcher or the research group in using a certain RCM might influence the selection of the RCM. For the simulations of the climate in East Asia COSMO-CLM (Rockel et al., 2008) was selected, because there is a general interest within our research group about the performance of COSMO-CLM under different conditions.

- The type of *lateral boundary conditions* (LBC) directly influences the experimental design.

The LBC come from a global climate model, in which assumptions about boundary conditions of the whole climate system are already employed. Therefore, the climate scenario employed is a crucial part of the experimental design. The choice of global model is arbitrary to a certain degree, as all models developed with in the CMIP framework are best-effort attempts of modeling the global climate system from different research groups. Non of the models can be rated *better* in modeling climate than another model (Taylor et al., 2012). The uncertainty introduced by the arbitrary choices of both RCM and global model have to be accounted by employing a variety of RCM and LBC serving global models in an ensemble approach (e.g., Mearns et al., 2012; Jacob et al., 2013).

The basic idea of the experimental design for the East Asia simulation was to come up with one simulation appropriate for evaluating the performance of the model in this specific region and configuration, one simulation for the past climate, one simulation for the future climate. The LBC for the evaluation run was served by ERA-40 (Uppala et al., 2005). All other runs were forced by ECHAM5 (Roeckner et al., 2003) run No. 3. The simulation for the past was forced by the ECHAM5 20th century simulation including both natural and anthropogenic forcing. For the simulation of the future period the A1B scenario was selected (Nakicenovic et al., 2000). Run No. 3 was applied according to prior agreement with a collaborating research group[1], who focused on dynamical downscaling of ECHAM5 run No. 1 with COSMO-CLM and the same numerics. The ECHAM5 simulation of the climate during the 20th century was driven by anthropogenic forcing only. The applied ECHAM5 simulations fall into CMIP phase 3 (Meehl et al., 2007).

- *Setting the domain* includes several decisions influencing each other. The region of interest determines the location and extend of the domain. However, the question of horizontal resolution is also part of the experimental setup. Nevertheless, these two design parameters influence each other. On the one hand, computational issues limit the domain extend and resolution. On the other hand, the applied grid ($n \times m$) has to be sufficiently large to reduce boundary artifacts and to allow the RCM to develop internal variability in the inner domain on its own (Simon et al., 2013b). Furthermore, the resolution is limited due to the ratio between RCM resolution and resolution of the global model, which must not exceed a factor of 6–8 (Rummukainen, 2010). Finally, the width of the lateral relaxation layer (or often called sponge zone) has to be defined. This zone should help the dynamics to adapt to the finer resolution and to reduce boundary artifacts.

  The domain configuration for the East Asia simulations were chosen in alignment with CORDEX guidelines[2]. This led to appropriate downscaling factor between the horizontal resolution of the driving model and the RCM, and to a sufficient grid size to ensure the generation of internal variability. Details of the grid specification for the simulations are given in Table 1 of

[1]Christoph Menz from PIK working on the BMWF funded *Guating project*.

[2]However, the simulations do not fully meet CORDEX guidelines. In our simulations a CMIP3 model provides the LBC, instead of a CMIP5 model, which is one of the CORDEX requirements.

Appendix A.

- To finalize the simulation design physical parameterizations have to be adapted to the region of interest and to the numerical setup. A specific configuration might show a different behavior on different grid resolutions, e.g., the parameterization of convective precipitation on a coarse grid (50 km) has to include more sub-scale processes, like the horizontal drift of air masses at the top of the convection column, than on a fine grid (7 km), where these processes should be partly modeled dynamically (Kuell et al., 2007). A different region can lead to different behavior of the physical parameterizations (Wang et al., 2013), e.g., the tropopause height plays an important role in the parameterization of convection and it changes from about 16 km height in the tropics to about 8 km at the poles. The latter point was of special importance for the East Asia simulations. Basically, COSMO-CLM was developed for European conditions, and is mostly applied to those. The East Asia domain extends across the equator, which made an adaption of the Rayleigh sponge damping layer height to 13 km necessary. This Further description of adapted numerics and physics for the East Asia downscaling can be found in section 2.2 *Model configuration* and Table 2 of Appendix A. These settings were found after several test runs of two exemplary years.

A first assessment of the performance of the simulations over the whole simulation periods is undertaken by a comparison with gridded observational data. For 2 m temperature and precipitation the CRU-TS 3.0 (Harris et al., 2013) and the APHRODITE (Xie et al., 2007) datasets have been applied, respectively. Both datasets are derived from pointwise observations, that have been post-processed by a statistical model. This results in a gridded interpretation of the pointwise observations. By construction these datasets have their own uncertainties, which are not accounted for in the applied investigation.

Biases of mean temperature and annual precipitation sums between the simulations concerning the past (ERA-40 driven and ECHAM5 20th century driven) and the gridded observation datasets are revealed. Strongest biases in all simulations can be found for annual precipitation sums in East Indonesia, Tarim Basin, and Tibetan Plateau (cf. Table 3–5 in Appendix A). These regions come with special geographical features. The Tibetan Plateau has a high elevation, and the Tarim Basin is surrounded by high mountain chains isolating this area. East Indonesia is exposed to tropical dynamics, where shifts of the ITCZ can make a huge difference in precipitation sums. More details about the comparison between the simulations and the gridded data is given in Appendix A section 3.

In addition to the investigation of the biases the ECHAM5 20C run No. 3 driven COSMO-CLM simulation was checked for dynamical processes specific to monsoon dynamics in East Asia. For each monsoon season (summer and winter) one example of the most important feature for the particular system is presented. The quasi-stationary frontal system in summer gets disturbed by cyclonic meso-α-scale vortices. These vortices are well resolved in the COSMO-CLM simulations (cf. figure 4, Appendix A). In winter cold air extensions originating in the Siberian-Mongolian-High cover East China. The development of such a cold surge is well presented in COSMO-CLM (cf.

figure 5, Appendix A).

3.2 Added Value

A quantitative evaluation of the RCM performance is crucial in the whole dynamical downscaling process, because a quantification can be added to the RCM output as kind of metadata. This would help end-users of RCM output to handle the data more confidently. Assessing the added value of a RCM with respect to the global model serving the boundary conditions is of special interest in this context.

Dynamical downscaling became established within the last two decades (Giorgi et al., 2001; Rummukainen, 2010), and first co-operative research efforts have been arranged during the last five years (Giorgi et al., 2009; Mearns et al., 2012; Jacob et al., 2013). Therefore, the toolbox for assessing added value properly and in comprehensive way is not completely filled yet. There is still demand for basic research about the evaluation of RCMs, and for studies focusing on the comparison of RCM output and the driving models (Feser et al., 2011; Laprise et al., 2012). Summarizing research undertaking in this field three categories of added value can be identified.

1. Added value can be defined as the capability of the RCM to reproduce the *truth*, i.e. observations or a virtual reality, better than the simulations performed with the global model. Both comparisons an day-to-day scale, e.g. reproducing weather, and comparisons of statistics over longer period as estimates for the climate fall within this category. A comparison with respect of reproducing weather is often applied to RCMs driven by re-analysis data (Feser, 2006; Winterfeldt and Weisse, 2009). Though a RCM driven by global re-analysis data differs from a regional re-analysis, where data-assimilation is integrated into the regional model (Mesinger et al., 2006; Bollmeyer et al., 2014). A comparison of climatological values is also possible when the RCM was driven by climate simulation (Di Luca et al., 2012).

2. In the second category added value is defined according to a gain of spatial small-scale variability. This kind of added value is assessed by direct comparison between driving model and downscaled version. Technically, the gain of spatial small-scale variability is often estimated by spatial spectral analysis (Errico, 1985). Another way to quantify added value according to this definition is the implementation of the so-called Big-Brother experiment. The reader is referred to Denis et al. (2002) for more information about this special kind analytic tool.

3. Analog to the assessment of added variability on small spatial scale, added value can also be defined as a gain of small-scale variability on temporal scales. Direct comparison of RCM and GCM should give insights on which temporal scales the RCM act independent from the driving GCM, and therefore adds value.

A comprehensive overview of the literature on added value is given in the introduction of Appendix B. A contribution to the field of evaluating the added value of a RCM simulation is presented in Appendix B. The method, newly developed and presented for the first time, can be sorted into the

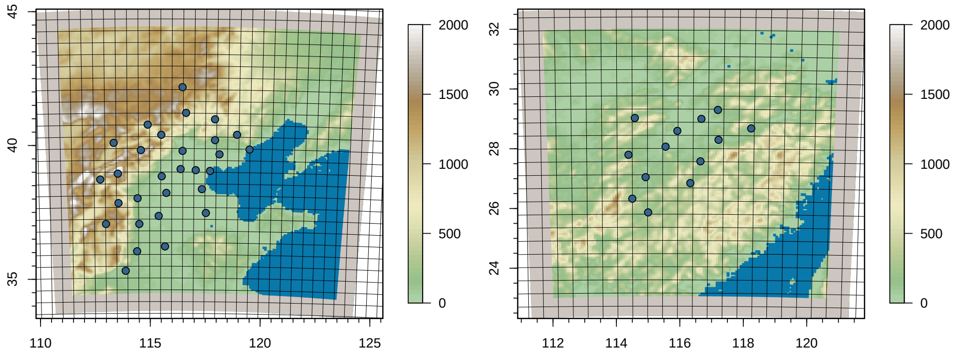

(a) Haihe orography (b) Poyang orography

Figure 3.1: Orography [m a.m.s.l.] of the Haihe (left) and Poyang (right) domain at 7 km resolution. The points mark the locations of the rain gauges. The overlying grid indicates the 50 km resolution of the driving model. The gray frame represents the sponge zone.

third category of added value listed above. A cross-spectral analysis is applied point-to-point between the RCM output and a bi-linearly interpolated version of the driving model. The cross-spectrum contains both the coherence and the phase spectrum (von Storch and Zwiers, 2002). In this setup, the coherence spectrum is richer in content, and further investigations focus on that part.

The method was applied to surface temperature, and to temperature and humidity in the lower troposphere at 850 hPa. The applied data is described in section 3.1. The spatial coherence pattern are related to atmospheric dynamics in East Asia, e.g., monsoons and inter-tropical convergence zone (ITCZ). Furthermore, another application to data from a second nesting step, i.e, from 50 km to 7 km horizontal resolution, reveals the vast difference in temporal scale, on which the regional models are starting to uncouple from their driving models. In the 50 km runs internal variability was generated by COSMO-CLM on temporal frequencies between 1/yr and 1/month. In contrast, for the second nesting step uncoupling was found not before the daily-scale (Simon et al., 2013b).

After all, as the study (cf. Appendix B) introduces the method for the first time, there is a bunch of questions raising. On the one hand there is no proper way to apply a hypothesis test whether self-generated variability is significant (cf. section *Conceptual model* in Appendix B). On the other hand more applications, in particular applications to RCM ensembles, are necessary to estimate the sensitivity of coherence structures on changes in the experimental design of RCM simulations. Such changes can relate to the choice of domain size, sponge zone, RCM, GCM providing LBC, and so on.

3.3 Additional Analysis

For the additional analysis of RCM output emphasis is put on the precipitation output of the double-nesting runs with 7 km resolution, as the results and technical details for the runs with 50 km are already conducted in Appendix A (Wang et al., 2013). The model output of the simulations with

7 km resolution was applied in the study, which was described in the previous section about added value of RCMs (Simon et al., 2013b), and an overview of performed simulations can be found therein (Appendix B, Table 1). Figure 3.1 shows a detailed picture of the orography at 7 km resolution, and gives an idea of the difference in resolution from the first nesting step (50 km) to the second nesting step, as about 50 7 km×7 km grids fit into one 50 km×50 km box.

Calibration of rainfall distributions

Precipitation can take place on small spatial scales, e.g. convective events, and thus cannot be resolved by coarse GCMs directly, but these processes have to be parameterized. One motivation of dynamical downscaling approaches or simulation with high resolution GCMs is to resolve more processes, and be less dependent on parameterizations. The horizontal resolutions of the performed COSMO-CLM simulations, i.e. 50 km and 7 km, are still too coarse to resolve convective processes in a proper way. A Tiedtke convection scheme (Tiedtke, 1989) is applied in all simulations (Simon et al., 2013b; Wang et al., 2013).

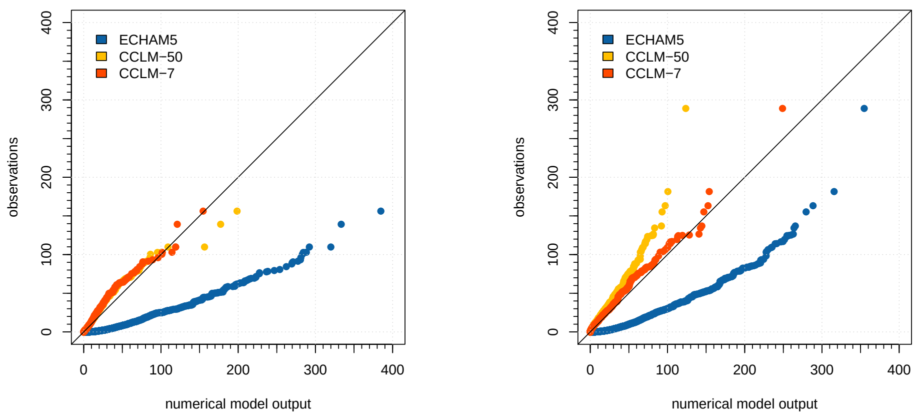

(a) Beijing rain gauge

(b) Nanchang rain gauge

Figure 3.2: QQ-plots for 24 h accumulated precipitation (in mm). The results for two rain gauges are presented, Beijing rain gauge (left) and Nanchang rain gauge (right), exemplarily for the two catchments.

QQ-plots are applied to compare local rainfall distributions observed at the rain gauges and the rainfall distributions simulated by the RCMs in the grid cells, in which the rain gauge is located (figure 3.2). The locations of the applied rain gauges are presented in figure 3.1. In addition to the COSMO-CLM output, the corresponding modeled precipitation values of ECHAM5 20C3M run no.1 (anthropogenic and natural forcing), which delivered the LBC for the dynamical downscaling, is included in the qq-plots. The precipitation output of the numerical models may only be interpreted as an average value over the grid cell. Nevertheless, the rainfall distributions taken from COSMO-CLM are closer to the distributions of the observations, than the ones from ECHAM5. The QQ-plots for the Beijing rain gauge (figure 3.2a) show close results for COSMO-CLM 50 km and COSMO-CLM 7 km. In contrast, for the Nanchang station (figure 3.2b) the curve of COMSO-CLM 7 km reveals

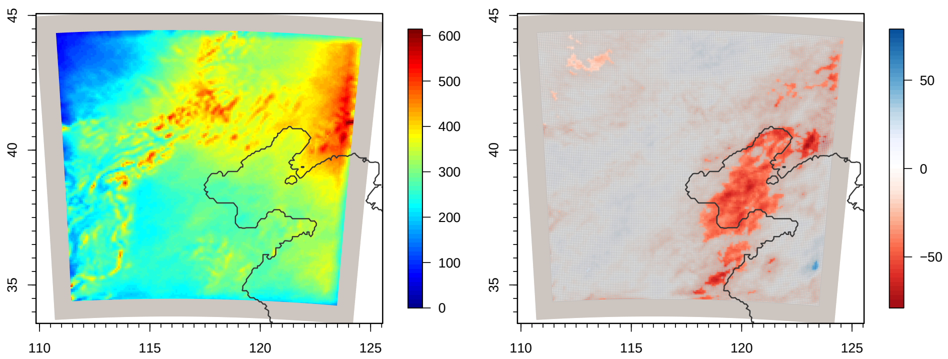

(a) mean JJA sums (b) difference from mean JJA sums

Figure 3.3: Point-to-point mean JJA precipitation sums (mm) for the 7 km Haihe domain over the whole simulated period 1971–2000 and 2021–2050 (left), and differences between the mean state of each period and the overall mean (right). Positive (negative) values indicate higher sums in the 2021–2050 (1971–2000) period. Points where the difference is not significant at 1% level are shaded.

improved calibration[3] in comparison to the curve for COSMO-CLM 50 km. These features discussed for the two station are common to the most QQ-plots of the other stations in the corresponding catchment.

Detection of future changes

In this subsection the mean states of precipitation sums will be discussed, and whether a change in precipitation properties, i.e., sums and block maxima, from the 20C to the 21C runs with COSMO-CLM 7 km can be detected on the available grid-scale. The signal-to-noise ratio decreases when time series representing smaller spatial scales are investigated. For instance, it is more likely to detect climate change on the global scale than on the local scale (Taylor et al., 2012).

However, the applied techniques cannot answer the question of climate change in the regions of interest sufficiently. A comprehensive analysis of detection, and in consequence of attribution, is only possible with an appropriate ensemble of simulations. Within the climate research community change is detected *if its likelihood of occurrence by chance due to internal variability alone is determined to be small* (Hegerl et al., 2010). An estimate for the spread explainable by internal variability can only be assessed by an ensemble approach. In this light the term *detection* as defined here differs from the definition given by Hegerl et al. (2010). For the sake of completeness, attribution of climate change, which evaluates *the relative contributions of multiple causal factors to a change* (Hegerl et al., 2010), requires a number of ensembles each accounting for a different forcing, i.e. natural forcing, anthropogenic forcing, natural plus anthropogenic forcing.

[3] I.e. marginal calibration according to Gneiting et al. (2007). This is the only mode of calibration that can be discussed for climate simulations. This mode of calibration relies on the assumption of a stationary climate over the simulation period.

The simulated mean precipitation sums during summer period (from June to August), exhibit values between 50 mm in the very Northwestern part of the domain, and around 600 mm in the Northeastern part of the Haihe domain above the land (figure 3.3a). On the Northern, Eastern and Southern boundary of the domain a line of relatively low precipitation values, compared to the values further inside, are visible. This indicates the influence of adaptation processes of the water cycle to the finer grid. In the inner domain both very high values (>500 mm) and very low values (<200 mm) can be found in the mountainous region. A smoother picture with values between 200 mm and 400 mm can be found in the center of the domain and above the sea. Changes in mean JJA precipitation sums between the two simulated periods, i.e. 1971–2000 (past) and 2021–2050 (future), are most prominent in their spatial extend above the Bohai Gulf, which is the most inner gulf of the Chinese Sea. Deviations of more than 50 mm from the mean state are revealed, which equals a difference of about 100 mm between the past and the future, with a dryer climate in future times.

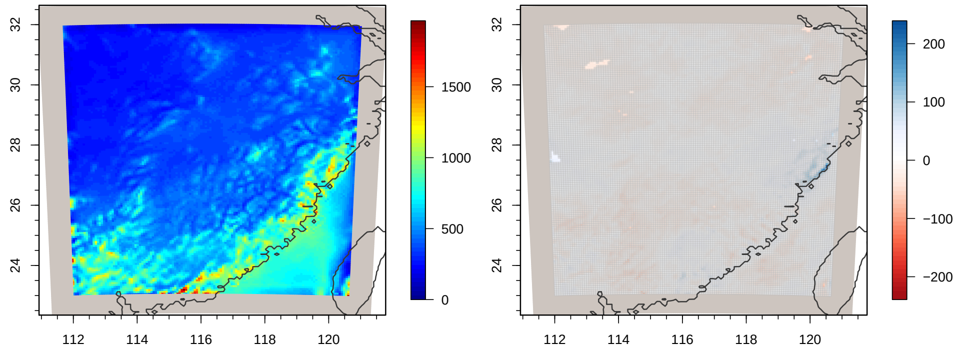

(a) mean JJA sums (b) difference from mean JJA sums

Figure 3.4: Point-to-point mean JJA precipitation sums (mm) for the 7 km Poyang domain over the whole simulated period 1971–1997 and 2021–2050 (left), and differences between the mean state of each period and the overall mean (right). Positive (negative) values indicate higher sums in the 2021–2050 (1971–1997) period. Points where the difference is not significant at 1% level are shaded.

In the Poyang domain (figure 3.4a) the absolute mean precipitation sums are partly higher than in the Haihe domain. Similar to the results for the Haihe domain is a zone with relatively low values due to boundary effects. Lowest values (200 mm–400 mm) occur in the Northwestern corner of the domain. Values are increasing in Southeast direction, with summer precipitation sums between 400 mm and 600 mm in the Poyang catchment, which is located in the center of the domain. Highest values (1000 mm–1800 mm) can be found locally in the coastal area and in the South, where complex mountainous terrain is dominating the landscape (figure 3.1b). Over the sea precipitation sums lie around 800 mm, but the spatial structure seems to be strongly influenced by the boundary. Hardly any changes between the simulation of the past and the simulation of the future detected (figure 3.4b). This absence of detection can be interpreted in two ways. First, the signal-to-noise ratio at the 7 km resolution is low, and in turn detection of change is unlikely (Taylor et al., 2012). Second, the EASM and associated precipitation have a strong year-to-year variability by nature (Li et al., 2010), which also leads to a low signal-to-noise ratio.

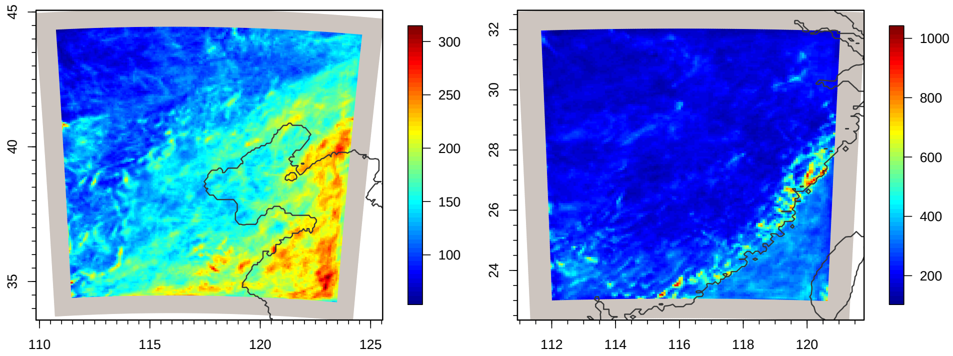

(a) Haihe domain (b) Poyang domain

Figure 3.5: Point-to-point GEV based estimates for 20 year return levels of daily summer precipitation events (in mm).

Finally, point-to-point estimates for 20 year return levels[4] for the two domains are given (figure 3.5). A general extreme value (GEV) distribution was fitted to seasonal block maxima via maximum likelihood (ML) estimator. The GEV contains three parameters for location, scale, and shape (Coles, 2001). As the domains covers a large area with complex orography and mixed land surface characteristics, strong variations in the shape parameter were found. In order to suppress very high and very low values of the shape parameter a penalty term was integrated into the ML estimator. The penalty term is a beta distribution prior defined on $[-0,5;0,5]$ and a mode of $0,1$, leading to a generalized ML estimator favoring values between $-0,1$ and $0,3$ for the shape parameter (Martins and Stedinger, 2000).

In the Haihe domain the 20 year return levels vary from about 50 mm in the Northwestern part of the domain to about 300 mm over the Chinese Sea (figure 3.5a). Thus, the spatial structure of the return levels differs form the one of the mean precipitation sums (figure 3.3a). In the Haihe catchment, which is located in the center of the domain, values are ranging between 100 mm and 150 mm with some spots reaching about 200 mm. These results are consistent with estimates obtained from local observations (cf. section 4.1).

The return levels in the Poyang domain (figure 3.5b) reveal a less smooth picture than the ones in the Haihe domain. In the coastal region and in the mountainous region in the South values exceed 500 mm and even reach more than 1000 mm locally. Over the sea return levels ranging between 250 mm and 400 mm can be found. In the center, and in the North and West of the domain values lies between 150 mm and 250 mm, but can also reach up to 350 mm locally. The values for the Poyang catchment, located in the center of the domain, are consistent with the 20 year return levels

[4]A 20 year return level means that the probability of exceeding this value by the seasonal maxima is 5% in each single year.

estimated from local observations (cf. section 4.1).

By likelihood ratio test (Coles, 2001) it was tested whether a GEV containing a linear model for the location parameter outperforms a GEV constant in all parameters. The employed linear model allows different values for the location parameter in each simulated period, i.e. past and future, but constant within each period. Neither for the Haihe domain nor for the Poyang domain large areas could have been detected, where the GEV with the linear model is significant better than the GEV constant in all parameters. Therefore, the figures showing the deviations of the return levels for each simulated period are omitted.

Chapter 4

Statistical Downscaling

Next to dynamical downscaling the field of statistical downscaling offers a computational feasible way to change the corresponding support of a time series. Statistical downscaling links large scale information to local scale information. Therefore a good observational database is required for producing a practical downscaling scheme. The local observation available for the regions of interest are preliminary examined (section 4.1) before the statistical downscaling scheme is developed. In an example study employing statistical downscaling special issues about the generation of physically meaningful predictors are emphasized (section 4.2).

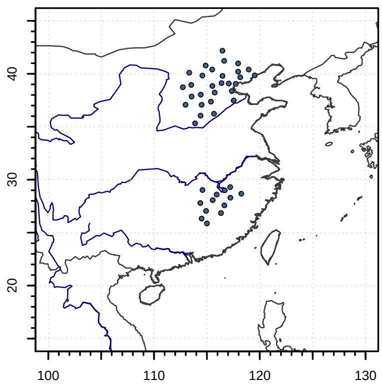

Figure 4.1: The map shows the Eastern part of China. The points mark the locations of the rain gauges in the Hai He Basin in the North and in the Poyang Basin in the South. For orientation major rivers are displayed – from the North to the South: Huang He (*Yellow River*), Chang Jiang (*Yangtze*), Zhu Jiang (*Pearl River*) and Mekong

4.1 Preliminary Analysis

Data availability

The measurements of 42 rain gauges have been made available for the research presented in this work. 13 and 29 of the stations are located in the Poyang catchment, in the South, and the Haihe catchment, in the North, respectively (figure 4.1). Temporal coverage is given from 1960 to 1999 with a daily resolution of 24 h accumulated precipitation sums.

Precipitation climatology

For each catchment a representative station was selected to discuss the precipitation climatologies in each catchment. For the North the rain gauge in Beijing was selected (figure 4.2), and for the South the one in Nanchang (figure 4.3). The annual numbers give a picture of a wet climate in the Yangtze valley, with 1588 mm of annual rain on 148 days and a 95. quantile of about 25 mm. In contrast, Beijing has an annual precipitation sum of 579 mm on 73 days and a 95. quantile of 7.7 mm.

	JAN	FEB	MAR	APR	MAY	JUN	JUL	AUG	SEP	OCT	NOV	DEC	
monthly sum [mm]	2.5	5.4	8.6	24	30.9	71.4	187.9	170.6	47.6	20.4	7.2	2.4	$\sum$578.9
rainy days ≥ 0.1mm	1.8	2.6	3.6	5	5.8	9.7	14.2	12.4	7.4	5.3	4	1.6	$\sum$73.3
95. quantile of daily values [mm]	0.1	0.8	1.5	4.4	5	12.7	38.9	33.1	10.4	2.9	0.9	0.1	7.7

Figure 4.2: Precipitation climatology of Beijing rain gauge, lon: $116.5°$E lat: $39.8°$N, over the period 1960–1999. The values on the right side of the table indicate average annual sum, average number of rainy days per year, and the 95. quantile of daily values over the whole period.

The climatologies can be linked directly to the phases of the EASM. The first rain season occurring in the year is the pre-summer rain season over the Yangtze valley. From March to May the monthly precipitation sums are high together with many rainy days. In June the Meiyu season gets visible in the climatology of Nanchang, where the highest monthly precipitation sum can be observed, be the rain is distributed over less days. Although the Meiyu season often extends until mid July, the whole July is not that pronounced in the climatology.

	JAN	FEB	MAR	APR	MAY	JUN	JUL	AUG	SEP	OCT	NOV	DEC	
monthly sum [mm]	67.6	97.7	169	223.8	249.7	301.5	136.7	114.2	72.6	55	58.1	42.1	$\sum$1588.1
rainy days ≥ 0.1mm	12.5	13.2	18.2	17.8	17.1	15.3	10.1	9.7	7.6	8.9	8.8	8.8	$\sum$148.1
95. quantile of daily values [mm]	12.5	20.1	25.6	36.5	41.2	58	25.7	22.8	14.8	9.4	12.6	9.3	24.8

Figure 4.3: Precipitation climatology of Nanchang rain gauge, lon: $115.9°$E lat: $28.6°$N, over the period 1960–1999. The values on the right side of the table indicate average annual sum, average number of rainy days per year, and the 95. quantile of daily values over the whole period.

In the northern part of East China, i.e. Beijing rain gauge, the rain season related the EASM occurs during July and August. Throughout the rest of the year this region of China gets almost no precipitation, which is related to the cold and dry climate due to EAWM dynamics.

Next, a block maxima approach of extreme value theory should give an overview about the climatological return levels of local summer (June to August) rainfall events in both catchments. As parametric model for the extreme value distribution the *Gumbel* distribution was selected. It has two parameters one for the location and one for the scale, in contrast to the *generalized extreme value* distribution (GEV), which consists three parameters for its location, scale and shape. This selection is based on a likelihood ratio test, that suggested to favor the GEV only for 5 stations in the Haihe catchment and for none in the Poyang catchment.

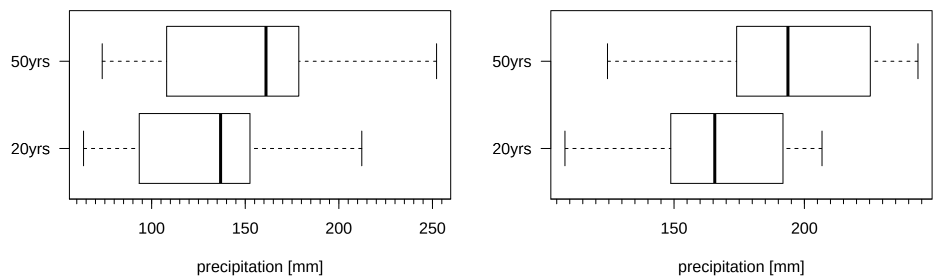

(a) Haihe catchment (b) Poyang catchment

Figure 4.4: Return levels, estimated via Maximum-likelihood fit of Gumbel distribution, at the rain gauges for the period from 1960 to 1999. Within Haihe catchment (left) 29 station are located. Within Poyang catchment (right) 13 stations are located.

The return levels in the Poyang catchment, where the bulk of return levels ranges from 150 mm to 185 mm, are higher as in the Haihe catchment, where only a few outliers reach high return level values 4.4. Via profile likelihood uncertainties of the return levels are assessed (Coles, 2001). Exemplarily, the uncertainties for Beijing rain gauge in the North and Nanchang rain gauge in the South are presented. For Beijing the estimates for the 20 year and 50 year return levels and associated 95% confidence levels are 135,6 mm (117,3 mm; 160,8 mm) and 157,7 mm (135,1 mm; 189,3 mm), respectively. In the same way, 174,1 mm (152 mm; 204,7 mm) and 201,1 mm (173,7 mm; 239,5 mm) are the estimates for the Nanchang rain gauge.

Detection of changes in precipitation properties

To get a better feeling for the provided observational data, and get an own picture about climate change during the second half of the 20th century, precipitation sums are analyzed with respect to linear trends. Significance in this section was tested according to F-statistics at the 5% level (Wilks, 2011). From 29 stations located in the Haihe catchment 5 show a significant linear trend with negative sign for annual precipitation sums, and there is no station with a positive trend. Zooming in to the summer season (June to August) only one station with a significant trend remains. In the

Poyang catchment 3 out of 13 stations show a significant linear trend with a positive sign, and 8 out of these 13 stations show a positive trend for the summer season.

Thus, the observational data exhibits the *drying of the North, flooding of the South* pattern, but it is not as pronounced as found by other studies (Wang and Zhou, 2005; Zhai et al., 2005). The results for the North suggest that the *drying* can not be explained by changes in EASM dynamics only. In contrast, the *flooding of the South* during EASM season gets very clear in the rain gauge data.

Analog to the sums a detection test was applied to investigate whether a change in the distribution of extremes occurred in the second half of the 20th century. Here, a model $\mathcal{M}_1$ with linear trend in the location parameter is compared relative to a model $\mathcal{M}_0$ constant both parameters of the Gumbel distribution, location and scale. Via likelihood ratio test (Coles, 2001) a decision is made whether to reject the model $\mathcal{M}_0$ in favor of model $\mathcal{M}_1$. The *drying of the North, flooding of the South* pattern is hardly visible in the observed maxima for the summer season. Only for one stations in the North a significant (at 5% level) negative trend for the location parameter can be found (no positive trends were detected), and in the South the observed extremes for only one station show a significant positive trend (no negative trends were detected).

4.2 Pattern-based Downscaling

The local observations represent the *predictand* of the statistical model that is supposed to link large scale and local scale information. On the other side of the transfer function *predictors* that provide skillful information with respect to the predictand are required. Additionally to the skillfulness of the predictors, it is desired to have physically meaningful predictors available, that allow further interpretation of the outcome of the statistical downscaling procedure. The generation of such meaningful predictors is presented in an example study (Appendix C).

The predictands in this application were build by transforming local precipitation observations to dichotomous variables indicating whether a certain threshold is exceeded or not. The predictors were created by post-processing ERA-40 output. As ERA-40 output contains tens of variables globally and partly on up to 60 vertical levels (Uppala et al., 2005), a pre-selection and a reduction of dimensions has to be applied. The pre-selected variables were either well known for characterizing EASM dynamics or variables that already proved their skill in other studies about downscaling precipitation. Spatially a 16×16 grid neighborhood around the region of interest, i.e., Poyang catchment, was selected. A reduction of dimensions was archived by both empirical orthogonal functions (EOF) and rotated EOFs (Jolliffe, 2002). Logistic regression was chosen for linking predictand and predictors (Wilks, 2011). The statistical models are verified by cross-validation (Efron and Tibshirani, 1993; Hastie et al., 2008) and proper scoring rules, i.e., Brier skill score and Winkler score (Gneiting and Raftery, 2007). For the four-fold cross-validation the four decades were split into three decades for training and one decade for verification. The EOFs are derived for the training period, then the forward selection of predictors for the logistic model is performed. Finally, scoring rules were calculated for the verification period. It is crucial that the EOFs are derived on the training period only, otherwise, if the EOFs would be derived on the full period before splitting training and verification data, the predictor time series would already *know* something about the verification data (Hastie et al., 2008, chap. 7.10.2). The complete method applied in the study is presented in detail in the method section of Appendix C.

The statistical models fed with predictors derived from relative vorticity at 850 hPa and vertical velocity at 500 hPa showed the highest skills (cf. figure 3, Appendix C). The investigation of the selected predictors revealed that for nearly all stations the first and the third EOF mode were selected (cf Table 1, Appendix C). Similar dominance has the second mode of the rotated EOFs. Though EOFs or rotated EOFs does not necessarily lead to physically meaningful patterns (Dommenget and Latif, 2002), in the present study the mentioned modes could be related to typical EASM dynamics. So-called Southwest vortices acting on the meso-α-scale disturb the quasi-stationary front between the warm and humid air in the South and the cold and dry air in the North (Ding and Chan, 2005; Wang, 2006).

Supplementary to the results and discussions presented in Appendix C, an example of the development of a Southwest vortex reveals the interaction of relative vorticity and vertical velocity during such a feature (figure 4.5). The same spatial structure was extracted by EOFs and rotated EOFs, and is shown in figures 6,7 and 10 of Appendix C. Especially, the pattern of the second rotated EOF mode (figure 10, Appendix C) highlights this similarity. Rising air over the Yangtze valley comes along with positive vorticity (cyclonic vortex structure). Even a counter-pole of negative vorticity located northwest to the positive vorticity band is visible.

This example makes clear, how physically meaningful predictors can be generated. This additional information can be used for further interpretation of the results of the statistical downscaling scheme. For instance, the probability of the occurrence of rain, or heavy rain, can be interpreted in association with the occurrence of Southwest vortices (Simon et al., 2013a).

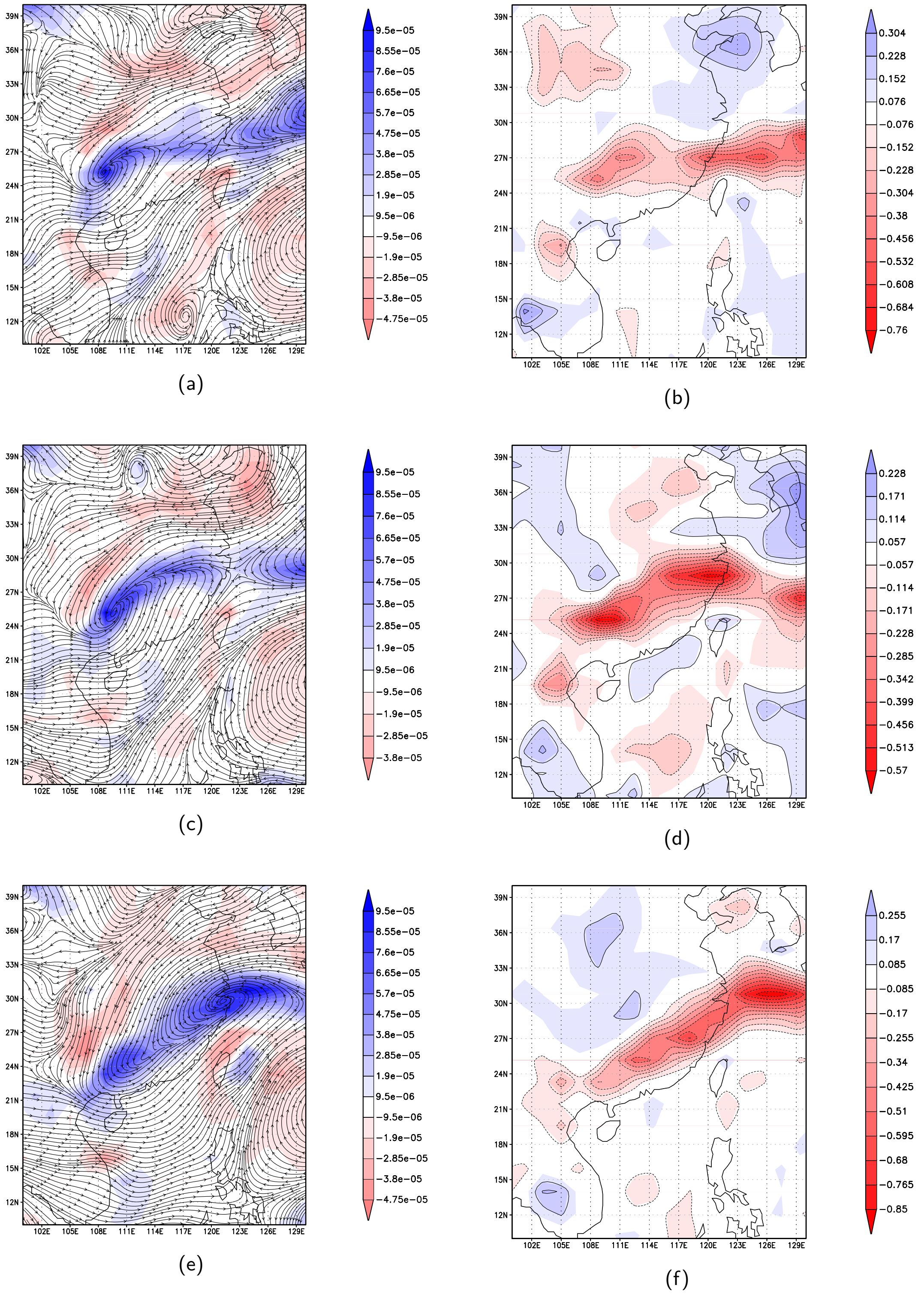

Figure 4.5: The left panels (a,c,e) show relative vorticity (s^{-1}) (red-blue shading) and streamlines of the winds at 850 hPa on three consecutive days in June. The lower panels (b,d,f) show vertical velocity at 500 hPa in pressure coordinates ($Pa\ s^{-1}$) for the same days.

Chapter 5

Conclusions

The field of downscaling climate data can be seen as an interface at which information is transfered between the discipline of climate modeling and other disciplines, e.g., biology, hydrology, impact of climate change, and adaptation to climate change. The key point of this manuscript is to identify and to suggest solutions for critical parts in this transfer process. The broad field of downscaling can be separated into two sub-fields, dynamical downscaling and statistical downscaling. For each of these sub-fields example studies are presented that illustrates how meteorologists can contribute to the information transfer in order to avoid mis-leading interpretation of the downscaled climate data by scientists not familiar to the inherent limitations of the specific downscaling procedure.

Dynamical downscaling is based on physical circulation model that have to be adapted for each experiment, and the computationally expensive experiments have to be performed on super-computers. Thus, we explained the factors, i.e., RCM selection, LBC selection, numerical settings, and tuning of physical parameterizations, crucial for the development of RCM simulations in detail. This RCM design phase, and first evaluation of atmospheric dynamics is demonstrated along the setup of COSMO-CLM for the East Asia domain (cf. section 3.1).

A RCM simulation must not be seen as a completed dataset. Analog to metadata of observations, information of quality and limitations of the RCM output are required to ensure proper application of the data in further studies. An evaluation of the RCM performance, or an assessment of the added value of the RCM simulation has to be enclosed to the RCM output as metadata. Therefore, we presented a newly developed method to quantify temporal scales on which the RCM shows the ability to generate internal variability independent from the model providing LBC (cf. section 3.2). Our method is a contribution to the toolbox containing methods for assessing added value of RCM simulations. Future work on this topic can be split into two branches. The first branch is related to documentation of the available methods for assessing added value. This should be put into practice by designing a comprehensive software package. The second branch is about further developments, and further applications of our method. In this light, we suggest three key points:

- Probably the best way to learn more about the potential of the method is the application to an ensemble of RCM simulations (Mearns et al., 2012; Jacob et al., 2013). This would allow to estimate the sensitivity of coherence structure on changes of numerics, physics, RCM, and LBC.

- The application of coherence spectra is not restricted to the comparison of time series, but it is also possible to compare spatial fields by this method. This can also be seen as an extension of the method proposed by Errico (1985) by cross spectra. This would allow to quantify the effective spatial scales on which an added value is generated by RCMs.
- An interesting study would be the computation of coherence spectra first between a regional re-analysis (Mesinger et al., 2006; Bollmeyer et al., 2014) and the LBC providing global re-analysis, and second between the corresponding dynamical downscaling of the global re-analysis and the global re-analysis, and third between the dynamical downscaling and the regional re-analysis. Hereby, both coherence spectra of time series, and coherence spectra of spatial fields would provide insights of the differences between regional re-analysis, where data-assimilation methods have been employed, and simple dynamical downscaling of global re-analysis.

Beyond the explicit assessment of added value of a single RCM, or an ensemble of RCMs, it is worth evaluating the RCM approach per se.

After 20 years of testing RCMs, serious approaches of bundling computational resources for the generation of RCM ensembles came up during the last five years. Within the CORDEX framework 13 domains cover the world's landmass (Giorgi et al., 2009). For instance, the EURO-CORDEX ensemble contains by now 40 members[1] performed by 29 working groups generated out of 10 different RCMs and 12 different LBC providing GCMs (Jacob et al., 2013). This enormous organizational, computational, and data storage effort, i.e., performing coarse resolution GCM ensembles for LBC plus 13 RCM ensembles of approximately the same order as the EURO-CORDEX or the NARRCAP ensemble, has to be evaluated against the effort necessary for generating a global ensemble with comparable horizontal resolution. Latter approach would also have a conceptual advantage over the RCM approach. Global modeling includes climate feedbacks taking place on continental and ocean basin wide scales, e.g., precipitation over land surrounding the Pacific might have an influence on ENSO, which is suppressed in RCMs. However, common sense within the regional climate modeling community is that there will always be certain issues for what RCMs have to be run.

Furthermore, RCMs have to find their standing in the emerging discipline of decadal climate prediction. Modeling decadal climate is no longer a sole boundary value problem, but a hybrid problem (Taylor et al., 2012). For decadal climate prediction it is not only important how the boundary values of the climate system develop, but it also depends on the initial state of the ocean, or rather the initial state of the whole hydrosphere, which also includes soil moisture and sea ice. It is not clear how RCMs fit in the framework of decadal climate prediction, for which simulations are performed on global scale with coupled AOGCMs. In contrast, most RCMs do not include an ocean component in their modeling system. At least land models are more and more integrated into regional model systems (Shrestha et al., 2014).

[1] Additional 26 simulations are in process.

In **statistical downscaling** statistical transfer functions are employed in order to link information on the large scale to information on the local scale. There is a large variety of statistical methods on hand for this kind of purpose. The toolbox contains methods to downscale continuous variables, probabilities, of probability density functions. Latter group includes distributions for extreme values. Furthermore, multi-variate methods are on hand to account for cross-variabilities between different variables, or different sites (spatial modeling). After all, there are some gaps in the toolbox related to spatial modeling of precipitation, which has a special marginal distribution with a point mass at zero, and extremes, for which multi-variate theory is solved only for two, or three dimensions.

A worthwhile contribution of a meteorologist to this procedure is the derivation of skillful, and physically interpretable predictors. The derivation of such predictors, and their application is presented in an downscaling study. Verification ensures the skillfulness of the predictors, while their physical interpretation is further discussed along examples (cf. section 4.2). The derivation of physically motivated predictors can not be performed automatically by some algorithm, but it always case dependent. Thus, it is important that the statistical downscaling is accompanied by a specialist of the regional atmospheric physics.

A proper observational database is a key requirement for designing a proper statistical downscaling scheme. Nevertheless, in *real world problems* the observational database is often weak: First, the observed time series can be too short to cover a sufficient amount of natural climate. Second, the spatial density of stations is too low to apply spatial statistics within the downscaling scheme. Third, the metadata of the observations is lacking accuracy, e.g., quality assurance, like gap filling or data homogenization techniques are not well documented leading to loss of degree of freedom and/or variability of the provided data.

Summarizing, it is obvious that both fields, dynamical downscaling and statistical downscaling, are not only at a different developmental stage currently, but also differ from each other conceptually. On the one hand, statistical downscaling is easy to implement given a solid observational database, and skillful and meaningful predictors have to be derived from case-to-case. On the other hand, research and development within the field of dynamical downscaling cost a lot of time, effort and computational resources. By nature, such a colossus moves slowly. In the end, a finalized RCM ensemble covers a variety of possible applications, and is as universal as the present GCM ensemble, e.g., CMIP5.

Bibliography

T. Barnett, L. Dümenil, U. Schlese, E. Roeckner, and M. Latif. The effect of eurasian snow cover on regional and global climate variations. *J. Atmos. Sci.*, 46(5):661–686, 1989.

J. Bjerknes. Atmospheric teleconnections from the equatorial pacific. *Mon. Weather Rev.*, 97(3): 163–172, 1969.

C. Bollmeyer, J. D. Keller, C. Ohlwein, S. Bentzien, S. Crewell, P. Friederichs, A. Hense, J. Keune, S. Kneifel, I. Pscheidt, S. Redl, and S. Steinke. Towards a high-resolution regional reanalysis for the european cordex domain. *Quarterly Journal of the Royal Meteorological Society*, 2014. (submitted).

C. Bretherton, M. Widmann, V. Dymnikov, J. Wallace, and I. Bladé. The effective number of spatial degrees of freedom of a time-varying field. *J. Climate*, 12(7):1990–2009, 1999.

G. Brier. Verification of forecasts expressed in terms of probability. *Mon. Weather Rev.*, 78(1):1–3, 1950.

C. Chang, Y. Zhang, and T. Li. Interannual and interdecadal variations of the east asian summer monsoon and tropical pacific ssts. part i: Roles of the subtropical ridge. *J. Climate*, 13(24): 4310–4325, 2000.

S. Coles. *An Introduction to Statistical Modeling of Extreme Values*, volume 208. Springer, London, Berlin, Heidelberg, 2001.

D. Cooley, D. Nychka, and P. Naveau. Bayesian spatial modeling of extreme precipitation return levels. *J. Am. Stat. Assoc.*, 102(479):824–840, 2007.

B. Denis, R. Laprise, D. Caya, and J. Cote. Downscaling ability of one-way nested regional climate models: the big-brother experiment. *Clim. Dynam.*, 18(8):627–646, 2002.

A. Di Luca, R. de Elía, and R. Laprise. Potential for added value in precipitation simulated by high-resolution nested regional climate models and observations. *Clim. Dynam.*, 38(5):1229–1247, 2012.

Y. Ding and J. Chan. The east asian summer monsoon: an overview. *Meteorol. Atmos. Phys.*, 89 (1):117–142, 2005.

D. Dommenget and J. Flöter. Conceptual understanding of climate change with a globally resolved energy balance model. *Clim. Dynam.*, 37(11-12):2143–2165, 2011.

D. Dommenget and M. Latif. A cautionary note on the interpretation of EOFs. *J. Climate*, 15(2): 216–225, 2002.

B. Efron and R. Tibshirani. *An introduction to the bootstrap*, volume 57. Chapman & Hall/CRC, London, 1993.

R. M. Errico. Spectra computed from a limited area grid. *Mon. Weather Rev.*, 113(9):1554–1562, 1985.

F. Feser. Enhanced detectability of added value in limited-area model results separated into different spatial scales. *Mon. Weather Rev.*, 134(8):2180–2190, 2006.

F. Feser, B. Rockel, H. von Storch, J. Winterfeldt, and M. Zahn. Regional climate models add value to global model data. *B. Am. Meteorol. Soc.*, 92:1181–1192, 2011.

R. A. Fisher and L. H. C. Tippett. Limiting forms of the frequency distribution of the largest or smallest member of a sample. In *Mathematical Proceedings of the Cambridge Philosophical Society*, volume 24, pages 180–190. Cambridge Univ Press, 1928.

K. Fraedrich, E. Kirk, and F. Lunkeit. Portable university model of the atmosphere. *DKRZ Rep*, 16, 1998.

F. Giorgi, J. Christensen, M. Hulme, H. Von Storch, P. Whetton, R. Jones, L. Mearns, C. Fu, R. Arritt, B. Bates, et al. Regional climate information-evaluation and projections. *Climate Change 2001: The Scientific Basis. [Houghton, JT et al.] Cambridge University Press, Cambridge*, pages 583–638, 2001.

F. Giorgi, C. Jones, G. R. Asrar, et al. Addressing climate information needs at the regional level: the CORDEX framework. *WMO Bulletin*, 58(3):175, 2009.

T. Gneiting and A. Raftery. Strictly proper scoring rules, prediction, and estimation. *J. Am. Stat. Assoc.*, 102(477):359–378, 2007.

T. Gneiting, F. Balabdaoui, and A. Raftery. Probabilistic forecasts, calibration and sharpness. *J. Roy. Stat. Soc. B.*, 69(2):243–268, 2007.

I. Harris, P. Jones, T. Osborn, and D. Lister. Updated high-resolution grids of monthly climatic observations–the cru ts3. 10 dataset. *Int. J. Climatol.*, 2013.

K. Hasselmann. Stochastic climate models part I. theory. *Tellus*, 28(6):473–485, 1976.

T. Hastie, R. Tibshirani, and J. Friedman. *The elements of statistical learning*. Springer Series in Statistics, London, Berlin, Heidelberg, 2nd edition, 2008.

G. Hegerl, O. Hoegh-Guldberg, G. Casassa, M. Hoerling, R. Kovats, C. Parmesan, D. Pierce, and P. Stott. Good practice guidance paper on detection and attribution related to anthropogenic climate change. In *Meeting Report of the Intergovernmental Panel on Climate Change Expert Meeting on Detection and Attribution of Anthropogenic Climate Change*, pages 1–8. Citeseer, 2010.

M. P. Hoerling, A. Kumar, and M. Zhong. El Niño, La Niña, and the nonlinearity of their teleconnections. *J. Climate*, 10(8):1769–1786, 1997.

D. Jacob, A. Elizalde, A. Haensler, S. Hagemann, P. Kumar, R. Podzun, D. Rechid, A. R. Remedio, F. Saeed, K. Sieck, et al. Assessing the transferability of the regional climate model remo to different COordinated Regional climate Downscaling EXperiment (CORDEX) regions. *Atmosphere*, 3(1):181–199, 2012.

D. Jacob, J. Petersen, B. Eggert, A. Alias, O. B. Christensen, L. M. Bouwer, A. Braun, A. Colette, M. Déqué, G. Georgievski, et al. EURO-CORDEX: new high-resolution climate change projections for European impact research. *Reg. Environ. Change*, pages 1–16, 2013.

I. Jolliffe. *Principal component analysis*. Springer Series in Statistics. Springer, New York, 3rd edition, 2002.

H. F. Kaiser. The varimax criterion for analytic rotation in factor analysis. *Psychometrika*, 23(3): 187–200, 1958.

V. Kuell, A. Gassmann, and A. Bott. Towards a new hybrid cumulus parametrization scheme for use in non-hydrostatic weather prediction models. *Q. J. Roy. Meteor. Soc.*, 133(623):479–490, 2007.

R. Laprise, D. Kornic, M. Rapaić, L. Šeparović, M. Leduc, O. Nikiema, A. Luca, E. Diaconescu, A. Alexandru, P. Lucas-Picher, et al. Considerations of domain size and large-scale driving for nested regional climate models: Impact on internal variability and ability at developing small-scale details. *Climate Change [A. Berger el al.]*, pages 181–199, 2012.

J. Li, Z. Wu, Z. Jiang, and J. He. Can global warming strengthen the east asian summer monsoon? *J. Climate*, 23(24), 2010.

E. Lorenz. Empirical orthogonal functions and statistical weather prediction. Massachusetts Institute of Technology, Dept. of Meteorology, 1956.

E. N. Lorenz. Deterministic nonperiodic flow. *J. Atmos. Sci.*, 20(2):130–141, 1963.

P. Lynch. The origins of computer weather prediction and climate modeling. *J. Comput. Phys.*, 227 (7):3431–3444, 2008.

E. S. Martins and J. R. Stedinger. Generalized maximum-likelihood generalized extreme-value quantile estimators for hydrologic data. *Water Resour. Res.*, 36(3):737–744, 2000.

P. McCullagh and J. Nelder. *Generalized linear models*. Chapman & Hall/CRC, 1989.

L. O. Mearns, R. Arritt, S. Biner, M. S. Bukovsky, S. McGinnis, S. Sain, D. Caya, J. Correia Jr, D. Flory, W. Gutowski, et al. The north american regional climate change assessment program: Overview of phase i results. *B. Am. Meteorol. Soc.*, 93(9):1337–1362, 2012.

G. A. Meehl, C. Covey, K. E. Taylor, T. Delworth, R. J. Stouffer, M. Latif, B. McAvaney, and J. F. Mitchell. The WCRP CMIP3 multimodel dataset: A new era in climate change research. *B. Am. Meteorol. Soc.*, 88(9):1383–1394, 2007.

F. Mesinger, G. DiMego, E. Kalnay, K. Mitchell, P. C. Shafran, W. Ebisuzaki, D. Jovic, J. Woollen, E. Rogers, E. H. Berbery, et al. North American regional reanalysis. *B. Am. Meteorol. Soc.*, 87 (3):343–360, 2006.

S.-K. Min and A. Hense. A Bayesian assessment of climate change using multimodel ensembles. part I: Global mean surface temperature. *J. Climate*, 19(13), 2006.

A. H. Murphy. General decompositions of MSE-based skill scores: Measures of some basic aspects of forecast quality. *Mon. Weather Rev.*, 124(10):2353–2369, 1996.

A. H. Murphy and R. L. Winkler. Diagnostic verification of probability forecasts. *International Journal of Forecasting*, 7(4):435–455, 1992.

N. Nakicenovic, J. Alcamo, G. Davis, B. de Vries, J. Fenhann, S. Gaffin, K. Gregory, A. Grubler, T. Y. Jung, T. Kram, et al. Special report on emissions scenarios: A special report of working group III of the Intergovernmental Panel on Climate Change. Technical report, Pacific Northwest National Laboratory, Richland, WA (US), Environmental Molecular Sciences Laboratory (US), 2000.

R. A. Pielke Sr. *Mesoscale meteorological modeling*, volume 98. Academic press, Orlando, 2013.

Y. Qian, Y. Zheng, Y. Zhang, and M. Miao. Responses of China's summer monsoon climate to snow anomaly over the Tibetan Plateau. *Int. J. Climatol.*, 23(6):593–613, 2003.

B. Rockel, A. Will, and A. Hense. The regional climate model COSMO-CLM (CCLM). *Meteorol. Z.*, 17(4):347–348, 2008.

E. Roeckner, G. Bäuml, L. Bonventura, R. Brokopf, M. Esch, M. Giorgetta, S. Hagemann, I. Kirchner, L. Kornblueh, E. Manzini, et al. The atmospheric general circulation model ECHAM5. PART I: Model description, Report 349, Max Planck Institute for Meteorology, Hamburg, Germany, 2003.

M. Rummukainen. State-of-the-art with regional climate models. *Wiley Interdisciplinary Reviews: Climate Change*, 1(1):82–96, 2010.

R. Saravanan and J. C. McWilliams. Advective ocean–atmosphere interaction: An analytical stochastic model with implications for decadal variability. *J. Climate*, 11(2), 1998.

T. Sato and Y. Xue. Validating a regional climate model's downscaling ability for east asian summer monsoonal interannual variability. *Clim. Dynam.*, 41(9-10):2411–2426, 2013.

C. Schölzel and A. Hense. Probabilistic assessment of regional climate change in southwest germany by ensemble dressing. *Clim. Dynam.*, 36(9):2003–2014, 2011.

W. Shamarock, J. Klemp, J. Dudhia, D. Gill, D. Barker, M. Duda, X. Huang, W. Wang, and J. Powers. A description of the advanced research WRF version 3. *NCAR technical note NCAR/TN/u2013475*, 2008.

P. Shrestha, M. Sulis, M. Masbou, S. Kollet, and C. Simmer. A scale-consistent terrestrial systems modeling platform based on COSMO, CLM and ParFlow. *Mon. Weather Rev.*, 2014. http://dx.doi.org/10.1175/MWR-D-14-00029.1.

T. Simon, A. Hense, B. Su, T. Jiang, C. Simmer, and C. Ohlwein. Pattern-based statistical downscaling of East Asian summer monsoon precipitation. *Tellus A*, 65(19749), 2013a. http://dx.doi.org/10.3402/tellusa.v65i0.19749.

T. Simon, D. Wang, A. Hense, C. Simmer, and C. Ohlwein. Generation and transfer of internal variability in a regional climate model. *Tellus A*, 65(22485), 2013b. http://dx.doi.org/10.3402/tellusa.v65i0.22485.

K. E. Taylor, R. J. Stouffer, and G. A. Meehl. An overview of CMIP5 and the experiment design. *B. Am. Meteorol. Soc.*, 93(4):485–498, 2012.

C. Tebaldi and R. Knutti. The use of the multi-model ensemble in probabilistic climate projections. *Philos. T. Roy. Soc. A*, 365(1857):2053–2075, 2007.

M. Tiedtke. A comprehensive mass flux scheme for cumulus parameterization in large-scale models. *Mon. Weather Rev.*, 117(8):1779–1800, 1989.

S. Uppala, P. Kållberg, A. Simmons, U. Andrae, V. Bechtold, M. Fiorino, J. Gibson, J. Haseler, A. Hernandez, G. Kelly, et al. The ERA-40 re-analysis. *Q. J. Roy. Meteor. Soc.*, 131(612): 2961–3012, 2005.

H. von Storch and F. Zwiers. *Statistical analysis in climate research*. Cambridge Univ Pr, Cambridge, UK, 2002.

H. Wackernagel. *Multivariate geostatistics*. Springer, Berlin Heidelberg New York, 2010.

B. Wang. *The Asian Monsoon*. Springer Verlag, Berlin, 2006.

B. Wang and Z. Fan. Choice of South Asian summer monsoon indices. *B. Am. Meteorol. Soc.*, 80: 629–638, 1999.

B. Wang, R. Wu, and X. Fu. Pacific-East Asian teleconnection: How does ENSO affect East Asian climate? *J. Climate*, 13(9):1517–1536, 2000.

D. Wang, C. Menz, T. Simon, C. Simmer, and C. Ohlwein. Regional dynamical downscaling with CCLM over East Asia. *Meteorol. Atmos. Phys.*, 121:39–53, 2013.

H. Wang. The instability of the East Asian summer monsoon–ENSO relations. *Adv. Atmos. Sci.*, 19(1):1–11, 2002.

Y. Wang and L. Zhou. Observed trends in extreme precipitation events in China during 1961–2001 and the associated changes in large-scale circulation. *Geophys. Res. Lett.*, 32(9), 2005.

D. Wilks. *Statistical methods in the atmospheric sciences*, volume 100. Academic press, Oxford, 2011.

J. Winterfeldt and R. Weisse. Assessment of value added for surface marine wind speed obtained from two regional climate models. *Mon. Weather Rev.*, 137(9):2955–2965, 2009.

T.-W. Wu and Z.-A. Qian. The relation between the Tibetan winter snow and the Asian summer monsoon and rainfall: An observational investigation. *J. Climate*, 16(12):2038–2051, 2003.

P. Xie, A. Yatagai, M. Chen, T. Hayasaka, Y. Fukushima, C. Liu, and S. Yang. A gauge-based analysis of daily precipitation over East Asia. *J. Hydrometeorol.*, 8(3), 2007.

P. Zhai, X. Zhang, H. Wan, and X. Pan. Trends in total precipitation and frequency of daily precipitation extremes over China. *J. Climate*, 18(7):1096–1108, 2005.

Y. Zhang, K. R. Sperber, and J. S. Boyle. Climatology and interannual variation of the East Asian winter monsoon: Results from the 1979–95 NCEP/NCAR re-analysis. *Mon. Weather Rev.*, 125 (10), 1997.

List of abbreviations

Abbreviation	Description
AGCM	atmospheric general circulation model
AOGCM	coupled atmosphere-ocean general circulation model
BMWF	Bundesministerium für Wissenschaft und Forschung
cdf	cumulative distribution function
CMIP	coupled model intercomparison project
CORDEX	coordinated regional climate downscaling experiment
COSMO-CLM	consortium for small-scale modeling - climate limited-area modeling
CRF	calibration refinement factorization
DFG	deutsche Forschungsgemeinschaft
DKRZ	deutsches Klimarechenzentrum
EASM	East Asian summer monsoon
EAWM	East Asian winter monsoon
ECHAM	ECMWF-Hamburg GCM
ECMWF	European centre for medium-range weather forecasts
ENSO	El-Niño Southern oscillation
EOF	empirical orthogonal function
ERA-40	ECMWF 40 year re-analysis
EVT	extreme value theory
GCM	general circulation model
GEV	generalized extreme value distribution
GLM	generalized linear model
ISM	Indian summer monsoon
ITCZ	inter-tropical convergence zone
LBC	lateral boundary conditions
MLE	maximum likelihood estimation
NARCCAP	North American regional climate change assessment program
NSFC	national natural science foundation of China
NWP	numerical weather prediction
PCA	principal component analysis
pdf	probability density function

PIK	Potsdam Institut für Klimafolgenforschung
RCM	regional climate model
REMO	regional model
SCS	Southern Chinese Sea
SMH	Siberian-Mongolian high
SST	sea surface temperature
WCRP	world climate research programme
WNPH	Western North Pacific high
WRF	weather research and forecasting model

List of Figures

Appendix A

Regional dynamical downscaling with CCLM over East Asia

The following manuscript is the accepted author's version. It has been published in the peer-reviewed journal *Meteorology and Atmospheric Physics* in 2013. The final publication is available at Springer via http://dx.doi.org/10.1007/s00703-013-0250-z.

Attribution of roles

Dinan Wang, Christian Ohlwein, Clemens Simmer designed experiments in coordination with Christoph Menz. Dinan Wang performed RCM experiments (ERA-40 driven and ECHAM run no.1 driven). Christoph Menz performed RCM experiments (ECHAM run no.3 driven). Dinan Wang performed analysis of mean temperature and precipitation fields. Thorsten Simon performed analysis of resolved monsoon dynamics. Dinan Wang and Thorsten Simon wrote major parts of the paper. All authors discussed the results and commented on the manuscript.

Noname manuscript No.
(will be inserted by the editor)

Regional dynamical downscaling with CCLM over East Asia

Dinan Wang · Christoph Menz · Thorsten Simon ·

Clemens Simmer · Christian Ohlwein

Received: date / Accepted: date

ABSTRACT

Inspired by the framework of the Coordinated Regional Climate Downscaling Experiment (CORDEX), the hindcast (1971-2000) and projection (2021-2050) simulations based on a resolution of 0.44° over the East Asia domain are performed with the regional climate model COSMO-CLM (CCLM). The simulations are driven by ERA-40 reanalysis data and output of the global climate model ECHAM5. This is the first time that the CCLM is adapted and evaluated for the East Asia Monsoon region; the setup is considered a starting point for further improvements in this region by the CCLM community. The evaluation results show that

Dinan Wang

Meteorological Institute, University of Bonn

Auf dem Hügel 20, 53121 Bonn.

E-mail: dinanbonn@yahool.de

Present address: Institute of Energy Systems and Energy Business, University of Applied Science Ruhr-West

Christoph Menz

Potsdam Institute for Climate Impact Research

E-mail: menz@pik-postdam.de

Thorsten Simon

Meteorological Institute, University of Bonn

Clemens Simmer

Meteorological Institute, University of Bonn

Christian Ohlwein

Meteorological Institute, University of Bonn

the CCLM is able to reasonably capture the climate features in this region, especially the monsoon dynamics on small scales. However, total precipitation in the northern part of the domain, over the Tibetan Plateau, and over east Indonesia has a pronounced wet bias. The projected climate change under the A1B scenario indicates an overall annual surface temperature increase of 1 K to 2 K, but no significant precipitation changes.

Keywords Regional climate modelling · COSMO-CLM · CORDEX East Asia

1. Introduction

The first successful application of regional climate models (RCM) dates back almost two decades (Giorgi and Bates 1989). Particularly in the last decade, considerable community efforts have been invested into improvement of model physics and dynamics for meso-scale processes and into the investigation of internal model variability and model limitations, while the range of RCM application has steadily increased (Rummukainen 2010). Despite these efforts and the potential of RCMs to reveal climate changes on the scales required for impact studies the merits of dynamical downscaling (downscaling of global climate simulations with RCMs) is often debated. Concerns can mostly be related to the isolated regional climate downscaling studies over specific interested areas and the lack of ensemble projections of sufficient quality (Giorgi et al 2009). Intrigued by these debates, WCRP (World Climate Research Program) recently initiated the Coordinated Regional Climate Downscaling Experiment (CORDEX)[1], which will provide a comprehensive picture of regional climate change projections based on ensembles of dynamical downscaling experiments.

In our regional climate downscaling studies over East Asia we largely follow the rules recommended by CORDEX. The study region covers the area of interest of the two research programmes co-funded by the German Research Foundations and the National Natural Science Foundation of China (DFG/NSFC, "Land Use and Water Resources Management under Changing Environmental Conditions", 2010-2012) and by the German Federal Ministry for Research and Education (BMBF, "Sustainable water and agricultural land use in the Guanting watershed under limited water resources", 2009-2012). The aim of the DFG/NSFC

[1] http://wcrp.ipsl.jussieu.fr/SF_RCD_CORDEX.html

project hosted by the University of Bonn is the combination of dynamical and statistical downscaling of global climate runs for a better understanding of potential future extreme events in the Haihe and Poyang Lake watersheds in China. The BMBF project, hosted by Potsdam Institute for Climate Impact Research, also employs a similar approach to the Guanting watershed. The downscaling results will be used to force hydrological models employed within the two research programmes. Since the simulation domains of both programmes are located within the East Asia domain defined by CORDEX, we performed a series of regional dynamical downscaling runs over this area. Although inspired by CORDEX our simulation setups are not identical to the prescriptions by CORDEX (e.g. the domain size and the driving data) due to the priorities of both programmes.

The Asian Summer Monsoon (ASM) is probably the most pronounced regional climate system in the region. The dynamics of ASM influences droughts and floods over Asia and impacts the global circulation (Ji and Vernekar 1997), thus its representation in simulations is of particular concern. Multiple general circulation model (GCM) ensemble simulations are usually employed to quantify the uncertainty range of climate projections (Min et al 2004; Kitoh and Uchiyama 2006). Due to low spatial resolutions and the required parameterizations, GCMs have difficulties to describe regional precipitation patterns generated by the ASM regions (Kawase et al 2008; Gao et al 2006). These problems are likely caused at least in part by heavy rainfall associated with the steep orography (IPCC 2007). The higher spatial resolution of RCMs is expected to remedy some of these shortcomings (Fu et al 2005; Kumar et al 2006). For example, Gao et al (2006) found that even the simulated large scale precipitation patterns are heavily influenced by resolution during the mid- to late-monsoon months, when small scale convective processes dominate precipitation generation. Mesoscale processes in the RCMs are indeed in some cases beneficial for rendering a more clear picture of ASM features (Yhang and Hong 2008).

The regional climate model COSMO-CLM (CCLM: COSMO - the COnsortium for Small-scale Modelling, CLM - Climate Limited-area Modelling or climate version of “Lokalmodell”) has been adopted for regional climate change projections in our study by employing the so-called time-slice mode. The CCLM has been already examined for its inter-continent transferability using the standard parameter setup for Europe, in which particularly the tropical ASM region was investigated within a short period (2001-2004) (Rockel and

Geyer 2008). Dobler and Ahrens (2008) showed the CCLM capabilities for Indian Summer Monsoon studies. The CCLM has, however, not been configured for East Asia for the investigation of future climate change, which is the central topic of this paper.

In section 2, the simulation design including study region, model configuration and reference data is described. Section 3 presents the results from five experiments. The analysis focuses on the $2m$ (screen level) temperature and precipitation. In a sub-section also the capability of the CCLM to model the important East Asia monsoon dynamics on small scales is demonstrated by examples. Section 4 finally provides a short summary and some conclusions from our study.

2. Simulation Design

a. Study Region

The CORDEX East Asia domain has a spatial extension of roughly $10500 \times 8000\ km^2$. Besides China, Mongolia and most parts of India it covers Indochina and the islands of Indonesia, the Philippines, and Japan. Almost one third of the world's population inhabits this region. The region is characterized by a large land-sea-contrast stimulating the Monsoon circulation and steep orography modulating the regional circulation and its effects on precipitation patterns. Figure 1 shows the simulation domain of the CCLM (red dotted line). For boundary relaxation and mitigation of gravity wave reflection the lateral relaxation zone is set to 16 grid boxes ($\approx 800\ km$) leaving an area of $9500 \times 7000\ km^2$ (purple line), which we term "CORDEX East Asia (CORDEX-easia)" for evaluation. The continental area is divided into 17 sub-domains, which were chosen according to Köppen-Geiger classification and observed mean temperature and precipitation.

b. Model Configuration

The CCLM is a non-hydrostatic regional climate model for meso-β to meso-γ scale resolutions (1-50 km). The model is based on the primitive thermo-hydrodynamic equations, which are formulated on a rotated horizontal grid (ARAKAWA-C-lattice type (Arakawa and Lamb 1981)) and a terrain following height coordinate [2]. Table 1 shows the grid definitions for our simulations. Various parameters were tested by two short-term simulations (1959-1964, 1996-1998) excluding the first year, respectively, for spin-up. Both test simulations were driven by ERA-40 reanalysis data in order to minimise systematic biases introduced from driving models. The period 1996-1998 includes two extreme events, i.e. the drought in the North China Plain in 1997 and the flooding in south China in 1998. The tests, based on the standard setup of CCLM for Europe, focused on the selection of the most appropriate integration scheme and the configuration of the lateral and upper boundary relaxation zones. The limited computational resources restricted the test simulations to rather short periods; also potential interdependencies of tested parameters could not be evaluated in detail. Benchmark variables were 2 m temperature and precipitation.

The Leapfrog temporal integration scheme is chosen over the Runge-Kutta scheme, because of both better computational performance and representation of spatial patterns of temperature and precipitation in particular over China. Different integration time-steps (from 75 s to 150 s) were tested; improvements when using smaller time-steps than 150 s were insignificant and did not justify the longer computational time. A modified Robert-Asselin time filter (Williams 2009) (named as "alphaass" in the CCLM) is used in conjunction with the Leapfrog scheme to reduce the impacts of the filter on the physical mode while suppressing the spurious computational mode. Our tests indicate that the proper adjustment of this filter (alphaass = 0.7) can lead to a significant improvement, especially for the simulated temperatures in Haihe basin.

Steep orography is evident within the CORDEX-easia domain and at the lateral boundaries. Moreover, the simulation domain incorporates a wide range of climatic zones. Thus it is essential to investigate model sensitivity to specifications of the lateral and upper boundary relaxation zones. The tests on the width of the lateral relaxation layer (named as "rlwidth" in the CCLM) reveal that the high mountains within or close to the lateral relaxation zone result in a significant overestimation of precipitation. The interpolated fields of the driving model seem to produce additional orographic precipitation. We selected an 800 km wide lateral relaxation layer containing the Karakorum. This configuration produces better precipitation patterns within the central area of the model domain and our study regions, despite considerable overestimations of

[2] http://www.cosmo-model.org

precipitation in a small area near the Karakorum. As the model domain includes tropical and sub-tropical climatic zones as well as the mountainous regions, the Rayleigh sponge damping layer on the top of the model domain needs to be adjusted. The bottom height (named as "rdheight" in the CCLM) of the layer is extended from the standard setup of 11 km to 13 km, which improves particularly monthly precipitation in south China and north east China. The most important CCLM (COSMO_4.8_CLM11) parameters found for this study are listed in Table 2.

c. Reference Data

As reference datasets for temperature and precipitation we use the CRU-TS3.0 (Climate Research Unit)[3] (Jones and Harris 2008) and APHRODITE-APHRO_V1003R1 datasets (Asian Precipitation Highly Resolved Observational Data Integration towards Evaluation of the Water Resources) [4] (Xie et al 2007). CRU-TS3.0 defined on a $0.5° \times 0.5°$ grid contains global monthly 2m temperature, while APHRODITE contains daily precipitation over Asia on a 0.25° grid or 0.5° (the latter is used in this paper). APHRO_V1003R1 is based on the network of daily rain gauge data for Asia, which contains up to 4.5 times more observations than available through the Global Telecommunication System network, and thus should better characterize precipitation characteristics in mountainous areas, such as the Himalayas (Yatagai et al 2009). For evaluation the CCLM output is mapped to the CRU-TS3.0 grid (0.5°) via a bilinear interpolation.

3. Simulation Results and Analysis

Three hindcast simulations for model evaluation and simulation design are performed, driven by ERA-40 reanalysis data (Uppala et al 2005) and ECHAM5-20C-(R1, all-R3) (Roeckner et al 2006a; Roeckner 2005) in a spectral resolution TL159 with 49 atmospheric and 3 soil layers. ECHAM5 GCM outputs on a T63 grid with 31 atmospheric and 4 soil layers are used for both hindcast and future projections. ECHAM5-20C-all-R3 is forced by anthropogenic (green house gases, sulphate) plus natural forcing (variable solar constant and effects

[3] Data are available online http://www.cru.uea.ac.uk/cru/data/hrg/.

[4] Data are available on-line http://www.chikyu.ac.jp/precip/.

of volcanic aerosols are included), while ECHAM-20C-R1 only includes observed anthropogenic forcing. Hence we can examine the impact of natural forcing on the model response. The A1B emission scenario is used in two simulations with the ECHAM5 global climate model (ECHAM5-A1B-(R1,R3) (Roeckner et al 2006b,c), to which we apply dynamical downscaling. Both realizations are initialized with different runs of ECHAM5-20C using anthropogenic forcing. Our CCLM simulations for the period from 1971 to 2000 driven either with ERA-40 or ECHAM5-20C are used for validation. For the future projection run, the period from 2021 to 2050 is chosen because of its relevance for near future climate change impact assessments required by the funding research programmes.

Evaluation focuses on the average annual and seasonal 2 m temperature (Figure 2) and total precipitation fields (Figure 3). Due to the large spatial variability of annual precipitation over the simulation domain we compute the relative bias (the difference relative to the respective reference dataset)(Figure 3). The relative bias is considered significant when the p-value of a t-Test (von Storch and Zwiers 1999) is below 0.1. We also show the annual values averaged over the sub-regions defined in Figure 1.

*a. ERA-*40 *driven simulation*

Our ERA-40 driven simulation with an approximate downscaling factor of 2.5 is first performed as a control run for evaluating model performance. ERA-40 is observation based and thus contains less systematic biases compared to GCM outputs. Thus the capability of CCLM to reproduce the present climate can be evaluated without, or at least with considerably reduced systematic bias in the large-scale forcing. The resolution difference between driving data and the CCLM, can however, lead to additional biases.

The first column of Figure 2 and Figure 3 shows the temperature and precipitation bias of the ERA-40 driven CCLM run compared to CRU and APHRODITE, respectively. The temperature bias ranges in most regions from -5 K to $+5$ K with the exception of the Himalaya and especially the Karakorum where the bias ranges from -10 K to 10 K. Extreme biases (± 10 K) are however only located at a few grid points and might result from an under-representation of the steep orography in the CCLM. The large observation uncertainty in this region can, however, also be a reason for the discrepancies (Brohan et al 2006; Lorenz and Kunstmann 2012). The mountain ridges of the Tibetan Plateau and Indochina exhibit the strongest cold bias while the largest warm bias appears in the Tarim basin and western Mongolia. The cold bias in east Indonesia might be associated with the overestimation of precipitation, especially at the mountain ridges of New Guinea.

Figure 3 shows that the CCLM produces a pronounced relative wet bias in the most northern part of the domain (north of latitude 40°) and over the Tibetan Plateau during their dry period (Oct to April, mainly in DJF and MAM). The high relative wet bias corresponds to a considerable absolute wet bias of up to 200 mm. However, the driving data ERA-40 has an even larger annual relative bias in this region (about 220%) than the CCLM (Table 3), which can partially account for the CCLM's performance in this context. Similar results hold for east Indonesia and the Philippines, although the precipitation amounts in those regions are up to 10 times higher than over the Tibetan Plateau. The absolute wet bias in east Indonesia is about 1500 mm. By contrast, the Philippines and west Indonesia show a surprisingly low bias compared to the spurious ERA-40 data in this region (Trenberth et al 2001).

According to Table 3 CCLM does not significantly improve the area averaged bias for temperature compared to the driving data. This might be partially attributed to the rather small downscaling factor, which leads to similar orographic heights both in the forecast model used for ERA40 and in the CCLM. The overall warm bias of the ERA-40 driven CCLM run is 0.82 K, which is slightly higher than the bias of ERA-40. Concerning precipitation (see table 3) the CCLM seems to be able to partly compensate for the known spurious results of ERA-40 in the tropics (Trenberth et al 2001) despite some significant relative biases in some subdomains. In summary, CCLM in this simulation setup is able to properly downscale the parent global fields and even reduces the error of the driving model ERA-40 within certain regions.

b. ECHAM5-20C driven simulation

As mentioned in Section 3a, there will be a systematic bias compared to observations introduced by the driving GCM output into the CCLM. Further differences might be caused by the higher (compared to the ERA40-driven CCLM runs) downscaling factor of about 4.5 for the GCM driven CCLM runs, which can lead to different synoptic scale behaviour (Rummukainen 2010).

Two ECHAM5-driven CCLM runs are used to assess the influence of natural forcing. However natural forcing affects only the driving GCM since the CCLM is not yet able to dynamically implement variable aerosol loads and a variable solar constant. Thus natural forcing affects CCLM only implicitly via the driving model (mainly temperature).

The second and third column of Figure 2 show that both ECHAM5-20C driven runs basically produce the same bias patterns as the ERA-40 driven run. The differences between ERA-40 and ECHAM5-20C driven runs are small and restricted to south India, Indochina and the north east continental areas (NEC and NE). The ECHAM5-20C driven runs show a cold bias in every season in north-eastern China and other north-eastern subdomains, while in south India the most pronounced cold bias is mainly associated with the rainy season (JJA). Over Indochina the ECHAM5-20C driven runs produce a slight warm bias in the annual mean temperature, in contrast to the cold bias of the ERA-40 driven run. There are no significant temperature pattern differences between ECHAM5-20C-R1 and ECHAM5-20C-all-R3. The biases averaged across the whole simulation domain for both runs differ only by about 0.2 K, which is of the same order of magnitude as the difference between the two driving datasets (shown in Table 4 and Table 5, where a total bias is 0.59 K for the ECHAM5-20C-R1 driven run and 0.41 K for the ECHAM5-20C-all-R3 driven run).

Concerning precipitation both ECHAM5-20C driven runs produce similar bias patterns as the ERA-40 driven run (Figure 3). Due to the seasonal precipitation cycle the strongest absolute biases occur in MAM and JJA. The strong relative wet bias of CCLM from SON to MAM for all three driving datasets implies that the CCLM is not able to reproduce the dry season in the north sufficiently. In east Indonesia the ECHAM5-20C driven runs produce a less pronounced wet bias in every season compared to the ERA-40 run, while in west Indonesia a more significant wet bias appears in the dry season (JJA) especially over the island of Java. Both ECHAM5-20C driven runs show again no significant difference. The overall precipitation biases across the CORDEX East Asia domain for ECHAM5-20C-R1 and ECHAM5-20C-all-R3 are 183 mm and 164 mm, respectively (Table 4 and 5).

Overall there are no significant differences in the temperature and precipitation patterns for all three hindcast runs compared to the reference data. The CCLM produces a small warm bias averaged over the whole CORDEX East Asia domain. The biases of the ECHAM5 driven runs are slightly lower than the

ERA-40 driven run. The strongest biases generally occur at mountain ridges. CCLM simulates an average wet bias across the whole domain mainly due to an overestimation in the northern part of the simulation domain and over east Indonesia. The overestimation is more pronounced when driven by ECHAM5-20C. The hindcast driving data ECHAM5-20C-R1 and ECHAM5-20C-all-R3 show no significant differences over the whole domain, but ECHAM5-20C-all-R3 (with a natural forcing) leads to a lower bias for both temperature and precipitation compared to ECHAM5-20C-R1 (without a natural forcing) data. The same holds true for the respective CCLM simulations.

c. *ECHAM5-A1B driven simulation*

Two downscaled future projections based on Run-1 and -3 of ECHAM5 under the A1B emission scenario are performed for the period 2021 to 2050. Here the CCLM model results are compared to the respective hindcast simulations driven by ECHAM5-20C-R1 and -all-R3, respectively.

The last two columns of Figure 2 show the projected change of temperature. Both runs produce a similar annual temperature change with a slight south to north gradient of 1 K to 2 K. The ECHAM5-A1B-R1 driven run has the most significant temperature increase over the Tibetan Plateau in DJF and MAM, while the ECHAM5-A1B-R3 driven run shows a stronger temperature increase in north-eastern China throughout the year. Both runs reveal a more than 2 K temperature increase over the Sichuan Basin in JJA and SON. However, the ECHAM5-A1B-R3 driven run presents a more pronounced increase probably due to the effect of the natural forcing in the ECHAM5-20C-all-R3 driven run. The highest temperature increase of up to or above 3 K with the most extended spatial coverage is projected for winter from both runs, which is remarkable considering the time frame of only 30 years. The similar climate change signals were also detected in the previous studies of climate projections over east Asia (Xu et al 2005; Zhang et al 2012; Hulme et al 1994).

Precipitation shows less systematic changes (Figure 3) but large differences between both projections. The relative precipitation anomaly of the ECHAM5-A1B-R1 driven run displays an increase of precipitation in a band around 20°N and 50°N and a decrease elsewhere. The most significant decrease in absolute precipitation is projected for the North China Plain and central and southern China in autumn (SON). In

JJA precipitation is projected to increase by more than 15% in west Indonesia, Indochina and south India. Nevertheless due to the high variability of precipitation these changes are not significant. This also explains the differences to the ECHAM5-A1B-R3 driven run and some findings of the previous studies (Xu et al 2005; Zhang et al 2012; Hulme et al 1994), whose statements are however not based on the t-test used in this paper. The ECHAM5-A1B-R3 driven run suggests that the projected significant temperature increase over the Sichuan Basin is related to a drastic precipitation decrease in the same region. The projections also hint at precipitation decreases of more than 20% over south China in autumn.

The temperature and precipitation change patterns derived from the CCLM results are comparable to the results from ECHAM5-A1B (figure not shown). Additionally CCLM can reasonably simulate climate change signals on smaller scales, e.g. around the Tibetan Plateau for the ECHAM5-A1B-R1 driven run or over Sichuan Basin for the ECHAM5-A1B-R3 driven run.

d. Examples for resolved monsoon dynamics

Dynamical downscaling with RCMs is performed in order to better resolve dynamical processes by using finer spatial and temporal scales. It is expected that the higher resolution leads to a more realistic representation of e.g. convection and its influence on the regional climate than with the low resolution of the driving GCM. A dominant meso-α scale feature of east Asian meteorology is the East Asian Summer Monsoon (EASM), the representation of which by the CCLM we will exemplify in the following.

The quasi-stationary frontal system of the EASM is mostly disturbed by cyclonic vortices, which develop over the southwestern Tibetan Plateau and travel roughly along the Yangtze river (Wang 2006). These vortices are well-known and even termed South-West Vortices (SWV). These disturbances are important ingredients to the generation of heavy rainfall events along the Meiyu band (Ding and Chan 2005). The SWVs are well resolved by the CCLM: an example is shown in Figure 4, where the CCLM simulations are compared to the representation of such a situation by ECHAM5 (figure not shown). While the feature covers 20×20 grid boxes in the CCLM simulations the same area is represented in ECHAM5 by only 4×4 grid boxes. Obviously the coarse resolution of ECHAM5 cannot resolve such a vortex structure; thus we expect that the CCLM better represents the humidity transport associated with the meso-α scale eddies and the intrinsic variability of the SWV. A more detailed analysis of the representation of such features in the CCLM and in ECHAM5 also in a statistical sense is beyond the scope of this paper and will be addressed in a follow-up study. This example gives, however, already an indication that the precipitation bias - also in the CCLM - might result at least in part from the parameterisation of precipitation processes and/or the insufficient resolution of the tropopause height. East Asia is a region with strong fluctuation of the tropopause height. The bottom height of the upper Rayleigh sponge layer in CCLM is however held constant. Thus the convection scheme might be unable to adequately represent the strong variability of tropical to sub-tropical monsoon processes. Furthermore the moisture not condensed to precipitation in the south might be transported further north where it might lead to a positive precipitation bias.

To examine the internal EASM variability on the seasonal scale the EASM index proposed by Wang and Fan (1999) and Wang et al (2008) is applied to ECHAM5-20C-all-R3 and the CCLM run driven with the former. The resulting time series of both models are highly correlated ($\rho = 0.90$, significant at 1% level) and shows that internal climate variability on the seasonal scale is transported well from the driving model to the driven model.

These results illustrate the capability of the CCLM both to represent small-scale monsoon features on the daily scale like SWVs and to maintain the internal variability on seasonal scale within the East Asia domain as provided by the driving GCM. A detailed analysis, based on post-processing the model outputs with a focus on dynamics in order to receive a bias-corrected dataset, will be the focus of a forthcoming paper.

Similar dependence structures are expected for the East Asian Winter Monsoon (EAWM), i.e. a strong coherence of the dynamics between the driving model and the driven model and a better resolution of processes on higher frequencies by the CCLM. The first point could, however, not yet be tested as standard EAWM indices require dynamics north of 50°N (Jhun and Lee 2004; Li and Yang 2010)), which coincides with the northern boundary of the simulation domain. The Siberian-Mongolian high (SMH) is a key component of the EAWM with high relevance due to its inter-annual variability (Wang 2006). Since the SMH is located close to the northern boundary of the CCLM domain, its fluctuations will be directly transported into the RCM. This assumption is supported by the example of a cold surge event shown in Figure 5 (still using the ECHAM5-20C-all-R3 driven simulation results), which is the main severe weather phenomenon during the EAWM season (Wang 2006). On January 4th an extension of the SMH enters the CCLM domain. Consequently a typical cold surge propagation of high pressure and associated cold air on ground level take place. It reaches its maximum on January 6th and weakens during an eastward drift afterwards.

4. Conclusions

The regional climate model COSMO-CLM (CCLM) is for the first time evaluated for its performance over East Asia following roughly the CORDEX recommendations. The paper analyses the annual and seasonal mean of temperature and precipitation by comparison with observations and between driving datasets and CCLM simulations. Examples are shown, which elucidate the merit of the higher spatial resolution for representing meso-α-scale processes connected to monsoon dynamics. A more comprehensive analysis based on climate indices with focus on extreme climate events is on going and will be the focus of an upcoming publication.

The evaluation results demonstrate that the CCLM, with a proper parameter tuning for East Asia, can be used for downscaling parent global fields and partially improve the results of the driving model within certain regions. Overall the CCLM performs better in simulating $2m$ temperature than precipitation. The significant cold bias over high mountain ridges (Himalaya and New Guinea) seems to be related to a wet bias in the same regions. The CCLM produces a pronounced and spatially extended wet bias in the northern part of the domain and over the Tibetan Plateau in DJF and MAM. The differences between two ECHAM5-20C driven runs, one with and one without natural forcing in the forcing data, are not significant despite a somewhat lower bias of the former run.

Based on the positive evaluation results, the projected future climate change under the A1B scenario was investigated and suggest increases from from 1 K to 2 K in annual mean temperature across whole East Asia. The annual mean total precipitation, however, is not projected to change significantly. However, due to the much higher variability and the wider uncertainty range of precipitation compared to temperature, this conclusion is preliminary since only multi-ensemble-simulations can provide reliable estimates.

Finally, a few examples highlight the potential of the CCLM to reproduce and better resolve important East Asia monsoon dynamics: the internal variability of the driving GCM on the seasonal scales is well transferred into the CCLM domain and small-scale features of monsoon dynamics such as SWV and cold surge events which cannot be modelled by ECHAM5 are simulated by CCLM and provide added value to the downscaled results.

The simulation results will be available on the CERA data base at the World Data Centre for Climate in Hamburg for future applications and improvements.

Acknowledgments.

The work was funded by the DFG project (NDFG-SCHO-1384/1-1) and BMBF project (FK:02WM1042). ERA-40 reanalysis data was provided by ECMWF. Thanks also to the CLM-Community for providing the access to the model code and further guidance, especially to Dr. Burkhardt Rockel (Helmholtz-Zentrum Geesthacht Centre for Materials and Coastal Research).

REFERENCES

Arakawa A, Lamb VR (1981) An energy and potential enstrophy conserving scheme for the shallow water equations. Mon Weather Rev 109(1):1836(19), DOI 10.1175/1520-0493(1981)109⟨0018:APEAEC⟩2.0.CO;2

Brohan P, Kennedy JJ, Harris I, Tett SFB, Jones PD (2006) Uncertainty estimates in regional and global observed temperature changes: A new data set from 1850. J Geophys Res 111(D12106), DOI 10.1029/2005JD006548

Ding YH, Chan JCL (2005) The east asian summer monsoon: an overview. Meteorol Atmos Phys 89(1-4):117–142(26), DOI 10.1007/s00703-005-0125-z

Dobler A, Ahrens B (2008) Precipitation by a regional climate model and bias correction in europe and south asia. Meteorologische Zeitschrift 17:499–509(11), DOI doi:10.1127/0941-2948/2008/0306

Fu CB, Wang SY, Xiong Z, Gutowski WJ, Lee DK, McGregor JL, Sato Y, Kato H, Kim JW, Suh MS (2005) Regional climate model intercomparison project for asia. Bull Am Meteorol Soc 86(2):257–266(10), DOI 10.1175/BAMS-86-2-257

Gao X, Xu Y, Zhao Z, Pal JS, Giorgi F (2006) On the role of resolution and topography in the simulation of east asia precipitation. Theor Appl Climatol 86(1-4):173–185(13), DOI 10.1007/s00704-005-0214-4

Giorgi F, Bates GT (1989) The climatological skill of a regional model over complex terrain. Mon Weather Rev 117(11):2325–2347(23), DOI 10.1175/1520-0493(1989)117⟨2325:TCSOAR⟩2.0.CO;2

Giorgi F, Jones C, Asrar G (2009) Addressing climate information needs at the regional level: the cordex framework. WMO Bulletin 58(3):175–183(9)

Hulme M, Zhao ZC, Jiang T (1994) Recent and future climate change in east asia. Int J Climatol 14(6):637–658, DOI 10.1002/joc.3370140604

IPCC (2007) Regional climate projections: The physical science basis in the fourth assessment report of the intergovernmental panel on climate change. IPCC

Jhun J, Lee E (2004) A new east asian winter monsoon index and associated characteristics of the winter monsoon. J Climate 17(4):711–726

Ji YM, Vernekar AD (1997) Simulation of the asian summer monsoons of 1987 and 1988 with a regional model nested in a global gcm. J Climate 10(8):1965–1979(15), DOI 10.1175/1520-0442(1997)010⟨1965:SOTASM⟩2.0.CO;2

Jones P, Harris I (2008) Cru ts 3.1

Kawase H, Yoshikane T, Hara M, Ailikun B, Kimura F, Yasunari T (2008) Downscaling of the climatic change in the mei-yu rainband in east asia by a pseudo climate simulation method. SOLA 4:73–76(4), DOI 10.2151/sola.2008-019

Kitoh A, Uchiyama T (2006) Changes in onset and withdrawal of the east asian summer rainy season by multi-model global warming experiments. J Meteo Soc of Japan 84(2):247–258(12), DOI 10.2151/jmsj.84.247

Kumar KR, Sahai AK, Kumar KK, Patwardhan SK, Mishra PK, Revadekar JV, Kamala K, Pant GB (2006) High-resolution climate change scenarios for india for the 21st century. Curr Sci 90(3):334–345(12)

Li Y, Yang S (2010) A dynamical index for the east asian winter monsoon. J Climate 23(15):4255–4262

Lorenz C, Kunstmann H (2012) The hydrological cycle in three state-of-the-art reanalyses: Intercomparison and performance analysis. J Hydrometeorol DOI doi:10.1175/JHM-D-11-088.1

Min SK, Park EH, Kwon WT (2004) Future projections of east asian climate change from multi-aogcm ensembles of ipccsres scenario simulations. J Meteor Soc Japan 82(4):1187–1211(25), DOI 10.2151/jmsj.2004.1187

Rockel B, Geyer B (2008) The performance of the regional climate model clm in different climate regions, based on the example of precipitation. Meteorologische Zeitschrift 17:487–498(12), DOI doi:10.1127/0941-2948/2008/0297

Roeckner E (2005) IPCC MPI-ECHAM5_T63L31 MPI-OM_GR1.5L40 20C3M_all run no.3: atmosphere 6 HOUR values MPImet/MaD Germany. World Data Center for Climate. CERA-DB, http://cera-www.dkrz.de/WDCC/ui/Compact.jsp?acronym=EH5-T63L31_OM_20C3M_3_6H

Roeckner E, Lautenschlager M, Schneider H (2006a) IPCC-AR4 MPI-ECHAM5_T63L31 MPI-OM_GR1.5L40 20C3M run no.1: atmosphere 6 HOUR values MPImet/MaD Germany. World Data Center for Climate, http://dx.doi.org/DOI:10.1594/WDCC/EH5-T63L31_OM-GR1.5L40_20C_1_6H

Roeckner E, Lautenschlager M, Schneider H (2006b) IPCC-AR4 MPI-ECHAM5_T63L31 MPI-OM_GR1.5L40 SRESA1B run no.1: atmosphere 6 HOUR values MPImet/MaD Germany. World Data Center for Climate, http://dx.doi.org/DOI:10.1594/WDCC/EH5-T63L31_OM-GR1.5L40_A1B_1_6H

Roeckner E, Lautenschlager M, Schneider H (2006c) IPCC-AR4 MPI-ECHAM5_T63L31 MPI-OM_GR1.5L40 SRESA1B run no.3: atmosphere 6 HOUR values MPImet/MaD Germany. World Data Center for Climate, http://dx.doi.org/DOI:10.1594/WDCC/EH5-T63L31_OM-GR1.5L40_A1B_3_6H

Rummukainen M (2010) State-of-the-art with regional climate models. WIREs Clim Change 1(1):82–96(15), DOI 10.1002/wcc.008

von Storch H, Zwiers F (1999) Statistical Analysis in Climate Research. Cambridge University Press

Trenberth KE, Stepaniak DP, Hurrell JW, Fiorino M (2001) Quality of reanalyses in the tropics. J Climate 14(7):1499–1510(12), DOI 10.1175/1520-0442(2001)014⟨1499:QORITT⟩2.0.CO;2

Uppala SM, Kllberg PW, Simmons AJ, Andrae U, Bechtold VDC, Fiorino M, Gibson JK, Haseler J, Hernandez A, Kelly GA, Li X, Onogi K, Saarinen S, Sokka N, Allan RP, Andersson E, Arpe K, Balmaseda

MA, Beljaars ACM, Berg LVD, Bidlot J, Bormann N, Caires S, Chevallier F, Dethof A, Dragosavac M, Fisher M, Fuentes M, Hagemann S, Hlm E, Hoskins BJ, Isaksen L, Janssen PAEM, Jenne R, Mcnally AP, Mahfouf JF, Morcrette JJ, Rayner NA, Saunders RW, Simon P, Sterl A, Trenberth KE, Untch A, Vasiljevic D, Viterbo P, Woollen J (2005) The era-40 re-analysis. Q J Roy Meteorol Soc 131(612):2961–3012(52), DOI 10.1256/qj.04.176, URL `http://dx.doi.org/10.1256/qj.04.176`

Wang B (2006) The Asian Monsoon. Springer Verlag

Wang B, Fan Z (1999) Choice of south asian summer monsoon indices. Bull Am Meteorol Soc 80:629–638

Wang B, Wu Z, Li J, Liu J, Chang C, Ding Y, Wu G (2008) How to measure the strength of the east asian summer monsoon. J Climate 21(17):4449–4463

Williams PD (2009) A proposed modification to the robert–asselin time filter. Mon Weather Rev 137(8):2538–2546, DOI 10.1175/2009MWR2724.1

Xie P, Yatagai A, Chen M, Hayasaka T, Fukushima Y, Liu C, Yang S (2007) A gauge-based analysis of daily precipitation over east asia. J Hydrometeorol 8(3):607–626(20), DOI 10.1175/JHM583.1

Xu Y, Zhao Z, Luo Y, Gao X (2005) Climate change projections for the 21st century by the ncc/iap t63 with sres scenarios. Acta Meteor Sinica 19:407–417

Yatagai A, Arakawa O, Kamiguchi K, Kawamoto H, Nodzu MI, Hamada A (2009) A 44-year daily gridded precipitation dataset for asia based on a dense network of rain gauges. Sci online Letters on the atmosphere (SOLA) 5:137–140, DOI 10.2151/sola.2009-035

Yhang YB, Hong SY (2008) Improved physical processes in a regional climate model and their impact on the simulated summer monsoon circulations over east asia. J Climate 21(5):963–979(17), DOI 10.1175/2007JCLI1694.1

Zhang L, Wu T, Xin X, Dong M, Wang Z (2012) Projections of annual mean air temperature and precipitation over the globe and in china during the 21st century by the bcc climate system model bcccsm1.0. Acta Meteor Sinica 26(3):362–375, DOI 10.1007/s13351-012-0308-8

List of Tables

Table 1. Grid specifications of the simulations.

Atmosphere		
	Horizontal Grid	
	longitude	latitude
Rotated north pole location	-64.78	77.61
Rotated grid extension	-47.96 to 55.44	-33.88 to 53.68
Rotated grid resolution	0.44	0.44
Number of grid points	235	199
	Vertical Grid	
Number of vertical layers	32	
Soil		
Number of soil layers	10	
Soil layer depth [m]	0.01, 0.035, 0.08, 0.17, 0.35, 0.71, 1.43, 2.87, 5.75, 11.51	

TABLE 2. Basic model configuration parameters of the CCLM.

Model Configuration	
Convection scheme	Tiedtke
Time integration scheme	Leapfrog, time step = 150 s
Robert-Asselin time filter (alphaass)	0.7
Lateral relaxation layer (rlwidth) [km]	800
Rayleigh damping layer (rdheight) [km]	13
Microphysics scheme	Kessler-type (1969)
Turbulence scheme	Prognostic turbulent kinetic energy (TKE)
Radiation scheme	Ritter and Geleyn (1992)

TABLE 3. Annual mean $2m$ temperature and averaged annual sum total precipitation bias for each subregion over the period 1971-2000. Shown here are the ERA-40 driven CCLM run and the respective ERA-40 biases compared to CRU-TS3.0 and APHRODITE for temperature and precipitation, respectively.

Subregion	temperature bias		precipitation bias			
	CCLM	ERA-40	CCLM		ERA-40	
	$[K]$	$[K]$	$[mm]$	[%]	$[mm]$	[%]
Central China	0.39	−0.83	141.05	18.19	110.02	14.19
Central	−0.27	−0.49	478.82	31.42	348.99	22.90
East Indonesia	−0.88	0.11	1530.18	88.55	3454.35	199.89
Indo China	−0.69	0.01	325.64	22.82	653.68	45.80
North China	2.45	0.28	67.33	41.05	45.44	27.70
North East China	1.32	0.70	175.28	30.83	74.63	13.13
North East	0.73	1.48	217.05	30.21	217.53	30.28
North India	1.63	−1.32	291.15	28.44	65.66	6.41
North	2.28	1.30	139.02	44.40	290.48	92.78
North West	2.17	0.06	−39.67	−13.64	127.06	43.69
Philippines	−0.37	1.38	12.25	0.58	1495.85	70.25
South China	0.29	0.34	−71.99	−5.18	−128.52	−9.24
South India	1.65	0.06	−227.12	−22.74	−95.90	−9.60
South Japan	−0.63	2.43	−231.80	−13.48	−224.97	−13.08
Tarim Basin	1.90	−1.34	103.97	113.06	235.40	255.98
Tibetan Plateau	−0.51	0.38	524.89	130.60	887.75	220.89
West Indonesia	0.01	−0.01	4.55	0.24	870.64	45.92
CORDEX-easia	0.82	0.22	239.86	28.02	471.53	55.08

TABLE 4. Annual mean $2m$ temperature and averaged annual sum total precipitation bias for each subregion over the period 1971-2000. Shown here are the ECHAM5-20C-R1 driven CCLM run and the respective ECHAM5-20C-R1 biases compared to CRU-TS3.0 and APHRODITE for temperature and precipitation, respectively.

Subregion	temperature bias		precipitation bias			
	CCLM	ECHAM5-20C-R1	CCLM		ECHAM5-20C-R1	
	$[K]$	$[K]$	$[mm]$	[%]	$[mm]$	[%]
Central China	0.37	−2.34	92.62	11.95	692.65	89.34
Central	0.51	−0.37	282.23	18.52	−285.12	−18.71
East Indonesia	−0.68	1.81	1255.07	72.63	925.30	53.54
Indo China	0.53	−0.07	−265.16	−18.58	−127.29	−8.92
North China	1.69	0.50	124.86	76.12	121.00	73.77
North East China	0.13	−0.64	218.22	38.39	275.75	48.51
North East	−0.34	0.05	392.05	54.57	321.27	44.72
North India	1.93	−0.17	318.06	31.07	−144.08	−14.07
North	1.01	0.22	364.30	116.35	238.54	76.19
North West	2.06	1.23	123.10	42.33	7.64	2.63
Philippines	−0.33	2.04	−310.12	−14.57	852.57	40.04
South China	1.20	0.43	−297.92	−21.42	−129.42	−9.31
South India	0.54	−0.40	−104.06	−10.42	28.24	2.83
South Japan	0.10	4.22	−116.73	−6.79	−39.58	−2.30
Tarim Basin	1.71	−0.98	180.76	196.56	136.56	148.50
Tibetan Plateau	−1.01	1.03	472.09	117.46	683.47	170.06
West Indonesia	0.21	0.32	−246.59	−13.01	395.62	20.87
CORDEX-easia	0.59	0.28	183.48	21.43	221.59	25.88

TABLE 5. Annual mean $2m$ temperature and averaged annual sum total precipitation bias for each subregion over the period 1971-2000. Shown here are the ECHAM5-20C-all-R3 driven CCLM run and the respective ECHAM5-20C-all-R3 biases compared to CRU-TS3.0 and APHRODITE for temperature and precipitation, respectively.

Subregion	temperature bias		precipitation bias			
	CCLM	ECHAM5-20C-all	CCLM		ECHAM5-20C-all-R3	
	$[K]$	$[K]$	$[mm]$	[%]	$[mm]$	[%]
Central China	0.46	−2.39	40.27	5.19	660.73	85.22
Central	0.29	−0.70	291.79	19.15	−243.62	−15.99
East Indonesia	−0.74	1.61	1172.01	67.82	935.84	54.15
Indo China	0.40	−0.26	−302.83	−21.22	−145.19	−10.17
North China	1.52	0.39	105.19	64.13	106.51	64.93
North East China	−0.19	−0.99	226.70	39.88	262.45	46.17
North East	−0.63	−0.48	403.50	56.16	312.59	43.51
North India	1.63	−0.33	263.97	25.79	−150.86	−14.74
North	0.75	0.00	388.45	124.07	249.66	79.74
North West	1.85	1.16	118.25	40.66	−4.16	−1.43
Philippines	−0.44	1.85	−356.47	−16.74	786.65	36.95
South China	1.05	0.13	−310.27	−22.31	−108.74	−7.82
South India	0.47	−0.52	−114.43	−11.46	6.39	0.64
South Japan	−0.05	3.94	−155.75	−9.05	−86.90	−5.05
Tarim Basin	1.62	−1.02	135.29	147.12	115.38	125.46
Tibetan Plateau	−1.16	0.97	464.60	115.60	671.69	167.13
West Indonesia	0.09	0.19	−310.80	−16.39	338.21	17.84
CORDEX-easia	0.41	0.09	164.58	19.23	212.46	24.82

TABLE 6. Annual mean $2m$ temperature and total precipitation driven by ECHAM5-A1B-R1 over the period 2021-2050 compared to the hindcast run (1971-2000) driven by ECHAM5-20C-R1.

Subregion	temperature anomaly		precipitation anomaly			
	CCLM	ECHAM5-A1B-R1	CCLM		ECHAM5-A1B-R1	
	$[K]$	$[K]$	$[mm]$	[%]	$[mm]$	[%]
Central China	1.57	1.43	−53.64	−6.18	2.55	0.17
Central	1.19	1.11	1.26	0.07	50.17	4.05
East Indonesia	0.98	1.04	−79.46	−2.66	−83.56	−3.15
Indo China	0.96	1.00	50.32	4.33	51.77	3.98
North China	1.48	1.68	−11.57	−4.01	−3.86	−1.35
North East China	1.41	1.46	8.03	1.02	2.94	0.35
North East	1.22	1.25	19.72	1.78	27.44	2.64
North India	1.49	1.56	19.35	1.44	4.60	0.52
North	1.44	1.61	25.43	3.75	33.78	6.12
North West	1.66	1.86	14.48	3.50	14.43	4.83
Philippines	0.97	0.98	109.59	6.02	107.69	3.61
South China	1.40	0.95	−45.66	−4.18	79.60	6.31
South India	1.25	1.36	62.20	6.95	27.55	2.68
South Japan	1.24	1.10	17.16	1.07	13.34	0.79
Tarim Basin	1.70	1.91	−21.29	−7.81	−17.25	−7.55
Tibetan Plateau	1.83	1.73	−32.59	−3.73	−22.01	−2.03
West Indonesia	1.01	1.02	13.46	0.82	92.93	4.06
CORDEX-easia	1.39	1.41	−2.02	−0.19	17.81	1.65

TABLE 7. Annual mean $2m$ temperature and total precipitation driven by ECHAM5-A1B-R3 over the period 2021-2050 compared to the hindcast run (1971-2000) driven by ECHAM5-20C-all-R3.

Subregion	temperature anomaly		precipitation anomaly			
	CCLM	ECHAM5-A1B-R3	CCLM		ECHAM5-A1B-R3	
	$[K]$	$[K]$	$[mm]$	[%]	$[mm]$	[%]
Central China	1.48	1.37	−53.41	−6.55	1.28	0.09
Central	1.28	1.29	−18.72	−1.03	−3.75	−0.29
East Indonesia	1.12	1.17	−107.37	−3.70	−73.63	−2.76
Indo China	1.03	1.06	84.07	7.48	91.73	7.16
North China	1.55	1.68	0.88	0.33	16.41	6.07
North East China	1.78	1.84	−2.75	−0.35	34.99	4.21
North East	1.68	1.93	1.60	0.14	32.86	3.19
North India	1.40	1.30	38.52	2.99	68.44	7.84
North	1.69	1.84	−14.13	−2.01	−0.45	−0.08
North West	1.84	1.97	−4.63	−1.13	2.26	0.79
Philippines	1.08	1.10	111.32	6.28	64.24	2.20
South China	1.41	1.25	−33.72	−3.12	11.53	0.90
South India	1.26	1.37	55.99	6.33	17.72	1.76
South Japan	1.31	1.28	34.14	2.18	29.97	1.84
Tarim Basin	1.58	1.70	7.07	3.11	11.92	5.75
Tibetan Plateau	1.56	1.49	−6.83	−0.79	4.07	0.38
West Indonesia	1.13	1.14	36.00	2.27	119.65	5.36
CORDEX-easia	1.47	1.50	0.81	0.08	23.50	2.20

List of Figures

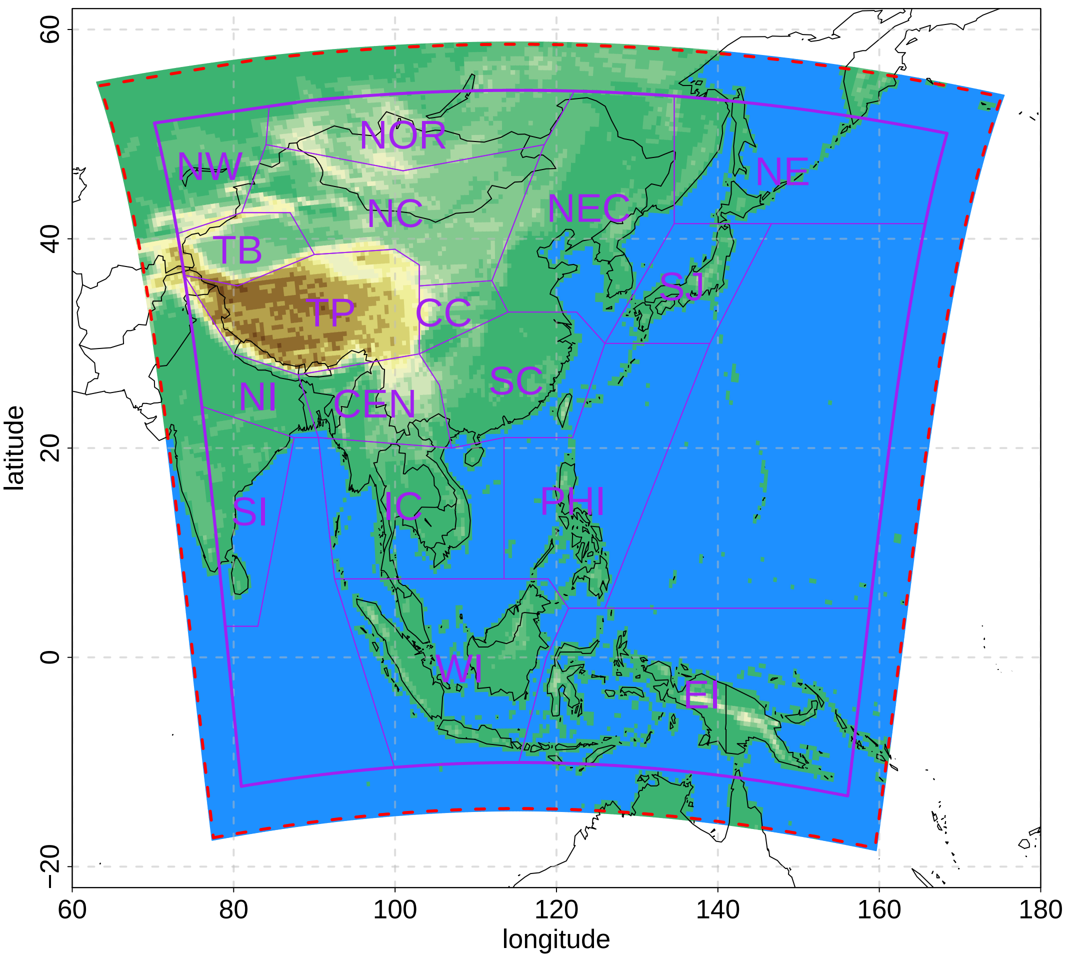

FIG. 1. The study region: the simulation domain of the CCLM is bounded by the red dotted line and the evaluation region is outlined with the solid purple line. For the evaluation purpose the domain is divided into the following subregions: **NW** - Noth West, **NOR** - North, **NEC** - North East China, **NE** - North East **TB** - Tarim Basin, **NC** - North China, **CC** - Central China, **SJ** - South Japan, **TP** - Tibetan Plateau, **SC** - South China, **PHI** - Phillippines, **NI** - North India, **SI** - South India, **CEN** - Central, **IC** - Indochina, **WI** - West Indonesia and **EI** - East Indonesia.

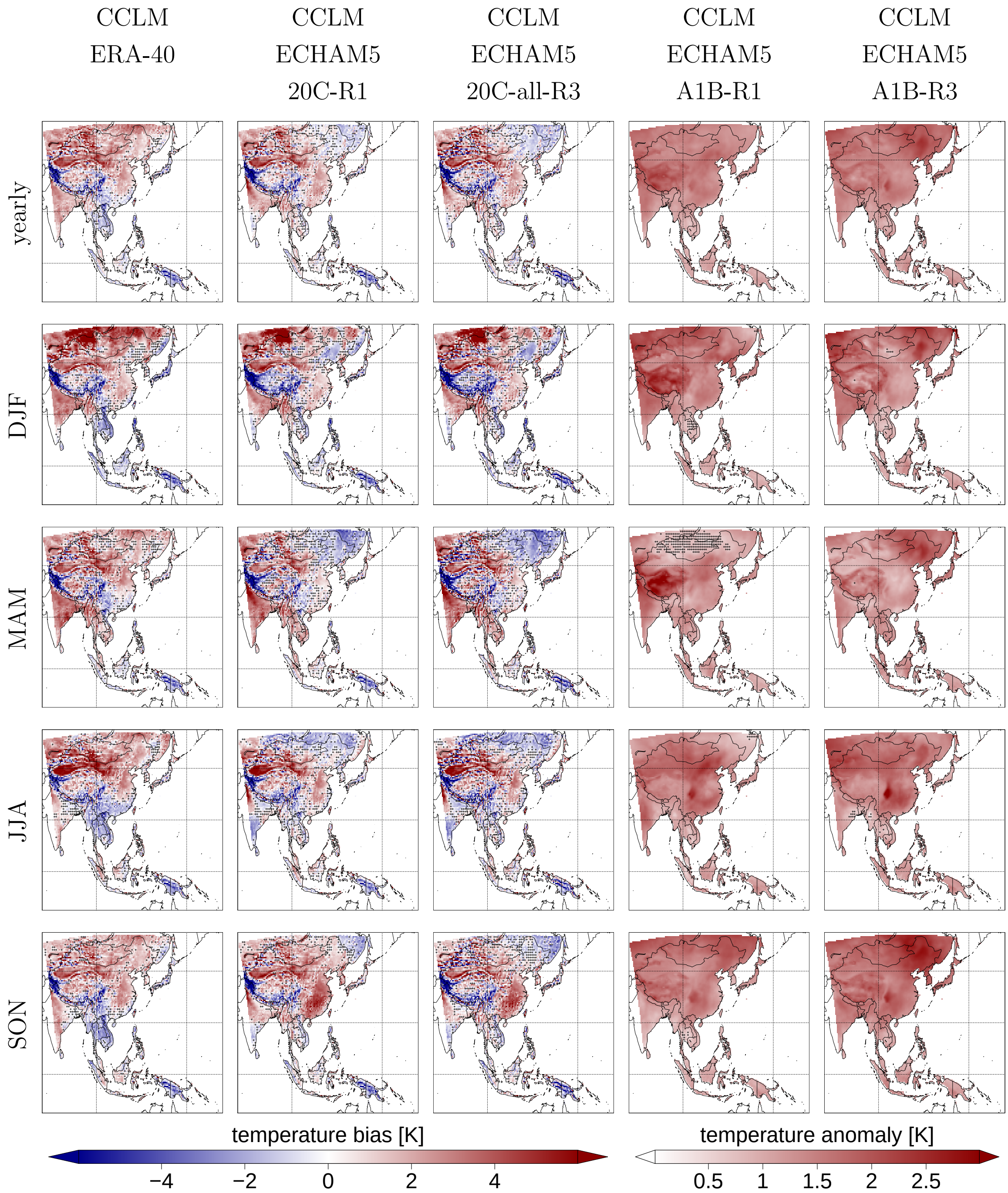

FIG. 2. The temperature bias of the five simulations. The hindcast simulations over the period 1971-2000 are compared to CRU-TS3.0, while the future projections over the period 2021-2050 are compared to their respective hindcast runs. Shaded areas indicate the regions with differences below 0.9 probability.

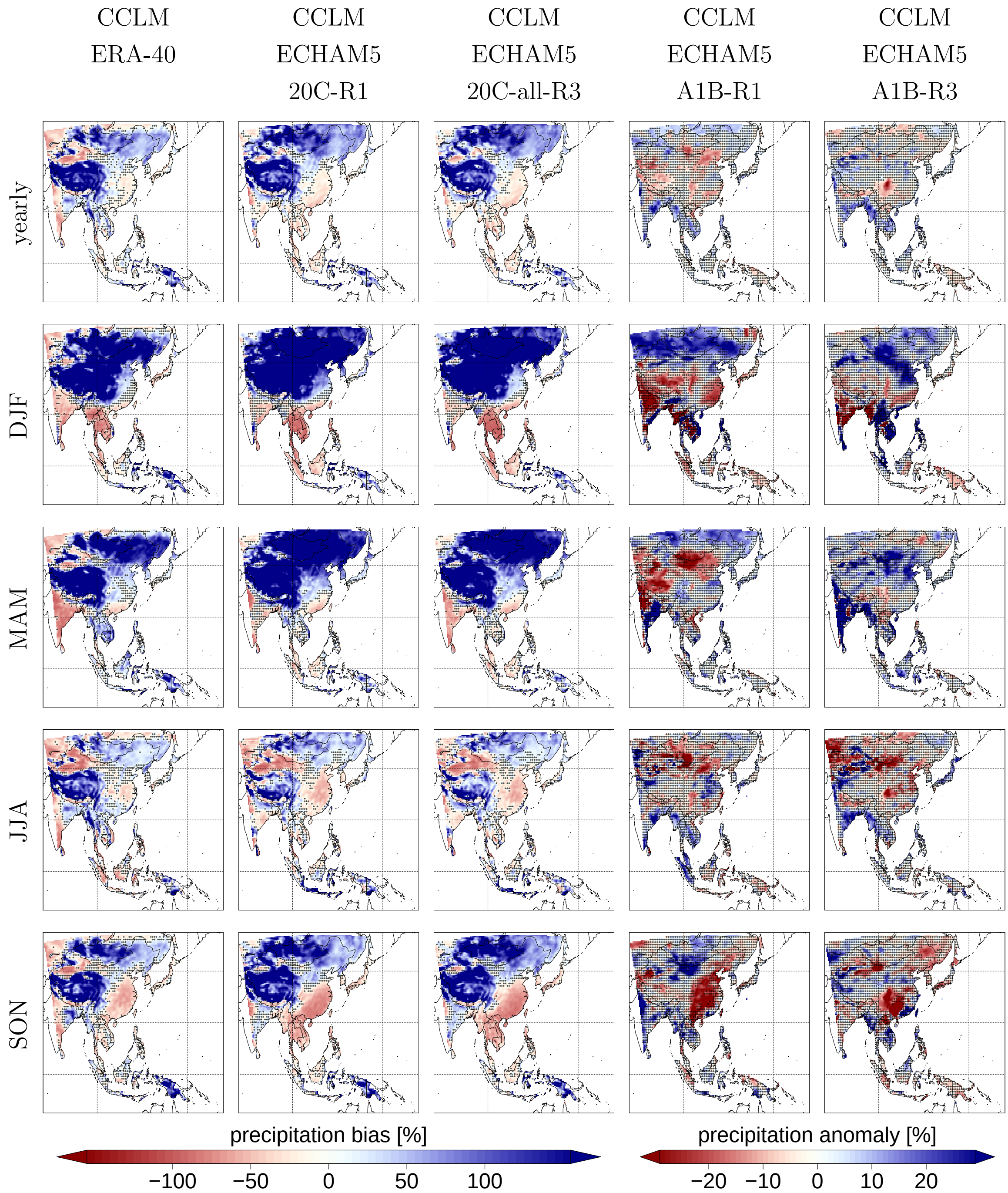

FIG. 3. The relative precipitation bias of the five simulations. The hindcast simulations over the period 1971-2000 are compared to APHRODITE-APHRO_V1003R1, while the future projections over the period 2021-2050 are compared to their respective hindcast runs. Shaded areas indicate the regions with differences below 0.9 probability.

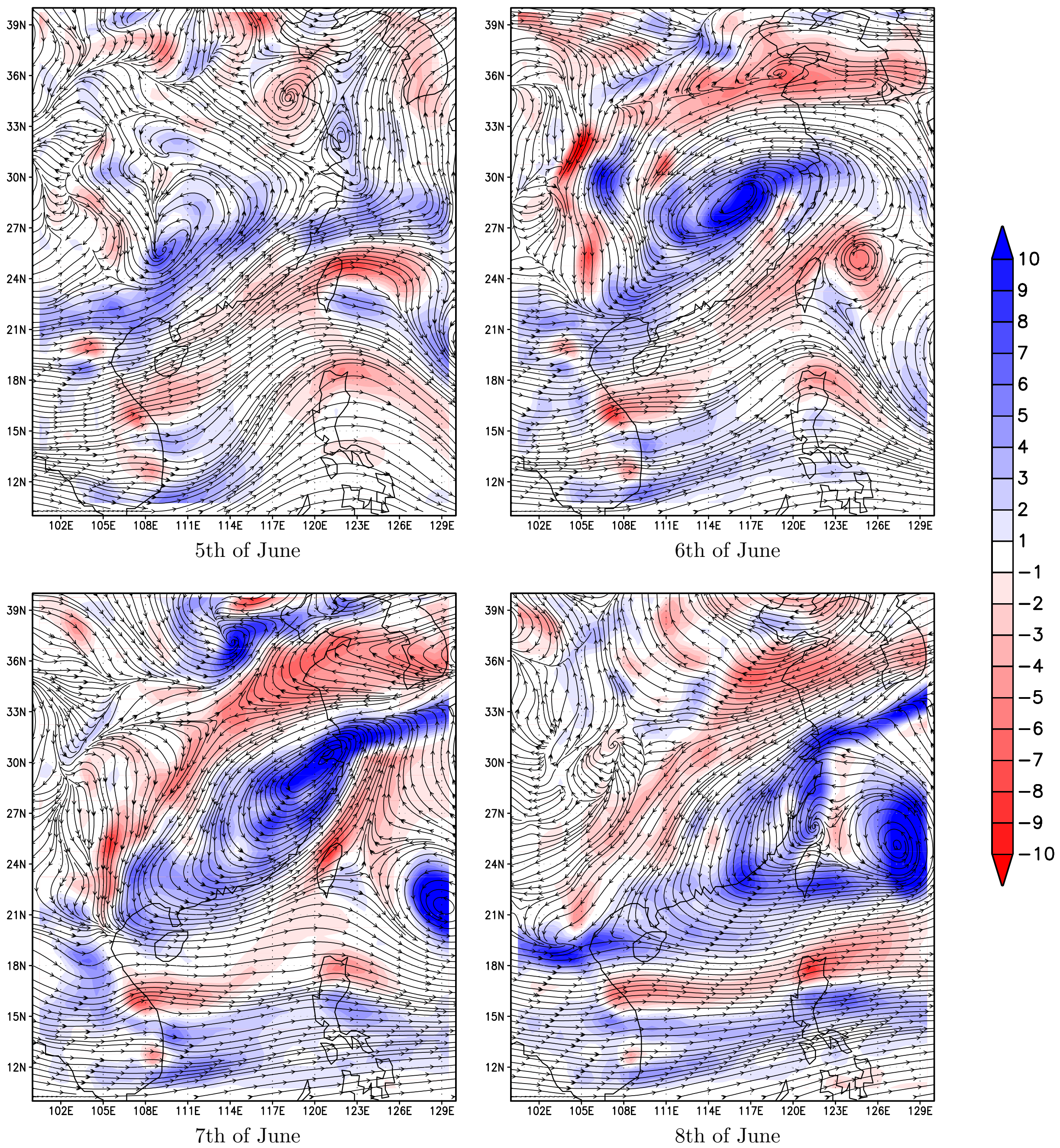

Fig. 4. A case study of a Southwest Vortex, which occured on the beginning of June over Southern China and is visible in the windfield at 850hPa. The arrows at the streamlines show the wind direction. The shaded background indicates the amplitude of the relative vorticity in 10^{-5}/s. The data is taken from the CCLM run driven by ECHAM5-20C-all-R3.

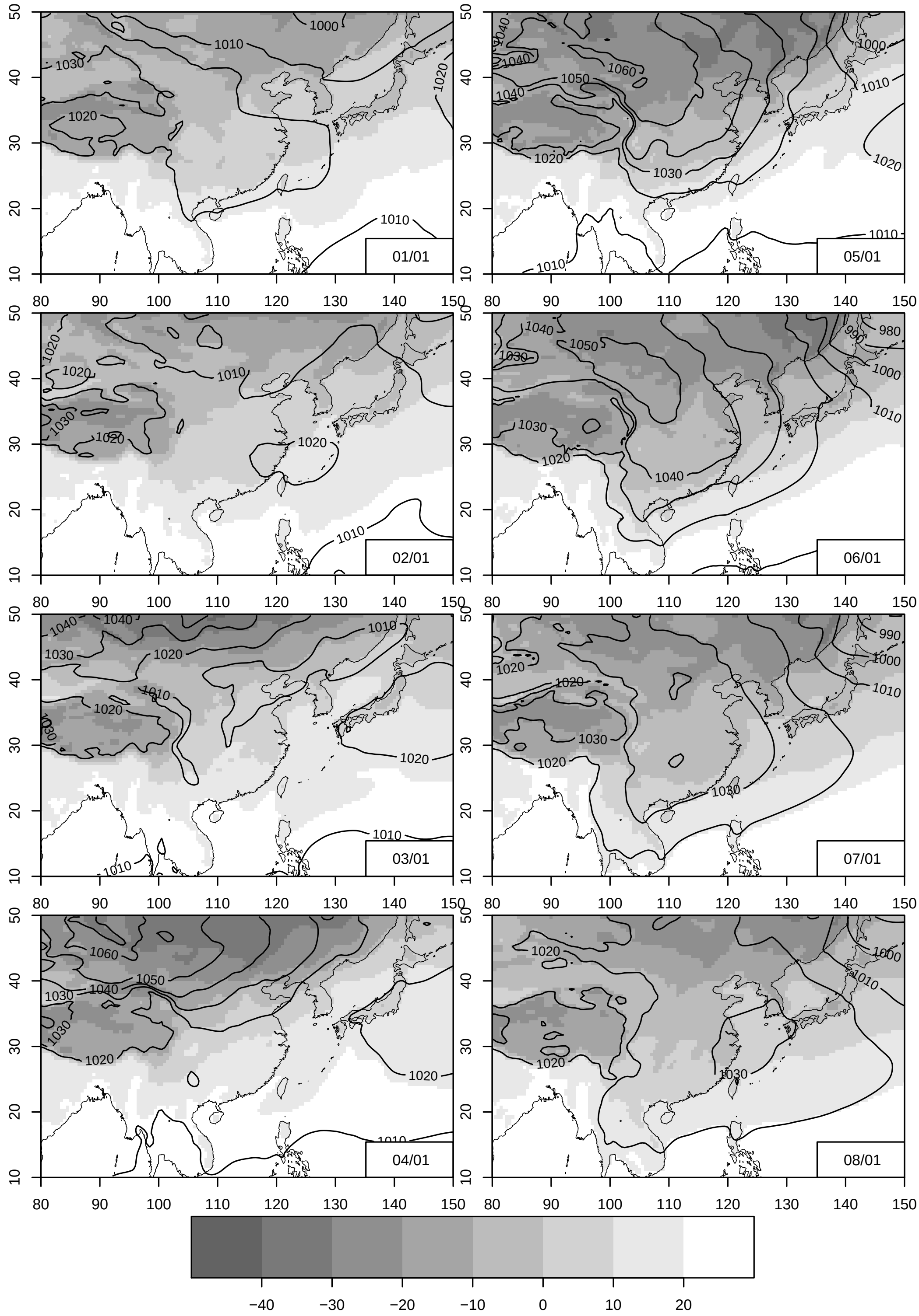

FIG. 5. The analysis of sea level pressure and temperature at ground level shows a cold surge event. Contour lines mark isobars in hPa. The shaded background displays the 2m temperature in °C.

Appendix B

Generation and transfer of internal variability in a regional climate model

The following manuscript has been published in the peer-reviewed journal *Tellus A* in 2013.

Attribution of roles

Thorsten Simon designed the evaluation method. Dinan Wang, Clemens Simmer and Christian Ohlwein designed the experimental set-up for the RCM simulations. Dinan Wang performed the RCM simulations, parts of which are published for the first time. Andreas Hense contributed to the development of the evaluation method. All authors discussed the results and commented on the manuscript.

Tellus SERIES A DYNAMIC METEOROLOGY AND OCEANOGRAPHY
PUBLISHED BY THE INTERNATIONAL METEOROLOGICAL INSTITUTE IN STOCKHOLM

Generation and transfer of internal variability in a regional climate model

By THORSTEN SIMON[1]*, DINAN WANG[2], ANDREAS HENSE[1], CLEMENS SIMMER[1] and CHRISTIAN OHLWEIN[1,3], [1]*Meteorological Institute, University Bonn, Bonn, Germany*; [2]*Institute for Energy Systems and Energy Business, Hochschule Ruhr West, Mülheim, Germany*; [3]*Hans-Ertel Centre for Weather Research, Climate Monitoring Branch, Germany*

(Manuscript received 29 July 2013; in final form 20 November 2013)

ABSTRACT

There is a strong need for tools allowing the comparison between the performance of a regional climate model (RCM) and the corresponding model providing lateral boundary conditions (LBC) for the RCM, which is a global general circulation model (GCM) in most cases. A method is presented to investigate the temporal scales on which a RCM is able to generate internal variability on its own and on which variability is copied from the driving model. This is implemented by a cross-spectral analysis between the RCM output and a bi-linearly interpolated version of the driving model, leading to an estimate of the coherence spectrum. Applying the aforementioned technique to surface temperature and temperature and specific humidity at 850 hPa from the RCM COSMO-CLM East Asia with a horizontal resolution of 50 km and its driving model ECHAM5, it was found that features in the spatial distribution of coherence are related to atmospheric dynamics in East Asia, e.g. monsoons and inter-tropical convergence zone (ITCZ). A further application to a double-nesting approach, where COSMO-CLM East Asia is the driving model for two domains – namely the Haihe catchment and the Poyang catchment – each with a horizontal resolution of 7 km, shows that the frequencies on which internal variability is generated by the driven model are much higher compared to the first nesting step. Concluding RCMs can produce a considerable variability on the respective temporal scales. This implies that a dynamical downscaling with a re-analysis as LBC is conceptually different to a regional re-analysis, i.e. data assimilation on the regional scale.

Keywords: East Asia, COSMO, cross-spectrum, internal variability, dynamical downscaling, nesting, double-nesting

1. Introduction

Assessing and projecting climate change is usually based on global general circulation models (GCMs). Due to high computational cost, the spatial resolution of GCMs is limited. This results in grid boxes with areas of the order of 10^4 km^2 (Roeckner et al., 2003; Uppala et al., 2005) and even lower effective resolutions. Studies investigating the energy spectra of numerical weather prediction models (NWPs) (Skamarock, 2004; Bierdel et al., 2012) suggest effective resolutions about 4–7 times coarser than the original grid. In addition, the low horizontal resolution of GCMs leads to a weak representation of local extreme events (Easterling et al., 2000), which is associated with the *change of support effect* (Wackernagel, 2010).[1]

To add additional regional information to the global input and to keep computational cost on an acceptable level, dynamical downscaling via regional climate models (RCMs) (e.g. Giorgi et al., 2001; Frei et al., 2006; Gao et al., 2008; Rummukainen, 2009) became an established method over the past 10–20 yr. The popularity of RCMs is also caused by the increasing demand for high-resolution data from other disciplines, e.g. hydrology, biology (e.g. Kuemmerlen et al., 2012; Schmalz et al., 2012). This led the

*Corresponding author.
email: tsimon@uni-bonn.de

[1]In geostatistics *support* is the interval, surface or volume, for which a value represents the average. The change of support effect refers to the circumstance that the variance of a variable averaged over an extended area, e.g. a grid-box, has to be less than the variance at a local point. (Wackernagel, 2010).

Citation: Tellus A 2013, **65**, 22485, http://dx.doi.org/10.3402/tellusa.v65i0.22485

World Climate Research Programme (WCRP) to establish the Coordinated Regional Climate Downscaling Experiment (CORDEX) with the goal to coordinate and to keep record of RCM simulations undertaken by research groups all over the world (Giorgi et al., 2009). Within CORDEX, 13 RCM domains are defined covering the globe. Examples of a CORDEX-based effort are the RCM ensemble simulations performed for Europe (EURO-CORDEX, see Vautard et al., 2013), Africa (CORDEX-Africa, see Nikulin et al., 2012) and within the North American Regional Climate Change Assessment Program (NARCCAP, see Mearns et al., 2012).

One conceptual shortcoming of RCMs is emphasized here, as it is closely related to the generation of internal variability in RCMs. While GCMs integrate the coupling between multiple components of the climate system – at least atmosphere and ocean (hydrosphere), but also cryosphere, biosphere and lithosphere – RCMs restrict the coupling usually to biosphere and lithosphere via so-called land surface models (Giorgi et al., 2001). Due to the usually applied one-way nesting technique of RCMs – as it is also the case in our simulations – one drawback of these simulations is that teleconnections are not included and hence large-scale climate feedbacks are suppressed. For example, in a RCM adapted to East Asia the monsoon systems do not influence ENSO, while ENSO signals are transmitted via lateral boundary conditions (LBC) as it was simulated in the driving GCM (Wang et al., 2005). Furthermore, air–sea interactions are no part of most RCM simulations as the SST of the driving GCM is often used as a lower boundary instead of a dynamical ocean component (Hagedorn et al., 2000) or at least a slab ocean, which would model the damping effect of the ocean mixed layer and hence allow to store heat in the ocean (Lorbacher et al., 2006; Dommenget, 2010).

The main purpose of RCM simulations is to explicitly resolve and thus not to parameterize processes at finer spatial and temporal scale. Therefore, internal variability is generated on scales, which are not modelled by global GCMs. This self-generated internal variability is often referred to as *added value* of a RCM simulation compared to a GCM, though *added value* is often also defined as the ability of a RCM to modify the externally forced variability. After all, there is still demand for basic research about the credibility of RCMs. Therefore, there is a strong need for studies on the comparison of RCM simulations and their driving models (Laprise et al., 2008; Feser et al., 2011). After reviewing literature (see references below), three categories of different definitions of added value can be identified. In the first category, added value is defined in terms of estimating the level of the *change of support effect* between global and regional simulations compared to point-like observations. In the second and third category, added value is described as the gain of internal variability at small spatial and temporal scales, respectively.

The definition of added value on the basis of verification has been applied in studies dealing with different models, e.g. regional models driven by re-analysis data, NWP models and regional models driven by global climate simulations. Feser (2006) compared two RCM simulations – with and without spectral nudging (von Storch et al., 2000) – and the NCEP re-analysis with the analysis generated by the model run operationally at Germany's National Meteorological Service (DWD). Applying a spatial filter technique to separate spatially large and regional scale signal, it was found that the spectrally nudged RCM leads to the best reproduction of the observations. The investigation of a double-nesting approach for East Asia showed the ability to reconstruct single events like typhoons more realistically than in the original re-analysis data (Feser and von Storch, 2008). A comparison between near surface wind speed of spectrally nudged RCM simulations driven by re-analysis data and QuikSCAT observations exhibited added value, especially along coastlines and for regions with complex terrain (Winterfeldt and Weisse, 2009). Using a verification approach based on Bayesian statistics, Röpnack et al. (2013) showed the ability of the COSMO-DE convection permitting ensemble prediction system (COSMO-DE-EPS, 2.8 km grid) to forecast the probability of tropospheric temperature profiles in a superior manner compared to two other COSMO-based ensembles (each 10 km grid). Another study falling in this first category is an analysis of the NARCCAP ensemble (Di Luca et al., 2012). This analysis does not use the original data of the driving model, but uses an upscaling technique for the RCM output, which works as a filter for high-resolution variability. The added value of a RCM is defined as the improvement of the representation of climate statistics, e.g. the 95th quantile of precipitation. Thus, this first category is not restricted to studies dealing with re-analysis and NWP models, and also includes studies investigating climate simulations.

There are different approaches to assess added value in terms of spatial small-scale variability, which refers to the second category of definitions. Via spatial spectral analysis (Errico, 1985) of kinetic energy and moisture flux convergence, it was revealed that the RCM increases variability on smaller scales in comparison to the driving re-analysis (Rockel et al., 2008a). Using the same spectral technique, it was found that the sensitivity of a RCM to surface forcing depends on the implemented convection scheme (Castro et al., 2005). A special way to evaluate the added value of a RCM is the so-called 'Big-Brother Experiment' (BBE) (Denis et al., 2002). Here, both a Big-Brother and a Little-Brother have to be generated by a RCM and compared afterwards, with the Big-Brother working as a *mentor* for the Little-Brother: First, the high-resolution Big-Brother data is filtered to remove fine-scale variability. Second, the filtered Big-Brother is used as a driving dataset for the Little-Brother. This allows us to evaluate RCM specific errors. The downside of this method is the high computational costs. Nevertheless, an important outcome of studies analysing BBEs is that the merit of a RCM simulation emerges rather when a large domain is setup than in the case of a smaller domain. In the first case, more internal variability on small spatial scales develops compared to the second case (Laprise et al., 2012).

We follow a third way of defining added value. Added value is the ability of the regional model to generate internal variability on temporal frequencies in opposition to variability that is transferred from the driving model. The ratio of the univariate spectra of both models – computed with time series of single grid boxes that have close to equal locations – shows the increase of variance in the RCM (Fig. 1). However, we are aiming at investigating the contribution of the RCM in terms of developing dynamics on small temporal scales. This kind of approach is feasible with coherence spectra between both models (Section 3).

Considering the effective resolution of a circulation model, which is known from experimental studies on the mesoscale to be about 4–7 times coarser than the original grid (e.g. Bierdel et al., 2012), leads to a rough estimate for the spatial scales. The 50-km horizontal grid spacing of a RCM runs would result in an effective resolution of 200–350 km. The driving model ECHAM5 has a horizontal resolution of T63, which equals a resolution of 630 km at the equator in spectral space. Added value would then be expected at spatial scales from 350 to 600 km. The corresponding temporal scales with respect to atmospheric

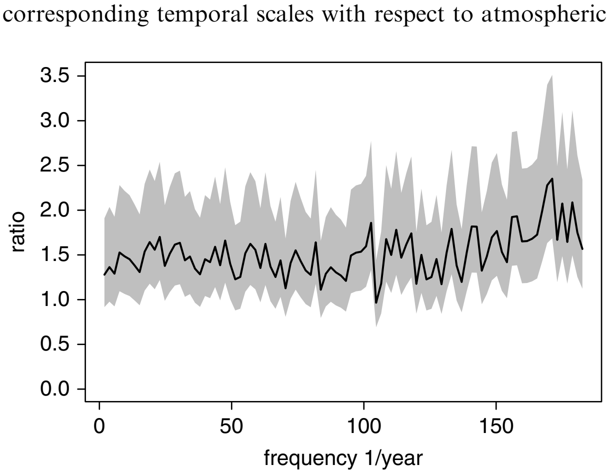

Fig. 1. Exemplary ratio of the RCM spectrum and the GCM spectrum for one grid cell in the Pacific (140°E, 20°N) for T850 in winter taken from the '20C' experiment. The shaded area indicates the 95% confidence interval.

processes lie in a range between 1 h and 1 d (Orlanski, 1975), but this rough estimate for the temporal scales leaves open the question as to whether the involved regional model has the ability to develop dynamics on these scales.

In this paper, we address the problem, on which temporal scales added value can be expected. A method, based on cross-spectral analysis (Section 3), is proposed to investigate the potential of a RCM to adapt and self-generate internal variability. The method is applied to simulations over East Asia with COSMO-CLM and ECHAM5. Both a nesting and a double-nesting approach are analysed (Section 2). The results presented in detail in Section 4 are discussed in Section 5, with the focus set on special issues that require further explanations and on added value of RCM simulations in general. Special attention is given to a conceptual formulation of the methodology (Section 6). Section 7 contains concluding remarks and proposes further applications for the method.

2. Data

The basis for this study is RCM simulations for East Asia (Fig. 2) performed with the COSMO-CLM (**CO**nsortium for **S**mall-scale **MO**delling–**C**limate **L**imited area **M**odel, Rockel et al., 2008b). The domain covers both tropical and extra-tropical regions. The centre of the domain is located above eastern China, where the East Asian Summer Monsoon dominates the regional climate during summer (Ding and Chan, 2005; Simon et al., 2013). The model is integrated on a 0,44°grid (about 50 km) and forced by LBC once every six hours, using a sponge zone with a width of 10 grid points on each side. One run is forced by ECHAM5 20C3M_all run no.3[2] (hereafter: ECHAM5) (Roeckner, 2005), another one by ECHAM5 A1B run no.3,[3] and a third run by the ECMWF 40 yr Re-analysis (ERA-40) (Uppala et al., 2005). For further details on the adaption of COSMO-CLM to the domain and on physical and numerical parameters, the reader is referred to Wang et al. (2013). However, an extract of the model parameters is given in Table 1. Wang et al. (2013) also discussed how typical summer and winter weather phenomena for East China are represented in the model. The basic concept of the analysis is the comparison of the output of the driving model with the output of the driven model. To this end, the coarse data (ECHAM5, ERA 40) is bi-linearly interpolated

[2]The ECHAM5 20C3M_all simulations are driven with anthropogenic forcing (CO_2, CH_4, N_2O, CFCs, O_3 and sulphate) and natural forcing (variable solar forcing and effect of volcanic aerosols).

[3]The A1B scenario assumes a balanced mix of energy sources for the 21st century (Nakicenovic et al., 2000).

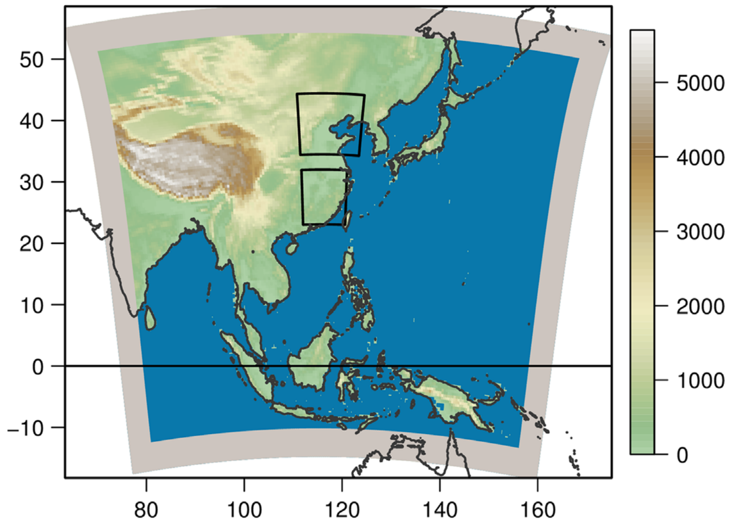

Fig. 2. Orography [m a.m.s.l.] for the East Asia domain in 0,44°resolution. The grey frame indicates the sponge zone. Two subdomains (North—Haihe, South—Poyang) are highlighted by boxes.

to the grid of COSMO-CLM. For the spectral analysis (cf. Section 3), only daily mean values were used. The main focus is set on temperature at 2 m (T_2M), temperature at 850 hPa (T850) and specific humidity at 850 hPa (Q850). This choice of variables allows us to analyse differences of the properties at the surface and in the lower atmosphere (T_2M vs. T850), as well as to account for specific features for the water cycle (Q850 vs. T850).

In addition to the 0,44° model, a double-nesting approach has been applied to two smaller regions simultaneously. The motivation for the double-nesting approach is to enter a very fine spatial resolution representing more details of the topography. The first region is the catchment of the Haihe river in the Northeast of China, and the second region is the catchment of the Poyang lake in the Southeast of China (Fig. 2). The resolution for both of these domains is 0,0625° (7 km), but the areal extend of both domains differs. The calculation was run on a 160×160 and a 128×144 grid (excluding the lateral sponge zone) for the Haihe catchment and the Poyang catchment, respectively. These simulations were driven by the output of the 50 km run forced by ECHAM5 20C3M. Again, the output of the 50 km run is bi-linearly interpolated to the grids of the Haihe domain and the Poyang domain, respectively. As the spatial resolution of the model is finer – 7 km vs. 50 km – added value is also expected on shorter time scales. Therefore, the data was taken in a temporal resolution of one value per hour for this analysis, which is only available for T_2M. An overview of the simulations performed for East Asia by COSMO-CLM and an extract of the model parameters is given in Table 1.

Table 1. Simulations performed with COSMO-CLM for East Asia

	Single-nesting	Double-nesting Haihe	Double-nesting Poyang
Model	COSMO_4.8_CLM_11 (and higher)		
Horizontal resolution	0,44° (50 km)	0,0625° (7 km)	
Horizontal grid size (excl. sponge zone)	183×147	160×160	128×144
Timestep	150s	60s	
Convection scheme	Tiedtke		
Time interval for boundary conditions	6 hours		
Driving model & simulated period	ERA40 1971–2000 (CCLM_eval_50km)	CCLM_eval_50km 1971–2000	CCLM_eval_50km 1971–1975
	ECHAM5_20C3M_all_3 1971–2000 (CCLM_20C_50km)	CCLM_20C_50km 1971–2000	CCLM_20C_50km 1971–1997
	ECHAM5_A1B_3 2011–2050 (CCLM_A1B_50km)	CCLM_A1B_50km 2021–2050	CCLM_A1B_50km 2021–2050

3. Methods

The basis of our methodology is a cross-spectral analysis. Before the estimation of the spectral parameters can be applied, the time series should be filtered from obvious periodic signals, e.g. (semi-) annual cycle and diurnal cycle, which is done by a standard linear regression model fitted to the time series at each grid point. For the comparison between the COSMO-CLM 50 km run and its driving model, ECHAM5, the purpose of the linear regression is to detect the annual and semi-annual cycle, as both extra-tropics and tropics are included in the East Asia domain. The diurnal cycle is excluded from the time series, as the data for this comparison is daily mean values.

$$X = X_{\mathrm{m}} + X_{\mathrm{lt}} + X_{\mathrm{ac}} + X_{\mathrm{sac}} + X'; \quad X' \sim \mathcal{N}(0,\ \sigma^2) \tag{1}$$

The indices m, lt, ac and sac stand for *mean*, *linear trend*, *annual cycle* and *semi-annual cycle*, respectively. X' represents the filtered time series, which will be analysed later. Both annual cycle and semi-annual cycle are described by two parameters: amplitude and phase shift of a sine signal at the annual and semi-annual frequencies. For most regions, σ^2 depends on the season, thus X' will be analysed conditioned on the season. In this analysis (ECHAM5 vs. COSMO-CLM 50 km), we consider the summer season, from April to September, and the winter season, from October to March, which results in about 180 data values per season and year.

For the comparison between the COSMO-CLM 7 km runs and its driving model, COSMO-CLM 50 km, hourly values are available. First, the summer season, from June to August (JJA), and the winter season, from December to February (DJF), were selected from the time series. The selected seasons differ in length compared to the seasons selected above due to computational aspects. Hourly values and seasons of three months in length result in about 2160 values per season and year. Second, to detect the diurnal cycle, a linear regression model has been fitted to each season individually:

$$X = X_{\mathrm{dc}} + X'; \quad X' \sim \mathcal{N}(0,\ \sigma^2) \tag{2}$$

Here, the *diurnal cycle* term X_{dc} consists of 24 parameters, one for each hour of the day. In Section 4, we will see that the relevant time scale, on which the driven RCM changes from transfer to generation of variability, is about 1 d. In order to avoid aliasing effects (Von Storch and Zwiers, 2002) from sampling high frequency signals at low rates, only temperatures at 2 m, which are available with hourly resolution, will be analysed for the step from 50 to 7 km resolution.

To examine this nature of co-variability between the driving model and the driven model over a continuum of frequencies, the cross-spectra

$$\Gamma_{xy}(\omega) = \mathcal{F}\left\{\gamma_{xy}\right\}(\omega) = A_{xy}(\omega)e^{i\Phi_{xy}(\omega)} \quad \forall\, \omega \in [-0.5, 0.5] \tag{3}$$

are estimated grid-point wise. Here, $\mathcal{F}$ denotes the Fourier transform, γ_{xy} stands for the cross-covariance function of the time series X and Y. On the right-hand side of eq. (3), the cross-spectrum is expressed in polar coordinates, where A_{xy} and Φ_{xy} are called amplitude spectrum and phase spectrum, respectively. However, the amplitude of the complex cross-spectrum Γ_{xy} will be represented as squared coherency spectrum,

$$\kappa_{xy}(\omega) = \frac{A^2_{xy}(\omega)}{\Gamma_{xx}(\omega)\Gamma_{yy}(\omega)} \tag{4}$$

Γ_{xx} and Γ_{yy} refer to the univariate spectra of the time series X and Y, respectively. The coherence is dimensionless and formally similar to the squared correlation. Thus, the coherence function can be seen as a linear transfer function of information from the driving model to the driven model (Jenkins and Watts, 1968). Due to the experiment setup, a phase lag of a climate signal occurring in both models is unexpected and the phase spectrum can be neglected.

Technically, the estimation of the cross-spectrum is based on bi-variate periodograms. As the pure bi-variate periodogram is not a good estimator for the cross-spectrum, smoothing techniques have to be applied (Jenkins and Watts, 1968; Von Storch and Zwiers, 2002). For the frequency 1/yr, a Daniell spectral estimator was used. For higher frequencies, the time series was split into blocks of the same length called chunks. The periodograms computed individually for each chunk are averaged afterwards in order to account for different variances σ^2 of the residual time series conditioned on the season. To keep the inference of both the Daniell spectral estimator and the chunk spectral estimator consistent, it was ensured that both estimators result in about the same degrees of freedom. Uncertainty of the estimation is assessed via 95% confidence intervals. For more details on the applied estimators, the reader is referred to Von Storch and Zwiers (2002).

4. Results

The results for the first nesting step, i.e. from ECHAM5 to COSMO-CLM 50 km, are presented first, followed by the comparison of COSMO-CLM 50 km and the double-nesting COSMO-CLM 7 km for the two catchments, Haihe and Poyang.

Appearing for all examined variables and frequencies is a red frame along the lateral boundaries (Fig. 3), where coherence is close to unity. This indicates a strong transfer of climate variability at the boundaries, which can be expected due to the experimental setup. The width of the red frame varies between the different variables, but is of the order of the width of the sponge zone, which is 10 grid boxes at each side in our setup.

For the variables T_2M, T850 and Q850, more variability in the spatial patterns of coherence at frequency 1/yr is found in the inner domain (Fig. 3a–c). The field for T_2M exhibits a pronounced land–sea contrast, with a strong transfer of variability over the ocean and a weak transfer over land (Fig. 3a). This is especially apparent for the tropics with its large islands and the Indochinese peninsula, but it is also visible in the extra-tropics at the coastlines of East China, Korea and southern Japan. Here, one should keep in mind that the sea surface temperature of ECHAM5 serves as a boundary condition and drives COSMO-CLM from the ocean. Exceptions to this general image are found in the higher latitudes of the domain, where for both land and sea a strong transfer of variability can be detected, and over the tropical ocean at 5°N to 10°N in the eastern part of the domain, where a local minimum of coherence is located (cf. Section 5).

To investigate the coherence spectrum at this local minimum over a range of frequencies, we averaged the 2 m temperature, over the box 4°N to 9°N and 132°E to 144°E, before calculating the spectrum (Fig. 4a). This procedure also cancels out fine-scale variability. The coherence is about 0.5 at 1/yr and decreases close to zero at 1/month. This result matches with the values presented in the maps. For completeness, the ratio between the univariate spectra of the two models is also computed (Fig. 4b). The ratio gives a measure of the absolute

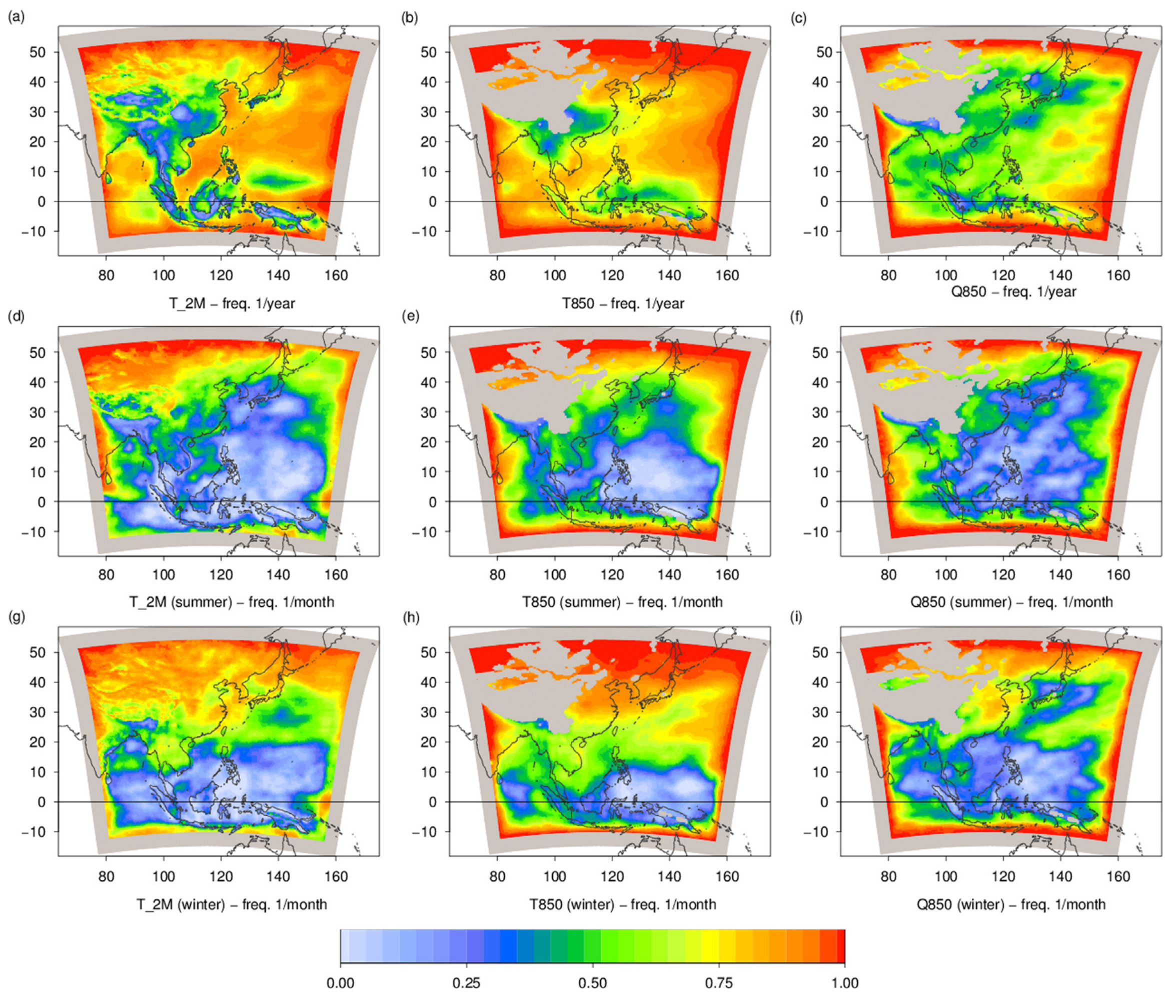

Fig. 3. Grid-point wise coherence between COSMO-CLM (0,44°resolution) driven by ECHAM5 20C3M_all run no.3 and ECHAM5 20C3M_all run no.3. The 1st, 2nd and 3rd columns show results for the variables T_2M, T850 and Q850, respectively. The 1st, 2nd and 3rd rows show results for the frequencies 1/yr, 1/month in summer and 1/month in winter, respectively. The grey frame indicates the sponge zone. The grey shaded areas within the domain cover mountainous regions, that lie above 850 hPa.

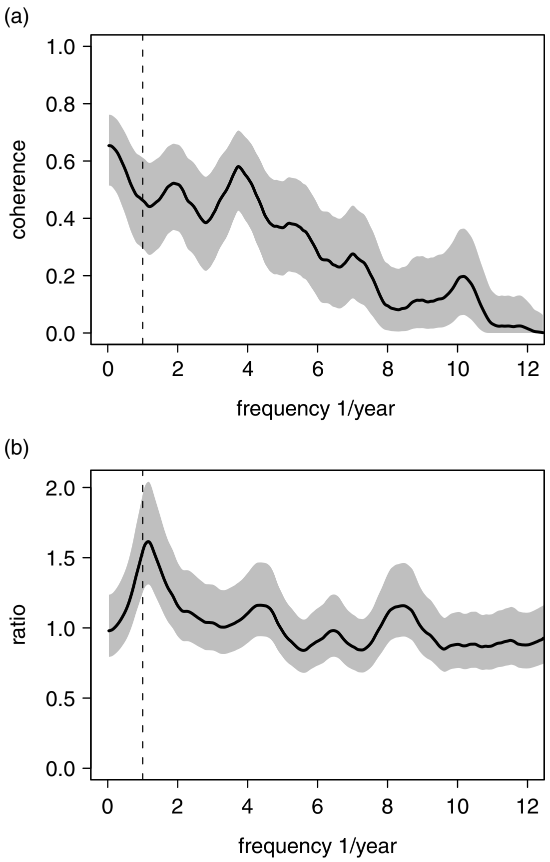

Fig. 4. Analysis of T_2M averaged over the box 4°N to 9°N and 132°E to 144°E. (a) Coherence between the time series from COSMO-CLM driven by ECHAM5 20C3M_all run no.3 and ECHAM5 20C3M_all run no.3. (b) The ratio between the corresponding univariate spectra.

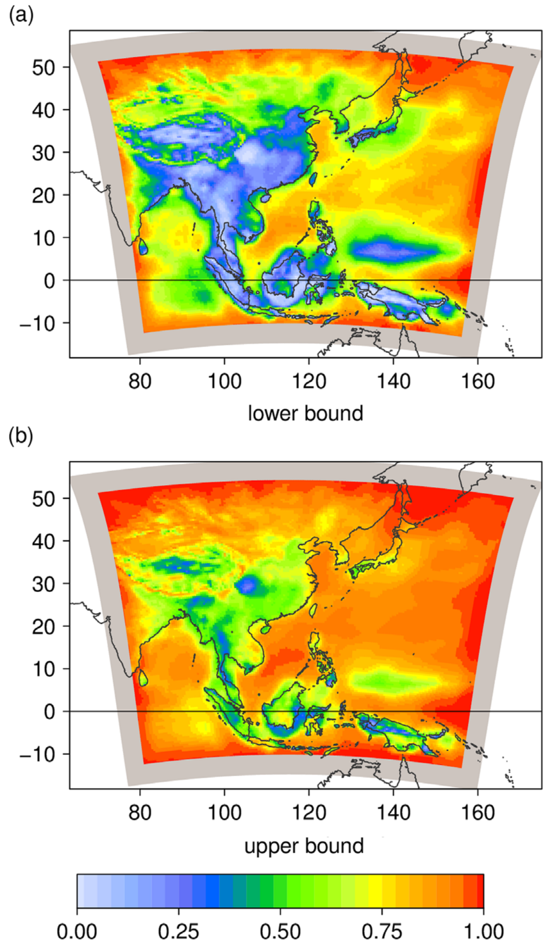

Fig. 5. 95% confidence interval for T_2M at the frequency 1/yr (Fig. 3a).

similarity. Though the variability of T_2M in COSMO-CLM is higher than in ECHAM5 at the frequency 1/yr, it is still in the same order.

To give an impression of the uncertainties coming along with the estimator, a closer look is taken at the 95% confidence interval for T_2M at the frequency 1/yr (Fig. 5). The most important feature is the local minimum around 10°N in the Pacific, which remains even in the upper bound of the confidence interval. In the lower bound, the degree of decoupling is pronounced over East South Asia and the area South of the equator in the Indic exhibits a local minimum with values around 0.5.

In the lower troposphere at 850 hPa, the temperature reveals a slightly different image (Fig. 3b). For most of the domain, a strong transfer of variability is obviously similar to T_2M, but the pronounced land–sea contrast over the tropics has weakened towards higher coherence values over the land. A possible explanation is the stronger dependence of T_2M on the parameterisation of land surface processes, which differs between ECHAM5 and COSMO-CLM and hence leads to low coherence between the models at 2 m. Another difference between the spatial pattern of T850 and T_2M is a shift of the local minimum over the tropical North Pacific further South closer to the equator. Both minima are connected vertically, which was checked with a cross-section at 135°E (figure not shown). Furthermore, compared to the pattern of T_2M, the transfer of variability over the Asian landmass is more enhanced. Only very close to the mountain range, where the temperature at 2 m coincides with the temperature at 850 hPa, low coherence values are found.

While variability of temperature at 850 hPa is strongly dictated by ECHAM5, the variability of specific humidity at 850 hPa is rather decoupled (Fig. 3c). Even the green areas ($\kappa_{xy}(1/year) = 0.5$) indicate that still 50% of the variance in the RCM can be explained by the driving GCM. However, this finding suggests a decoupling of the modelled water cycle.

In general, the results for the frequency 1/month (Fig. 3d–i) exhibit that the RCM is decoupled from its driving model in the inner domain with coherence values <0.25 for large areas of the domain. The extent of this 'inner domain' varies for the different variables and seasons. For summer (Fig. 3d–f), the areas, for which the driven and the driving model are decoupled from each other, reach further North than in winter (Fig. 3g–i); the Asian landmass is covered with coherence values >0.5 in winter, with the lower coherence for Q850 over the Indochinese peninsula being the only exception. Over the Bay of Bengal, both variables (temperature and humidity) at 850 hPa are influenced by the driving model stronger in summer (Fig. 3e,f) than in winter (Fig. 3h,i), which can be associated with the prevailing southwesterly trade winds in this region.

Similar to the results for the frequency 1/yr, there is a stronger coupling between ECHAM5 and COSMO-CLM for a temperature at 850 hPa than for humidity at the 1/month frequency. For Q850, coherence values less than 0.5 extend even to the northeastern part of the domain. In contrast, the decoupling for T850 is more concentrated on tropical regions, which is especially true for the winter (Fig. 3h).

Comparing T_2M and T850 exhibits similar patterns for the coherence values at the frequency 1/month. However, the influence of ECHAM5 on the temperature in COSMO-CLM is slightly stronger at 850 hPa than at the surface. This is remarkable, as the ECHAM5 SST serves as a boundary condition for the RCM runs. Parameterized processes at the surface might cause the strong decoupling between the surface temperatures in the models.

For the sake of completeness, the results of the cross-spectral analysis between COSMO-CLM driven by ECHAM5 under the A1B scenario reveal nearly the same spatial coherence pattern as under the 20C conditions (Fig. 3). All correlations between the 20C coherence pattern and the corresponding A1B pattern exceed 0.9. This circumstance should only be mentioned here as it makes the results for 20C more robust, but a presentation of the results for A1B in detail can be omitted.

Figure 6 shows an extract of the results gained from the comparison of the two 7-km domains (namely Haihe catchment and Poyang catchment) with their driving counterpart at the 1/48 h frequency. As discussed in the Methods section, only a temperature at 2 m is analysed. Similar to the first nesting step, coherence values for summer (JJA) are smaller than for winter (DJF). This finding indicates that convective-scale processes typical for summer are generated in the driven model independent from the processes passed by the 50-km driving model, which leads to a decoupling in the surface temperature. The reason for the decoupling might be found in the different applicability of the Tiedtke convection scheme on the different resolutions (Kuell et al., 2007). In contrast, the large-scale processes typical for winter lead to the transfer of variability in the surface temperature.

Comparing the coherence distribution in both domains with each other, we find smaller values for the Poyang catchment. We suppose that day-to-day variability in the Poyang basin is dominated strongly by monsoon dynamics, which is associated with higher variability in small-scale features, compared to the weather in the Haihe region (Wang, 2006; Simon et al., 2013). Although a similar dipole structure is already visible in the results of the first nesting step (Fig. 3d), the results in Fig. 3 cannot be directly compared with the results in Fig. 6. These findings are absolutely independent from each other, as no ECHAM5 information is integrated in the analysis of the second nesting steps. Another remarkable feature is the band of relatively low coherence values along the coastline in the Haihe domain for the JJA season (Fig. 6a), which is a direct effect of the change from low to high resolution and the attended better representation of the land–sea mask. In winter (DJF), where coherence is high for the whole domain, the minima lie in the mountainous regions. This is an effect of orography, which is represented more realistically in COSMO-CLM at higher resolution.

However, the fact that for the Poyang catchment coherence values less than 0.5 m at the frequency 1/48h were found for large parts of the domain is a sufficient condition for an expected added value of further analyses, such as the application of extreme value theory on weather extremes associated with a daily time scale (Katz et al., 2002; Friederichs, 2010). The strong transfer of variability for the winter months indicates that there is no potential to expect added value in terms of additional variability on high temporal frequencies. For completeness, it is tested for added value in terms of modification of the amplitude of the input signal. This is done via the ratio of the univariate spectra of both models (not shown). For our example, this aspect of added value could be detected at some isolated spots. Furthermore, our methods provide no sufficient condition to reject the potential of the RCM to generate more variability on high spatial frequencies, which can be assessed by the method presented by Errico (1985).

5. Discussion

In this section, two key aspects will be addressed. On the one hand, we suggest an explanation for the local minimum of coherence in the T_2M field for the frequency 1/yr over the tropical North Pacific. On the other hand, we discuss transfer and generation of climate variability in RCMs in general.

In order to investigate the local minimum in Fig. 3a, we take a closer look at the precipitation distribution

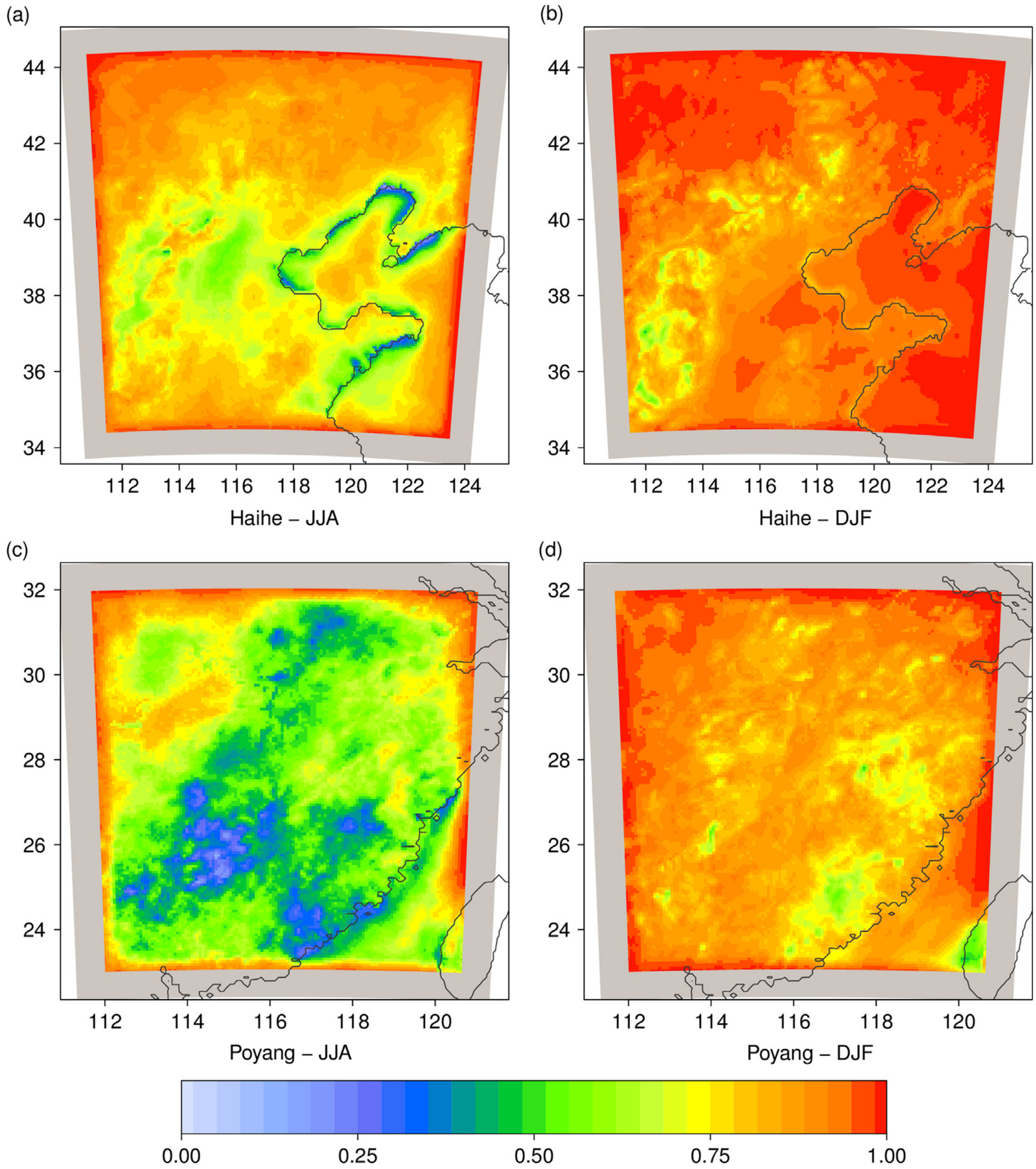

Fig. 6. Grid-point wise coherence at frequency 1/48h between COSMO-CLM (0,0625°resolution) driven by COSMO-CLM '20C' (0,44°resolution) and COSMO-CLM '20C' (0,44°resolution). The 1st and 2nd columns show the results for COSMO-CLM (0,0625°) adapted to the Haihe catchment and the Poyang catchment, respectively. The 1st and 2nd rows show the results for summer season (JJA) and winter season (DJF), respectively. The grey frame indicates the sponge zone.

generated by COSMO-CLM and ECHAM5, which is closely related to the dynamics of the inter-tropical convergence zone (ITCZ) (Fig. 7). In this region, with its dominant easterly trade winds, ECHAM5 directly feeds COSMO-CLM. A typical feature of ECHAM5 in the tropical Pacific is the so-called double ITCZ, which is a well-known phenomenon in most coupled GCMs (Li et al., 2004). This leads to a northern ITCZ, broadened and shifted further North compared to observations that persist throughout the year (Jungclaus et al., 2006). In the precipitation field of ECHAM5 (Fig. 7b), the northern ITCZ is clearly visible as a strong rain belt around 10°N in the Pacific.

When this strong precipitation belt enters the RCM domain, it has to get adapted to the new grid. The ECHAM5 ITCZ transports a huge amount of moisture into the COSMO-CLM domain. The major part of this humid air accumulates close to the boundary, where mean annual precipitation up to 7000 mm/year is simulated. This is a strong positive wet bias compared to the mean annual

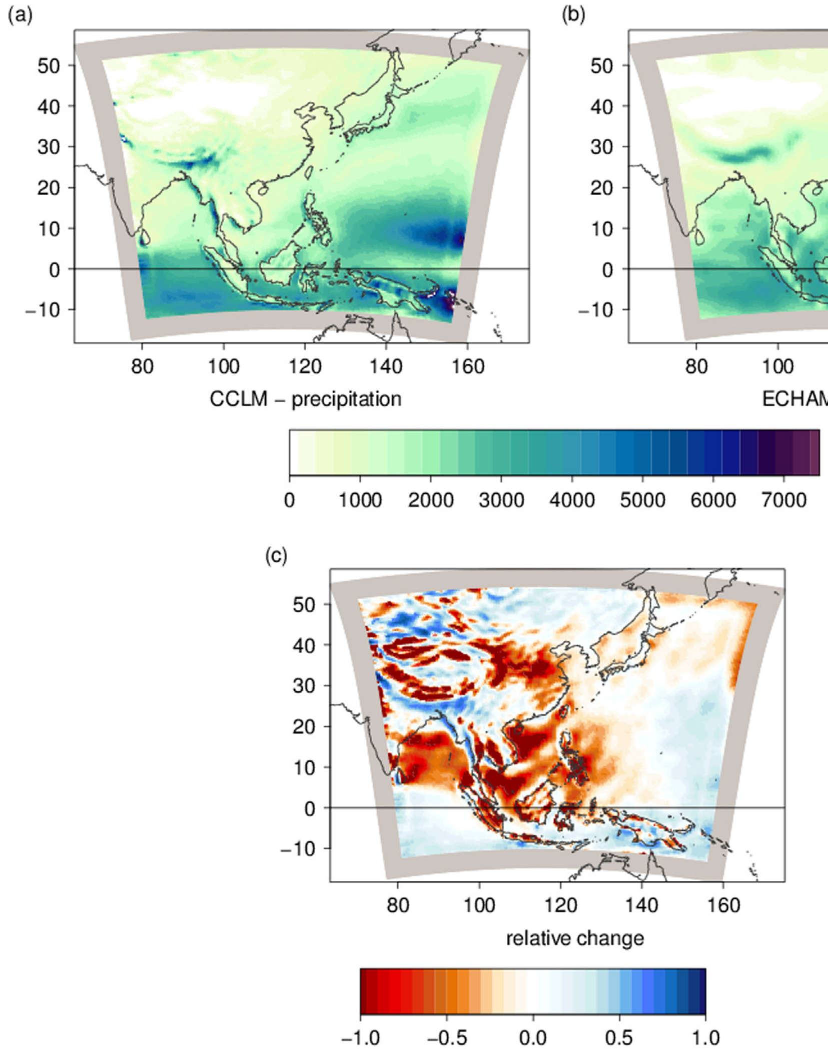

Fig. 7. Comparison of mean annual precipitation from COSMO-CLM and ECHAM5 for the period from 1971 to 2000 in *mm*. The field of ECHAM5 is bi-linearly interpolated to the COSMO-CLM grid and the sponge frame is added for better visual orientation. The right-hand plot shows the relative change between COSMO-CLM values and ECHAM5 values, with the darkest red indicating a relative change of −100% or less.

precipitation in ECHAM5. About 95% of the simulated precipitation in COSMO-CLM in this region is related to convective processes, which depend on the applied parameterisations. Following the ITCZ in COSMO-CLM to the East the mean annual precipitation values decrease. The sign of the bias changes at about 140°E and close to the Philippines the bias reaches strong negative values. This finding indicates a strong dissonance between the convection schemes of the two models. In turn, this could cause the decoupling ($\kappa_{xy}(1/year) \sim 0.5$) of the variability of the 2 m temperature in COSMO-CLM and the variability of 2 m temperature in ECHAM5. Further parameter tuning, e.g. adjustment of the Rayleigh sponge damping layer (Wang et al., 2013), could help to reduce this dissonance.

We now enter the discussion about transfer and generation of climate variability in RCMs in general. To this end, we review the results of a second experimental setup and examine the coherence spectra between COSMO-CLM driven by ERA-40 and ERA-40 itself (Fig. 8). The applied LBC differ from the ones of the ECHAM5 driven experiment, which helps to gain information about the influence of the LBC versus the potential of the RCM to develop an independent inner domain. The spatial resolution of ERA-40 is higher than the spatial resolution of ECHAM5, which leads potentially to more fine-scale variability that is directly passed into the regional model.

The results based on ERA-40 (Fig. 8) are similar to the ones based on ECHAM5 (Fig. 3) with respect to the high coherence values near the boundaries and on the landmass

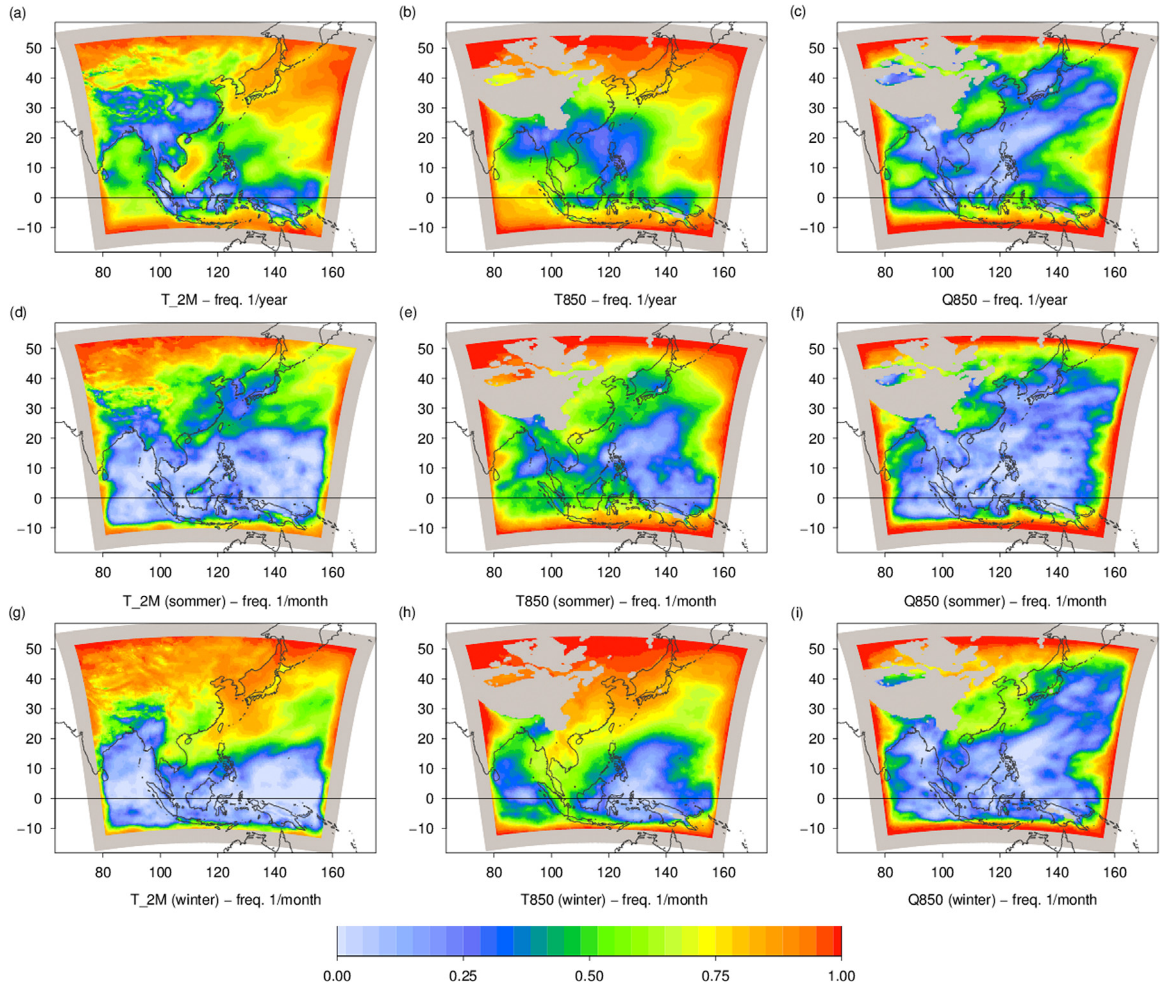

Fig. 8. Grid-point wise coherence between COSMO-CLM (0,44 °resolution) driven by ERA-40 and ERA-40. The 1st, 2nd and 3rd columns show results for the variables T_2M, T850 and Q850, respectively. The 1st, 2nd and 3rd rows show results for the frequencies 1/yr, 1/month in summer and 1/month in winter, respectively. The grey frame indicates the sponge zone. The grey shaded areas within the domain cover the mountainous regions that lie above 850 hPa and contain only artificial results for T850 and Q850.

in the North and low values in the inner domain, particularly in the tropics. Strong similarities prevail for the frequency 1/month, which leads to the conclusion that the patterns for transfer and generation of variability on this frequency are mainly based on the model itself, COSMO-CLM. Stronger differences can be seen at the frequency 1/yr with a distinct feature related to the ITCZ in the eastern part of the tropics (Fig. 8a). In contrast to ECHAM5, there is no persistent double ITCZ in ERA-40 and accordingly the associated LBC differ strongly from each other. Another remarkable feature is the decoupling of the water cycle (i.e. Q850, Fig. 8c) between COSMO-CLM driven by ERA-40 and ERA-40, which is even more pronounced compared to the ECHAM5 case (Fig. 3). There are different possible explanations for this finding. On the one hand, this finding might be related to the fact that intrinsic model noise is abandoned in ERA-40 and replaced by observational noise. On the other hand, one could also expect such a difference if the physical parameterisations (e.g. boundary layer, shallow convection, etc.) that affect Q850 differ more between ERA40 and COSMO-CLM than between ECHAM5 and COSMO-CLM.

The experiment with LBC from ERA-40 reveals that a dynamical downscaling driven by re-analysis data is conceptually different to a regional re-analysis, which would include data assimilation on the regional scale. The results (Fig. 8) show that COSMO-CLM generated variability in the inner domain by itself. Within a regional re-analysis framework, this freely developing variability would be suppressed by the data assimilation.

Finally, although the significance of the presence of self-generated climate variability cannot be assessed quantitatively due to the lack of appropriate test statistics (cf. Section 3), a qualitative statement can be made. Looking at an example of a coherence spectrum for one grid cell (Fig. 9), it is obvious that a decay of coherence takes place over a broad band of frequencies rather than a sharp drop.

6. Conceptual model

In this section, we are formulating an approach to assess the analysed aspect of added value theoretically.

The purpose of this method is to find the frequency band on which the RCM simulations copy the internal variability of the driving model and on which the RCM potentially generates internal variability on its own. The first and the latter frequency bands refer to slow and fast variations in the time series, respectively. Conceptually, one can imagine a decomposition as follows:

$$X'_{\text{driving}} = X'_{\text{sv}} + X'_{\text{n}} \tag{5}$$

$$Y'_{\text{driven}} = Y'_{\text{av}} + Y'_{\text{sgv}} + Y'_{\text{n}}, \tag{6}$$

with the following indices: the driving model (driving), slow varying variability (sv), noise (n), the driven model (driven), adapted variability (av), self-generated variability (sgv). This conceptual model allows us to interpret the co-variability between X_{driving} and Y_{driven},

$$\begin{aligned} E(X'_{\text{driving}} Y'_{\text{driven}}) = {} & E(X'_{\text{sv}} Y'_{\text{av}}) + E(X'_{\text{n}} Y'_{\text{sgv}}) \\ & + E(X'_{\text{sv}} Y'_{\text{n}}) + E(X'_{\text{n}} Y'_{\text{av}}) \\ & + E(X'_{\text{sv}} Y'_{\text{sgv}}) + E(X'_{\text{n}} Y'_{\text{n}}), \end{aligned} \tag{7}$$

as a function of the time scale. A high correlation can only be expected between X_{gv} and Y_{av} All terms, in which noise is taken into account, the correlation equals zero by definition. One should keep in mind that X_{gv} and Y_{av} are not necessarily truncated at the same frequency, but there might also be a band of frequencies, which is populated by both X_{gv} and Y_{sgv} Therefore, the correlation between X_{gv} and Y_{sgv} is not necessarily zero, but rather is expected to show a decay for the correlation towards shorter time scales.

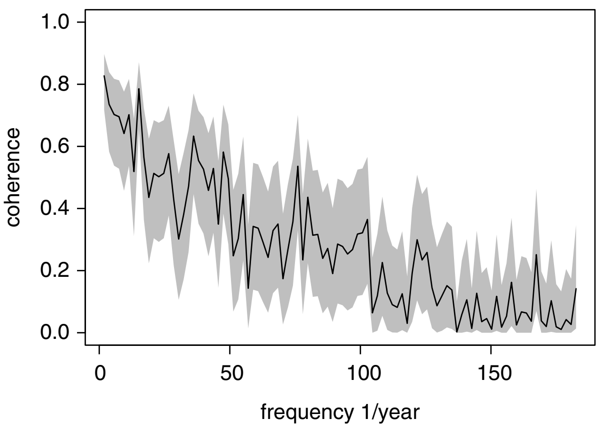

Fig. 9. A exemplary coherence spectrum for one grid cell in the Pacific (140°E, 20°N) for T850 in winter taken from the '20C' experiment. The grey shaded area indicates the 95% confidence interval.

Within this framework, it can be considered how a proper hypothesis testing for the above analysis could be designed. Usually a coherence value has to be tested against $H_0{:}\kappa_{xy} = 0$. Considering our conceptual model [eqs. (5) and (6)], this type of test is not appropriate for our problem. The question to be answered would be whether the self-generated internal variability of the driven model is greater than zero $H_1{:}E({Y'_{sgv}}^2) > 0$. Formally, this means to test $H_0{:}E({Y'_{\text{sgv}}}^2) = 0$, which cannot be easily assessed.

7. Conclusions

This study introduces a method defining one aspect of added value in terms of ability of the regional model to generate variability on its own. With this technique, it is possible to analyse the temporal scales on which internal variability is generated by the RCM itself and on which variability is dictated by the driving model (a GCM in most cases). This method does not account for added value in term of a modification of the amplitude of the input signal, which can be tested by the ratio of the univariate spectra of the two models. Though not applied in this study, coherence spectra might also be used in studies dealing with added value on spatial scales.

An example – COSMO-CLM East Asia – illustrates the problems that can be assessed with this method. Self-generated variability was found in the 50-km RCM already on temporal frequencies between 1/yr and 1/month. In a second nesting step, i.e. from 50 to 7 km, variability in the driven model was dictated by the driving model even up to a day-to-day scale. That is a vast difference of temporal scales between the two nesting steps. The method was also applied to COSMO-CLM driven by the re-analysis ERA-40. The circumstances that the method reveals self-generated variability in the RCM output make clear that this simulation is conceptually different to a regional re-analysis, in which a data assimilation scheme is implemented (e.g. Mesinger et al., 2006).

A straightforward benefit of this method is that it gives insights in the usability of RCM output for further studies, e.g. the representation of extreme events (e.g. Katz et al., 2002; Friederichs, 2010), statistical downscaling (e.g. Benestad, 2004; Simon et al., 2013). Questions concerning the influence of numerical parameters on RCM performance arising from this study include:

- the sensitivity of the temporal scale between adapted and self-generated climate variability to the choice of domain size

- the role of the chosen RCM, i.e. is there a certain setup supporting the ability of the RCM to generate variability by its own
- the effect of differences in the LBC, which inserts systematic errors from the driving model
- the influence of a dynamical ocean component or a conceptual model like a slab ocean compared to a prescribed SST.

All of these questions are beyond the scope of this study, but can probably be assessed by applying the method or an extension of the method on multi-RCM ensembles, which are available, e.g. for Europe (EURO-CORDEX, see Vautard et al., 2013) and Africa (CORDEX-Africa, see Nikulin et al., 2012) and North America (NARCCAP, see Mearns et al., 2012).

8. Acknowledgements

The authors gratefully acknowledge two anonymous reviewers for their comments. This work was funded by the NSFC/DFG-joint funding programme *Land Use and Water Resources Management under Changing Environmental Conditions*. It was also carried out in the Hans Ertel Centre for Weather Research, a research network of Universities, Research Institutes and the Deutscher Wetterdienst funded by the BMVBS (Federal Ministry of Transport, Building and Urban Development). Furthermore, the authors would like to thank Christoph Menz from BMBF's *Guanting Project* for the smooth and straightforward supply of data. The authors would like to credit the contributors to the *R project*.

References

Benestad, R. 2004. Empirical–statistical downscaling in climate modeling. *Eos*. **85**(42), 417.

Bierdel, L., Friederichs, P. and Bentzien, S. 2012. Spatial kinetic energy spectra in the convection-permitting limited-area NWP model COSMO-DE. *Meteorol Z*. **21**, 245–258.

Castro, C. L., Pielke, R. A. and Leoncini, G. 2005. Dynamical downscaling: assessment of value retained and added using the regional atmospheric modeling system (RAMS). *J. Geophys. Res*. **110**(D05108). DOI: 10.1029/2004JD004721.

Denis, B., Laprise, R., Caya, D. and Cote, J. 2002. Downscaling ability of one-way nested regional climate models: the Big-Brother Experiment. *Clim. Dynam*. **18**(8), 627–646.

Di Luca, A., de Elía, R. and Laprise, R. 2012. Potential for added value in precipitation simulated by high-resolution nested regional climate models and observations. *Clim. Dynam*. **38**(5), 1229–1247.

Ding, Y. and Chan, J. 2005. The East Asian summer monsoon: an overview. *Meteorol. Atmos. Phys*. **89**(1), 117–142.

Dommenget, D. 2010. The slab ocean el niño. *Geophys. Res. Lett*. **37**(20), L20701.

Easterling, D. R., Meehl, G. A., Parmesan, C., Changnon, S. A., Karl, T. R. and et al. 2000. Climate extremes: observations, modeling, and impacts. *Science*. **289**(5487), 2068–2074.

Errico, R. M. 1985. Spectra computed from a limited area grid. *Mon. Weather Rev*. **113**(9), 1554–1562.

Feser, F. 2006. Enhanced detectability of added value in limited-area model results separated into different spatial scales. *Mon. Weather Rev*. **134**(8), 2180–2190.

Feser, F., Rockel, B., von Storch, H., Winterfeldt, J. and Zahn, M. 2011. Regional climate models add value to global model data. *B. Am. Meteorol. Soc*. **92**, 1181–1192.

Feser, F. and von Storch, H. 2008. A dynamical downscaling case study for typhoons in southeast Asia using a regional climate model. *Mon. Weather Rev*. **136**(5), 1806–1815.

Frei, C., Schöll, R., Fukutome, S., Schmidli, J. and Vidale, P. 2006. Future change of precipitation extremes in Europe: intercomparison of scenarios from regional climate models. *J. Geophys. Res*. **111**(D6), D06105.

Friederichs, P. 2010. Statistical downscaling of extreme precipitation events using extreme value theory. *Extremes*. **13**(2), 109–132.

Gao, X., Shi, Y., Song, R., Giorgi, F., Wang, Y. and Zhang, D. 2008. Reduction of future monsoon precipitation over china: comparison between a high resolution RCM simulation and the driving GCM. *Meteorol. Atmos. Phys*. **100**(1), 73–86.

Giorgi, F., Christensen, J., Hulme, M., Von Storch, H., Whetton, P. and co-authors. 2001. Regional climate information–evaluation and projections. *Climate Change 2001: The Scientific Basis* (eds. J. T. Houghton, et al.). Cambridge University Press, Cambridge, pp. 583–638.

Giorgi, F., Jones, C., Asrar, G. R. and co-authors. 2009. Addressing climate information needs at the regional level: the Cordex framework. *World Meteorological Organization (WMO) Bulletin* **58**(3), 175.

Hagedorn, R., Lehmann, A. and Jacob, D. 2000. A coupled high resolution atmosphere–ocean model for the Baltex region. *Meteorol. Z*. **9**(1), 7–20.

Jenkins, G. M. and Watts, D. G. 1968. *Spectral Analysis and Its Applications*. Holden-Day, San Francisco.

Jungclaus, J., Keenlyside, N., Botzet, M., Haak, H., Luo, J.-J. and co-authors. 2006. Ocean circulation and tropical variability in the coupled model echam5/mpi-om. *J. Climate*. **19**(16), 3952–3972.

Katz, R. W., Parlange, M. B. and Naveau, P. 2002. Statistics of extremes in hydrology. *Adv. Water Resour*. **25**(8), 1287–1304.

Kuell, V., Gassmann, A. and Bott, A. 2007. Towards a new hybrid cumulus parametrization scheme for use in non-hydrostatic weather prediction models. *Q. J. Roy. Meteor. Soc*. **133**(623), 479–490.

Kuemmerlen, M., Domisch, S., Schmalz, B., Cai, Q., Fohrer, N. and co-authors. 2012. Integrierte modellierung von aquatischen ökosystemen in china: Arealbestimmung von makrozoobenthos auf einzugsgebietsebene [Integrated modelling of aquatic ecosystems in China: Distribution of benthic macroinvertebrates at catchment scale]. *Hydrol. Wasserbewirts*. **56**(4), 185–192.

Laprise, R., De Elia, R., Caya, D., Biner, S., Lucas-Picher, P. and co-authors. 2008. Challenging some tenets of regional climate modelling. *Meteorol. Atmos. Phys*. **100**(1), 3–22.

Laprise, R., Kornic, D., Rapaić, M., Šeparović, L., Leduc, M. and co-authors. 2012. Considerations of domain size and large-scale driving for nested regional climate models: impact on internal variability and ability at developing small-scale details. *Climate Change* (eds. A. Berger et al.). Springer, Wien. pp. 181–199.

Li, J., Zhang, X., Yu, Y. and Dai, F. 2004. Primary reasoning behind the double itcz phenomenon in a coupled ocean–atmosphere general circulation model. *Adv. Atmos. Sci.* **21**(6), 857–867.

Lorbacher, K., Dommenget, D., Niiler, P. and Köhl, A. 2006. Ocean mixed layer depth: a subsurface proxy of ocean–atmosphere variability. *J. Geophys. Res.* **111**(C7), C07010.

Mearns, L. O., Arritt, R., Biner, S., Bukovsky, M. S., McGinnis, S. and co-authors. 2012. The North American regional climate change assessment program: overview of phase I results. *B. Am. Meteorol. Soc.* **93**(9), 1337–1362.

Mesinger, F., DiMego, G., Kalnay, E., Mitchell, K., Shafran, P. C. and co-authors. 2006. North American regional reanalysis. *B. Am. Meteorol. Soc.* **87**(3), 343–360.

Nakicenovic, N., Alcamo, J., Davis, G., de Vries, B., Fenhann, J. and co-authors. 2000. *Special Report on Emissions Scenarios: A Special Report of Working Group III of the Intergovernmental Panel on Climate Change*. Technical Report, Pacific Northwest National Laboratory, Richland, WA (US), Environmental Molecular Sciences Laboratory (US).

Nikulin, G., Jones, C., Giorgi, F., Asrar, G., Büchner, M. and co-authors. 2012. Precipitation climatology in an ensemble of Cordex-Africa regional climate simulations. *J. Climate*. **25**(18), 6057–6078.

Orlanski, I. 1975. A rational subdivision of scales for atmospheric processes. *B. Am. Meteorol. Soc.* **56**, 527–530.

Rockel, B., Castro, C. L., Pielke Sr, R. A., von Storch, H. and Leoncini, G. 2008a. Dynamical downscaling: assessment of model system dependent retained and added variability for two different regional climate models. *J. Geophys. Res.* **113**(D21), D21107.

Rockel, B., Will, A. and Hense, A. 2008b. The regional climate model COSMO-CLM (CCLM). *Meteorol. Z.* **17**(4), 347–348.

Roeckner, E. 2005. IPCC MPI-ECHAM5_T63L31 MPI-OM_GR1.5L40 20C3M_all run no.3: atmosphere 6 HOUR values MPImet/MaD Germany. CERA-DB "EH5-T63L31_OM_20C3M_3_6H" http://cera-www.dkrz.de/WDCC/ui/Compact.jsp?acronym=EH5-T63L31_OM_20C3M_3_6H.

Roeckner, E., Bäuml, G., Bonventura, L., Brokopf, R., Esch, M. and co-authors. 2003. *The Atmospheric General Circulation Model ECHAM5. Part I: Model Description, Report 349*. Max Planck Institute for Meteorology, Hamburg, Germany.

Röpnack, A., Hense, A., Gebhardt, C. and Majewski, D. 2013. Bayesian model verification of NWP ensemble forecasts. *Mon. Weather Rev.* **141**(1), 375–387.

Rummukainen, M. 2009. State-of-the-art with regional climate models. *WIREs: Clim. Change*. **1**(1), 82–96.

Schmalz, B., Kuemmerlen, M., Strehmel, A., Song, S., Cai, Q. and co-authors. 2012. Integrierte modellierung von aquatischen ökosystemen in china: Ökohydrologie und hydraulik [Integrated modelling of aquatic ecosystems in China: Ecohydrology and hydraulics]. *Hydrol. Wasserbewirts.* **56**(4), 169–184.

Simon, T., Hense, A., Su, B., Jiang, T., Simmer, C. and co-authors. 2013. Pattern-based statistical downscaling of East Asian Summer Monsoon precipitation. *Tellus A*. **65**. http://dx.doi.org/10.3402/tellusa.v65i0.19749.

Skamarock, W. 2004. Evaluating mesoscale nwp models using kinetic energy spectra. *Mon. Weather Rev.* **132**(12), 3019–3032.

Uppala, S., Kållberg, P., Simmons, A., Andrae, U., Bechtold, V. and co-authors. 2005. The ERA-40 re-analysis. *Q. J. Roy. Meteor. Soc.* **131**(612), 2961–3012.

Vautard, R., Gobiet, A., Jacob, D., Belda, M., Colette, A. and co-authors. 2013. The simulation of European heat waves from an ensemble of regional climate models within the Euro-Cordex project. *Clim. Dynam.* **41**, 2555–2575.

von Storch, H., Langenberg, H. and Feser, F. 2000. A spectral nudging technique for dynamical downscaling purposes. *Mon. Weather Rev.* **128**(10), 3664–3673.

Von Storch, H. and Zwiers, F. 2002. *Statistical Analysis in Climate Research*. Cambridge University Press, Cambridge, UK.

Wackernagel, H. 2010. *Multivariate Geostatistics*. Springer, Berlin.

Wang, B. 2006. *The Asian Monsoon*. Springer Verlag, Berlin.

Wang, B., Ding, Q., Fu, X., Kang, I., Jin, K. and co-authors. 2005. Fundamental challenge in simulation and prediction of summer monsoon rainfall. *Geophys. Res. Lett.* **32**(15), L15711.

Wang, D., Menz, C., Simon, T., Simmer, C. and Ohlwein, C. 2013. Regional dynamical downscaling with CCLM over East Asia. *Meteorol. Atmos. Phys.* **121**, 39–53.

Winterfeldt, J. and Weisse, R. 2009. Assessment of value added for surface marine wind speed obtained from two regional climate models. *Mon. Weather Rev.* **137**(9), 2955–2965.

Appendix C

Pattern-based statistical downscaling of EASM precipitation

The following manuscript has been published in the peer-reviewed journal *Tellus A* in 2013.

Attribution of roles

Thorsten Simon, Tong Jiang, Clemens Simmer and Christian Ohlwein defined the scientific question behind the study. Thorsten Simon performed the analysis. Andreas Hense contributed to the development of the statistical methods. Buda Su and Jiang Tong provided the observational data and were in charge of its quality. All authors discussed the results and commented on the manuscript.

Tellus SERIES A DYNAMIC METEOROLOGY AND OCEANOGRAPHY
PUBLISHED BY THE INTERNATIONAL METEOROLOGICAL INSTITUTE IN STOCKHOLM

Pattern-based statistical downscaling of East Asian Summer Monsoon precipitation

By THORSTEN SIMON[1]*, ANDREAS HENSE[1], BUDA SU[2], TONG JIANG[2], CLEMENS SIMMER[1] and CHRISTIAN OHLWEIN[1], [1]*Meteorological Institute, University Bonn, Germany*; [2]*National Climate Centre (NCC), Beijing, China*

(Manuscript received 20 September 2012; in final form 24 January 2013)

ABSTRACT

This study identifies daily Meiyu-like East Asian Summer Monsoon patterns that are linked to precipitation observations in the Poyang lake catchment. This analysis provides insight into the dynamics of strong, local precipitation events and has the potential to improve projections of precipitation from coarse-grid numerical simulations. Precipitation observations between 1960 and 1999 are taken from 13 rain gauges located in the Poyang lake catchment, which is a sub-catchment of the Yangtze River. The analysis shows that the observations are linked to daily patterns of relative vorticity at 850 hPa (Vo850) and vertical velocity at 500 hPa (W500) taken from the ERA-40 re-analysis data set. The patterns are derived by two approaches: (a) empirical orthogonal function (EOF) analysis and (b) rotated EOF analysis. Vo850 and W500 refer to geostrophic and ageostrophic processes, respectively. A logistic regression connects the large-scale dynamics to the local observations, whereby a forward regression selects the patterns best suited as predictors for the probability of exceeding thresholds of 24 h accumulated rainfall at the gauges. The regression model is verified by cross-validation.

The spatial structure of the detected patterns can be interpreted in terms of well-known meso-α-scale disturbances called Southwest vortices. Overall, the proposed EOF and rotated EOF patterns are both related to physical processes and have the potential to work as predictors for exceedance rates of local precipitation in the Poyang catchment.

Keywords: Poyang catchment, Meiyu belt, East Asian Summer Monsoon, downscaling, precipitation, logistic regression, EOF

1. Introduction

In summertime, the East Asian Summer Monsoon (EASM) dominates climate and weather over the Yangtze Basin, China. The so-called Meiyu rain belt – typically occurring between early June and mid-July – stretches across the Yangtze valley and extends east to the southern parts of Korea and Japan. The Meiyu over the Yangtze is the same atmospheric phenomenon as the Baiu in Southern Korea and the Changma in Southern Japan (Wang, 2006).

The heavy rain events caused by the EASM and their strong variability have a high impact on water resource management, agriculture, and land use planning (Piao et al., 2010; Zhang et al., 2012), play an important role in the reinsurance industry and emergency management (Zong and Chen, 2000; Zhai et al., 2005; Kron, 2009), and even affect air quality over China (Zhao et al., 2010a). This makes the EASM a key factor influencing economic development in the region. Therefore, it is crucial to improve our knowledge about processes behind the EASM and its relation with heavy precipitation events.

Existing EASM indices can be clustered into 4–5 classes depending on definition and physical basis (Wang et al., 2008). The processes reflected by these indices are mainly the thermal contrast between the landmass and the adjacent seas (Guo, 1983; Webster and Yang, 1992) and the strength of the subtropical high-pressure system over the western North Pacific (Wang and Fan, 1999; Li and Zeng, 2002). However, all of these indices are defined on the seasonal scale and are thus less suited to reflect monsoon dynamics on the daily scale. Zhao et al. (2010b) present a daily scale index based on the difference between sea level pressure (SLP) anomalies of two boxes, with one box located over the East China Sea and one over China.

*Corresponding author.
email: tsimon@uni-bonn.de

Citation: Tellus A 2013, **65**, 19749, http://dx.doi.org/10.3402/tellusa.v65i0.19749

The Meiyu rain belt is associated with a quasi-stationary subtropical front separating the warm and moist air located over the tropical Southern Chinese Sea (SCS) from the cold and dry air formed over the mid-latitude landmass (Ding and Chan, 2005; Wang, 2006). This large-scale synoptic system is further characterized by low-level vortices, which are generated locally over the Tibetan plateau, and mainly visible on the 850 and 700 hPa pressure levels. Vortices that originate over the southeastern part of the plateau are called southwest vortices (SWVs) as they build up in the southwest of China (Ding and Chan, 2005).

SWV genesis can be described conceptually as follows. In spring and even more so in summer, the plateau receives strong solar radiation leading to strong convective instability given sufficient moisture supply. A mesoscale cyclonic circulation can develop, which supports convection (Wang, 2006). Additionally, baroclinic instability might instigate the generation of SWVs. The front between the warm and moist air from the south – or more precisely from the Indochinese peninsula and the SCS – and the cold and dry air from the mid-latitudes preconditions the development of SWVs (Chen and Dell'Osso, 1984). SWVs may take different tracks through China and the adjacent seas. Most SWVs move eastward and can cause heavy rainfall in the Yangtze Basin. Others might take a more northward path and can cause severe rainfall in northern China (Ding et al., 2001).

SWVs have been investigated many times over the last three decades. Comprehensive overviews on SWVs can be found in Wang (2006) and Chang (2004). Several studies focus on the analysis of SWVs during strong rainfall periods. The following model-based analyses of SWV events are of particular relevance: the formation and propagation of a SVW in July 1979 (Wang and Orlanski, 1987), the atmospheric processes during the Sichuan flood in July 1981 (Kuo et al., 1988), and the onset of the EASM in May 1992 (Chang et al., 2000). The latter study also investigates the role of orography and highlights its importance for vortex genesis and pathway (Chang et al., 2000). Tao and Ding (1981) analysed observed heavy rainfall events during 1931 and 1980 and the relevance of the Tibetan plateau for the associated atmospheric processes. During the GAME/HUBEX field experiment – an intensive hydrological and meteorological observation project taking place over eastern China in 1998 and 1999 – strong rainfall occurred over the Yangtze valley, which could be directly linked to SWVs (Ding et al., 2001).

In order to quantify the relationship between daily local precipitation and regional monsoon dynamics in a probabilistic context, a statistical downscaling framework was developed. To this end, we post-process the GCM dynamics for the following reasons: A grid box of a global GCM output represents an area of more than 40 000 km^2 (Roeckner, 2003; Uppala et al., 2005). Studies investigating the energy spectra within numerical weather prediction (NWP) models found an effective resolution of 4–7 grid boxes (Skamarock, 2004; Bierdel et al., 2012). It is reasonable to consider a similar effective resolution for GCMs used for climate scenarios or re-analyses. Unresolved subgrid processes like precipitation have to be parameterised often leading to systematic biases (Murphy, 1999; Wilby and Wigley, 2000). The uncertainty of GCM output is only assessable at high computational costs by ensembles (Schölzel and Hense, 2011). Furthermore, due to the horizontal resolution, local extreme events are only weakly depicted in GCM output.

To overcome some of these problems, many studies choose a dynamical downscaling approach via regional climate models (RCMs) (Frei et al., 2006; Gao et al., 2008; Park et al., 2008). RCMs are able to simulate dynamics on a finer scale, and come up with many benefits; for example, RCMs are physically motivated and provide a physically consistent dataset with cross-correlations between the different atmospheric variables. Nevertheless, new disadvantages come up with this approach. A new error source is introduced by the different ways boundary conditions are handled (Ebell et al., 2008; Mesinger and Veljovic, 2013) and sets of parameterisations are selected (Bachner et al., 2008). In particular, precipitation can show significant biases (Lindau and Simmer, 2013). Due to the high computational costs, RCMs are integrated usually with a one-way-nesting approach. Therefore, teleconnections are suppressed (Wang et al., 2005). In the case of the EASM, relevant processes cannot take place, for example, the interaction between the Meiyu rainbelt and the SST of the adjacent seas (Wang et al., 2005) or the coupling with ENSO (Wang et al., 2000).

Statistical downscaling is an alternative way to overcome some of the above-mentioned drawbacks of GCMs. The outcome is unbiased as the statistics are trained on observations. Depending on the target quantity an exceedance rate model (Zhai et al., 2005), a model for quantiles (Bremnes, 2004; Friederichs and Hense, 2007) or a description of the full probability density function (PDF) (Benestad et al., 2012) can be realised. Downscaling can improve the representation of extremes, especially when extreme value theory is applied (Bentzien and Friederichs, 2012). Statistical downscaling circumvents the low resolutions of GCMs, as the statistics are adapted to local measurements. By using amplitudes of spatial patterns instead of time series of single grid boxes as predictors, the downscaling approach can accommodate non-local influences in space and time. Such approaches are thus termed dynamical-statistical methods (Benestad, 2004; Maraun et al., 2010).

Besides regression techniques, other methods can be applied to estimate local PDFs of precipitation. Orlowsky et al. (2010) applied an analogue resampling scheme to observations from the Yangtze valley. Cooley et al. (2007) used a Bayesian hierarchical model to assess high precipitation return levels, which can also be used for downscaling. Stochastic weather generator techniques are also very popular in the field of statistical downscaling (Wilby et al., 1998; Vrac and Naveau, 2007).

In this paper, a statistical downscaling model is proposed, which predicts the probability of exceeding local precipitation thresholds. As covariates we test spatial patterns associated with the monsoon dynamics on a daily scale. Both observational data from rain gauges in the Poyang catchment and re-analysis data (cf. Section 2) are used for the derivation of the predictors and the setup of the statistical model (cf. Section 3). The results of the downscaling approach (cf. Section 4) are discussed in Section 5, with the main focus set on the physical interpretation of the predictors. Section 6 contains concluding remarks.

2. Data

The study region in China is the catchment of the Poyang Lake, a sub-catchment of the Yangtze River, located in the Jiangxi province. This region roughly extends from 114°E to 119°E longitude and from 26°N to 30°N latitude. Thirteen rain gauge stations are available, which are located at altitudes ranging from 30 to 144 m (Fig. 1). Annual precipitation amounts vary from 1435 to 1850 mm with 22–29% occurring in the major rain season during June and July, which is associated with the Meiyu rain belt. Therefore, the focus of this study is set on this season. Daily precipitation totals from the 13 stations are available from 1960 to 1999.

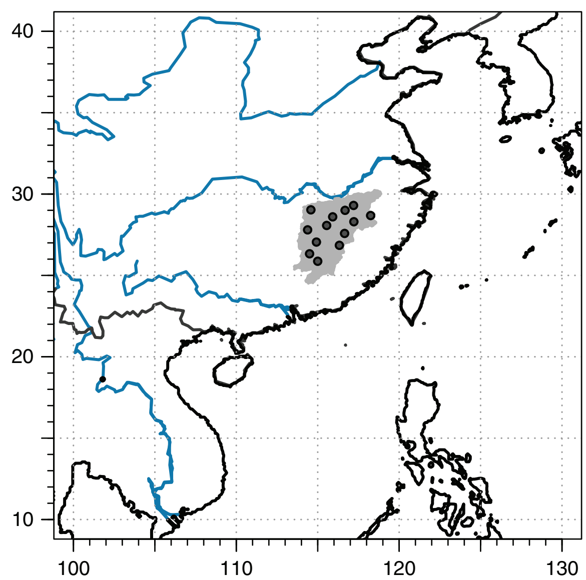

Fig. 1. Location of the Poyang catchment (light grey area) and the 13 rain gauges (dark grey points) in China.

To link observed precipitation to different atmospheric properties, the ERA-40 re-analysis, with the resolution of 1,875° × 1,875°, is chosen (Uppala et al., 2005). According to Skamarock (2004) and Bierdel et al. (2012), covariates of the statistical model should be related to atmospheric dynamics on larger scales than the grid resolution of ERA-40. Therefore, a region of ERA-40 has been selected that envelopes the Poyang catchment spaciously. The corners of the envelope are 10°N, 100°E, 40°N and 130°E. The Poyang catchment is not at the centre of this region, which is slightly shifted to the southwest as atmospheric disturbances are anticipated to develop in the southwest before they propagate parallel to the Yangtze valley. The ERA-40 output is taken for the same period (1960–1999) as station data is available. The following abbreviations will be used for the output variables: UV850 – horizontal windfield at 850 hPa, W500 – vertical velocity in pressure coordinates at 500 hPa, TCW – total column water content, Vo850 – relative vorticity at 850 hPa. The physical motivation for this pre-selection of the variables is given in the results section.

3. Methods

One aim of this study is to set up a statistical model for the probability of rainfall threshold exceedance at rain gauges depending on large-scale predictors. To this end, the rainfall observations are transformed to binary time series via

$$y = \begin{cases} 0 & R_{24h} \leq u \\ 1 & R_{24h} > u, \end{cases} \tag{1}$$

where R_{24h} is the locally observed 24 h accumulated rainfall and u denotes the threshold. For the region of interest – the Poyang catchment in China – the thresholds $u = \{1,5,10,25,50\}$[mm] lead to reasonable exceedance rates (Fig. 2).

To this end the ERA-40 output for the selected area is processed by emperical orthogonal function (EOF) analysis (Hannachi et al., 2007). To account for cross-correlations between the different variables, the fields of different variables are combined as input to the EOF analysis, i.e. our data vectors have the spatial dimension $n_x \times n_y \times n_v$, where $n_x = n_y = 16$ is the number of grid boxes in the x and y direction and n_v is the number of variables, which depends on how many variables are combined (cf. Fig. 3). To take account of different units for different variables, each variable is scaled by its standard deviation, calculated simultaneously over space and time. The resulting EOFs have the same length and contain sub-vectors with spatial patterns for each variable. As EOF analysis is a purely statistical construct, it does not necessarily result in physically meaningful patterns (e.g. Dommenget and Latif, 2002). In addition to EOFs, varimax rotated EOFs (vEOFs) are used as predictors. Basically, the varimax

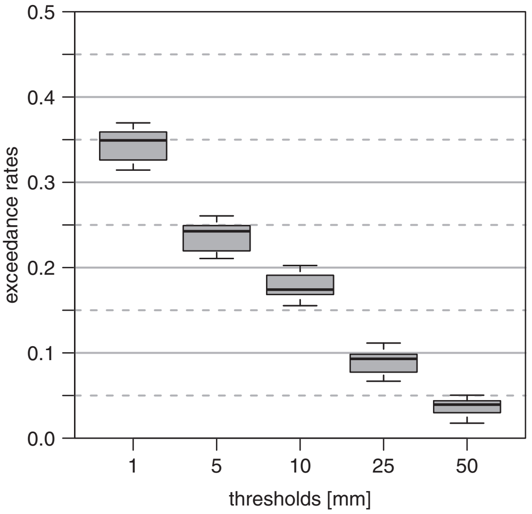

Fig. 2. Climatological exceedance rates conditional on the different thresholds. Each box contains the expectation values E(y) for the 13 stations.

rotation provides more localised patterns than the EOF analysis and avoids the generation of high-order multi-poles. The varimax rotation was performed in such way that, the spatial patterns are no longer orthogonal, but the coefficient time series are uncorrelated, which is also the case for the EOFs. Another characteristic of both methods is that the principal components or EOF/vEOF amplitudes tend to be normally distributed. A comprehensive overview of multivariate statistical techniques can be found in Wilks (2011) and Von Storch and Zwiers (2002). Deeper insights into EOFs are given by Jolliffe (2002).

To combine the binary time series of rainfall events above a given threshold [eq. (1)] with the EOF/vEOF

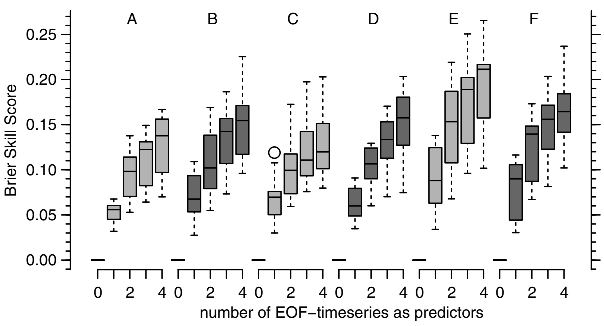

Fig. 3. Comparison of different setups for the EOF analysis and the subsequent forward regression. Each box-whisker-plot shows the distribution of the Brier skill score over all stations in the catchment. These results are based on a threshold of u = 25 mm. The letters refer to the different input sets: A – UV850, B – W500, C – TCW, D – Vo850, E – Vo850 and W500, F – Vo850 and W500 and TCW. Note: The boxes are grey shaded only for visual convenience.

patterns, a *logistic regression* is applied, which assumes that the events are drawn from a Bernoulli-distributed random variable $Y \in \{y=0,\ y=1\}$ and $Y \sim \mathrm{Be}(p) = p^y(1-p)^{1-y}$. Here, p is the exceedance probability of the rainfall event. The logistic regression assumes a linear model between the logit transformed exceedance probability p and the predictor values,

$$\log\left(\frac{p_i}{1-p_i}\right) = \beta_0 + \sum_{j=1}^{m} x_{ij}\beta_j, \tag{2}$$

where p_i denotes the probability of threshold exceedance, $x_{i1},\ldots,x_{im}$ the predictor time-series and $\beta_0,\beta_1,\ldots,\beta_m$ the model parameters. The log-likelihood for a Bernoulli-distributed random variable is expressed by

$$l(p;y) = \sum_{i=1}^{n}\left[y_i \log\left(\frac{p_i}{1-p_i}\right) + \log(1-p_i)\right] \tag{3}$$

in combination with eq. (2) (McCullagh and Nelder, 1989, chap. 4). The estimation of the model parameters $\beta_0,\beta_1,\ldots,\beta_m$ is performed by the R function glm() (R Development Core Team, 2011), as the logistic regression is a special case of a *generalised linear model* (GLM).

As the decomposition techniques (EOF and vEOF) still generate an awkward number of effective modes (Bretherton et al., 1999, eq. 4), a selection of covariates has to be performed in order to avoid over-fitting. This selection is divided into two parts. In the first part a forward selection is performed. Each pool of potential predictors includes principal components of one EOF or vEOF analysis. At each step, the best yet unselected covariate maximising the log-likelihood is added until no further covariates remain. As the second part of the selection, a stopping rule for the predictor chain has to be found. This is achieved by testing each model on a set of independent data via cross-validation. The predictor chain would be truncated at the point where the skill of the model does not increase with the addition of more predictors (Wilks, 2011, chap. 7.4). More details of the application of the stopping rules are given further on.

To avoid conflicts with temporal autocorrelations of the EASM, a four-fold cross-validation (Michaelsen, 1987; Efron and Tibshirani, 1993) is performed with four sets with 30 yr training periods and one decade for verification. This timescale is chosen as the EASM is strongly linked to ENSO varying with a period of 3–7 yr (Neelin et al., 1998; Wang et al., 2000). The cross-validation includes the following steps: a) EOF analysis of ERA-40 data for the training period, b) forward regression via log-likelihood to determine the order of the covariates, c) calculation of skill scores from the independent part of the data, and d) averaging the skill scores over the four verification decades.

This strategy does not only validate the statistical model itself but also the derivation of the predictor time-series by EOF analysis (Von Storch and Zwiers, 2002; Hastie et al., 2008).

In the following sections, the goodness of the models is expressed by the Brier skill score (BSS) (Brier, 1950; Gneiting et al., 2007)

$$BSS = 1 - \frac{BS}{BS_{ref}}, \quad \text{with} \quad BS = \frac{1}{n}\sum_{i=1}^{n}(p_i - y_i)^2, \qquad (4)$$

where BS_{ref} is the Brier score of the climatology $E(y)$. In addition, as the probability of exceeding the 90% quantile (cf. Fig. 2) is modelled, the *Winkler score* is applied (Winkler, 1994; Gneiting et al., 2007),

$$WS = \frac{1}{n}\sum_{i=1}^{n}\frac{(c - y_i)^2 - (p_i - y_i)^2}{(c - H(p_i - c))^2}, \qquad (5)$$

where H is a heavyside function, which is zero for $p_i \leq c$ and one for $p_i > c$. The value of $c \in (0,1)$ works as a reference probability. The WS is an asymmetric scoring rule and serves as an additional verification for models, for which the climatological exceedance rate is far away from $E(y) = 0.5$ (cf. Fig. 2). Note that eq. (5) shows a special case of the WS derived from the BS. In general, the WS could also be derived from any other score. As a reference for the scoring rules, the mean probability over the training period ("climate") is chosen (Fig. 2). All scoring rules applied in this study are *strictly proper scoring rules*, which means that the scoring rule is maximised if and only if the forecast equals the observation (Gneiting et al., 2007).

For a more detailed validation of a statistical model the reliability diagram is calculated, which exhibits the joint distribution of forecast and observation via calibration-refinement factorisation. For each pre-defined forecast probability $p_k = \{0.05, 0.15, \ldots, 0.95\}$, both the conditional probability that an event has been observed $\Pr(y = 1|p_k)$ and the relative frequency of a forecast probability $\Pr(p_k)$ are calculated. The conditional probability and the relative frequency are called calibration curve and refinement curve, respectively. The calibration curve of a perfectly calibrated model lies exactly on the diagonal. The model has a high confidence, if the refinement curve exhibits a

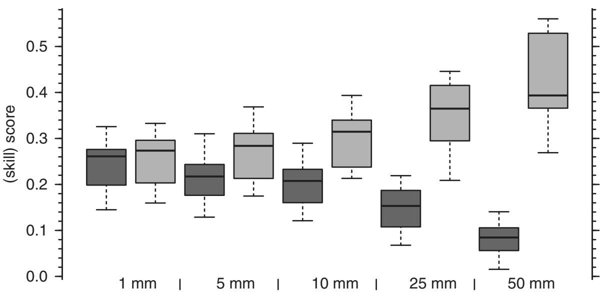

Fig. 4. Comparison of the symmetric Brier skill score (dark grey shaded boxes) and the asymmetric Winkler skill score (light grey shaded boxes) conditioned on the different thresholds. Each box-whisker-plot shows the distribution of one skill score over all stations in the catchment. The first and the third EOF mode of the set Vo850 and W500 were used as predictors.

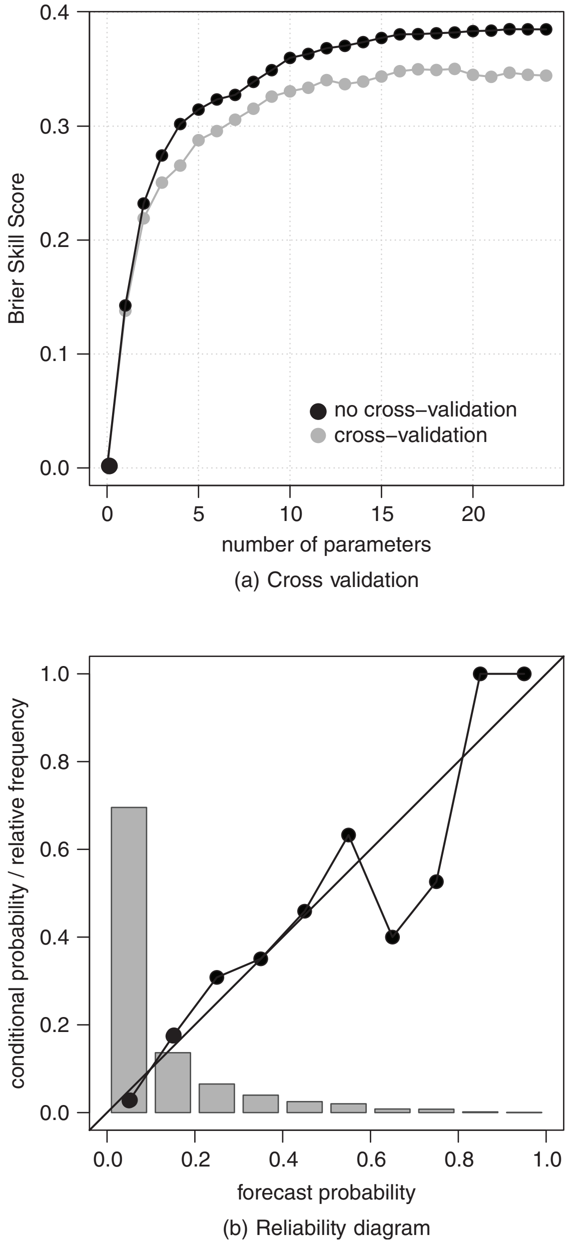

Fig. 5. Validation of the probability of threshold exceedance model with Vo850 and W500 as input variables of the EOF analysis. The predicted was calculated from the precipitation observations at Yushan (No. 58634) with the threshold $u = 25$ mm [cf. eq. (1)].

U-shape. That means, very low and very high probabilities are predicted in the majority of cases (Wilks, 2011).

4. Results

Different sets of ERA-40 output variables are compared as input for the downscaling procedure, i.e. the EOF analysis and the forward regression. The variables are either well known for describing monsoon dynamics on the seasonal timescale [UV850 cf. Wang and Fan (1999)] or typical variables for downscaling precipitation [W500, TCW, Vo850 cf. Friederichs and Hense (2007)]. To consider cross-correlations between variables, they are combined as input for the EOF analysis. The resulting principal components are also tested as predictors for the logistic regression. It was found that a combination of Vo850 and W500 performs best while no gain in skill is achieved by adding TCW to the set (Fig. 3). Models with no predictors lead automatically to the climatological exceedance rates (Fig. 2) and therefore result in zero skill. Not all tested combinations are shown in Fig. 3.

To gain more insight into the (skill) scores conditioned on the chosen threshold, the dependence of both the symmetric BSS and the asymmetric WS on the threshold is shown in Fig. 4. Each boxplot exhibits the distribution of (skill) scores over the 13 stations in the Poyang catchment after performing the cross-validation. Two predictors of the common EOF analysis of the variables Vo850 and W500 are used as covariates (more details on the selection are given in the next paragraph). Therefore, the BSS boxplot for $u = 25$ mm in Fig. 4 is equal to the boxplot with two predictors of group E in Fig. 3. The BSS decreases for higher thresholds as low-probability events are considered at high thresholds (Fig. 2). In contrast, the WS increases for higher thresholds, because it accounts for the asymmetric character of the response time series with high thresholds. Note, all models in this figure are significant at a 1% level with respect to climatology, which was checked by a likelihood-ratio test.

Two aspects of the cross-validation are analysed in detail: The effect of adding predictors to a statistical model and the spread of skill and reliability resulting from the cross-validation method. The results, shown in Fig. 5, refer to the station at Yushan (No. 58634) and a threshold of $u = 25$ mm. The skill increases with increasing numbers of predictors (Fig. 5a). The maximum in the cross-validation curve, from which a truncation criterion for the predictor chain would be expected, occurs between 15 and 20 predictors. However, the strong increments of the first two selected predictors, referring to the 1st and 3rd EOF, show the major relevance of these patterns in terms of precipitation exceeding a specified threshold. The ongoing improvement of skill indicates that not all relevant processes for rainfall events can be reduced to a small number of modes. A further and even stronger indication for the major relevance of these two modes and a truncation of the predictor chain after these modes is that the 1st and 3rd EOF are selected first during the forward regression for nearly all stations in the catchment (Table 1) and thresholds (not shown). The reliability diagram (Fig. 5b) for the model with the 1st and 3rd EOFs as predictors is reasonably good. The calibration curve lies on the diagonal, but exhibits also some over-estimation of the model conditioned on the forecast probability $0.6 < p_k < 0.8$. The refinement curve shows that the forecast probability lies between 0 and 0.1 in the majority of cases, but lacks a peak in the box for the highest forecast probabilities.

The spatial patterns of the modes with major relevance in the statistical analysis can be related to EASM dynamics. Figures 6 and 7 show the 1st and 3rd EOF, respectively.

Table 1. Order of selected EOF-predictors for all 13 stations in the Poyang lake catchment. The threshold is set to $u = 25$ mm for all stations

Station name (ID)	Sequence of selected EOF predictors						
Xiushui (57598)	1	3	7	2	14	15	11	–
Yichun (57793)	1	3	10	7	12	13	4	–
Jian (57799)	1	3	20	13	24	12	18	–
Suichuan (57896)	1	3	2	6	11	7	22	–
Ganzhou (57993)	1	6	2	13	3	20	8	–
Poyang (58519)	1	3	7	15	2	5	24	–
Jingdezhen (58527)	1	3	7	15	2	5	10	–
Nanchang (58606)	1	3	7	15	10	9	14	–
Zhangshu (58608)	1	3	15	7	12	17	10	–
Guixi (58626)	1	3	15	4	20	7	22	–
Yushan (58634)	1	3	15	24	14	13	7	–
Nancheng (58715)	1	3	15	12	4	20	24	–
Guangchang (58813)	1	3	13	2	20	12	6	–

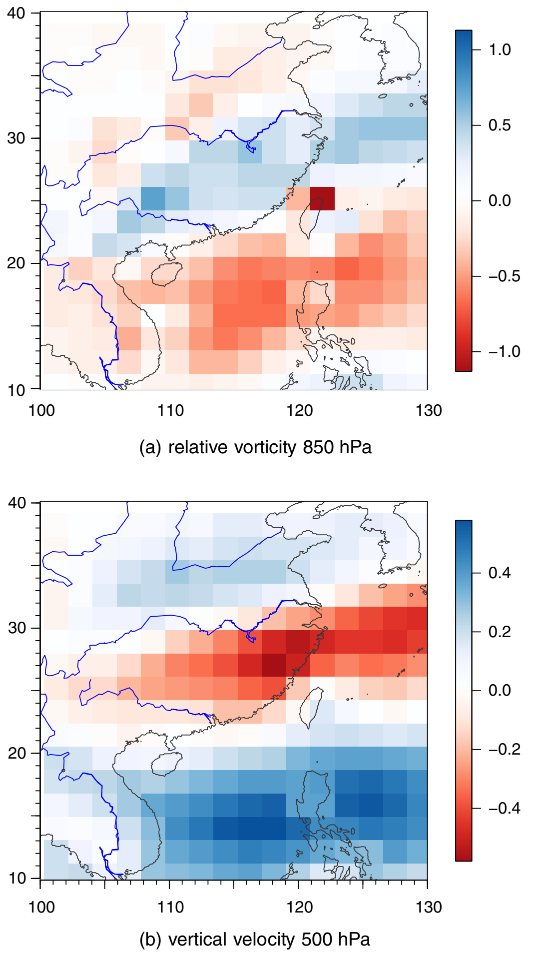

Fig. 6. The first EOF mode of ERA-40 output variables relative vorticity at 850 hPa and vertical velocity at 500 hPa. Explained variance 8.3%.

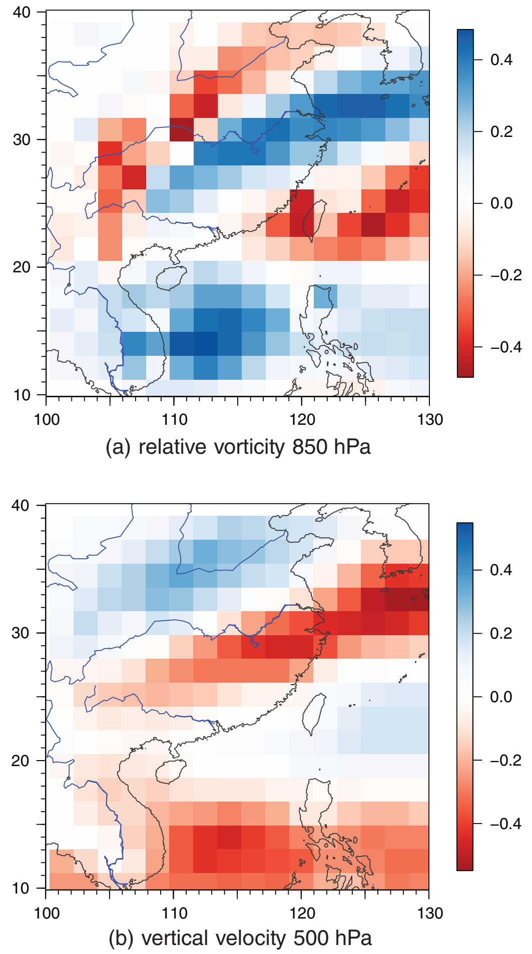

Fig. 7. The third EOF mode of ERA-40 output variables relative vorticity at 850 hPa and vertical velocity at 500 hPa. Explained variance 4.4%.

These modes were selected for all stations as first and second predictor with only one exception (Table 1). For the station in Ganzhou (No. 57993), the 6th mode was selected as second predictor. Furthermore, these two predictors led to the strongest increase of the scores (Fig. 5a). The vertical velocity field of the 1st EOF exhibits a strong pole over the Yangtze valley extending to the adjacent sea. The sign convention is chosen such that a negative spatial amplitude combined with a positive temporal amplitude indicates rising motion. Similarly located is a band of positive relative vorticity that is through the same sign convention associated to cyclonic disturbances. Rising motion and cyclonic disturbances are typical synoptic features of SW vortices as described in the introduction. However, there is a strong counter-pole in both fields over the SCS. Though this counter-pole is part of the 1st EOF, neither the relative vorticity nor the vertical velocity over the SCS can be associated with any process related to the EASM.

The 3rd EOF (Fig. 7) exhibits a composition of vertical velocity and relative vorticity over the Yangtze valley similar to the 1st EOF, but with a slightly different angle of its main axis. This belt is also located over the Yangtze valley, but its extension partly covers Southern Korea. It has more southwest to northeast direction in contrast to the belt in the 1st EOF, which is almost W–E aligned and does not cover Southern Korea. Furthermore, the pole in the 3rd EOF extends to a horseshoe-like pattern further south into the SCS. The horseshoe appears for both Vo850 (blue) and W500 (red).

Figure 8 shows the model response to the predictors derived from ERA-40 from the year 1998. This year is particularly interesting as a great flood occurred along the Yangtze River (Zong and Chen, 2000). The models for the different thresholds were trained on the period from 1960 to 1989. The good performance of the model – and with it the quality of the predictors – is obvious. As the same

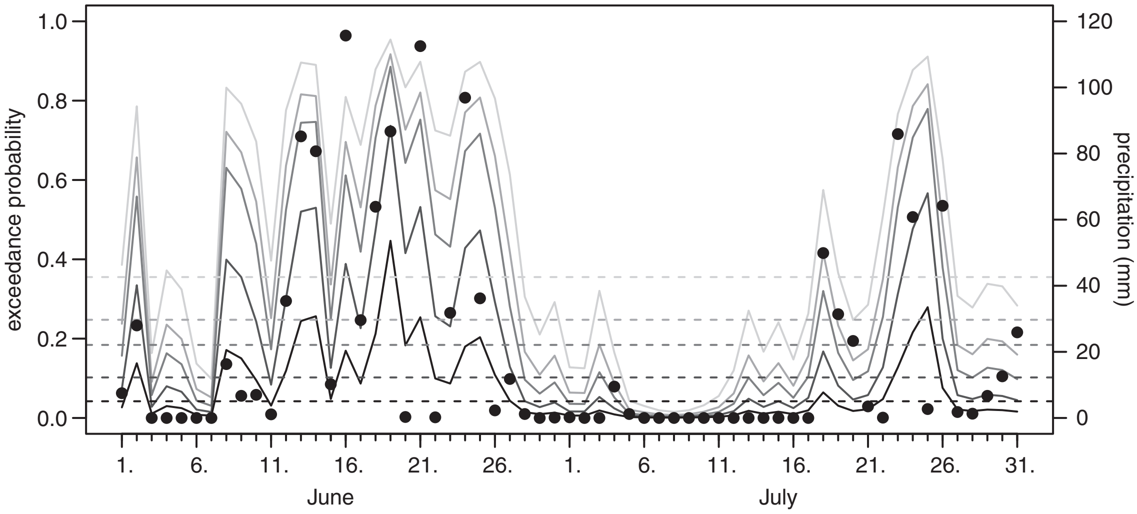

Fig. 8. Example application of the statistical model with EOF predictors for the rain gauge at Yushan (No. 58634). The training period is from 1960 to 1989. The model is applied to 1998. Dashed lines denote climatological exceedance probabilities. Solid lines denote modelled exceedance probabilities. The intensity of the lines stands for the different thresholds, from light to dark $u = \{1,5,10,25,50\}$ (mm). The dots show the observed precipitation at the rain gauge.

predictors were used for the model with different thresholds, no artificial crossing of the predicted probability curves occurs.

The varimax rotation of the first 25 EOF patterns leads to another decomposition of the data. The first 25 patterns were passed to the rotation, because that is the number of effective modes of the corresponding EOFs (Bretherton et al., 1999, derived by eq. 4). Again a forward selection is applied. Fig. 9 exhibits the BSS dependent on the number of predictors in the order that was determined by the forward selection. In contrast to the result of the forward regression with the EOF predictors, only one predictor with major impact can be found. The second vEOF mode was selected as first covariate throughout the stations, before the forward selection starts picking covariates in an arbitrary order that leads only to small increases in skill. The reliability curve correspond to the logistic model with one rotated EOF-predictor (Fig. 9b). The calibration curve exhibits a slight over-estimation for forecast probabilities greater than 0.4. Like the refinement curve of the EOF model (Fig. 5), the refinement curve of the varimax model lacks a peak for high forecast probabilities. However, overall the reliability diagram looks reasonable good.

The spatial pattern of the selected varimax mode display the already described relation between vertical velocity on 500 hPa and relative vorticity at 850 hPa (Fig. 10). The pattern is similar to the structure of the 1st EOF, but with the extension to the east less pronounced. However, the counter-pole over the SCS has vanished. Therefore, the spatial structure is more interpretable in a synoptic sense (cf. Discussion).

5. Discussion

With the combination of rising motion (W500) and cyclonic disturbances (Vo850) on the meso-α-scale, both EOF predictors (Figs. 6 and 7) and the varimax predictor (Fig. 10) are consistent with the concept of SWVs discussed above. As SWVs propagate along different paths through East China, the orientation of the main axis of the Meiyu rain belt vary also. However, the main axis of each predictor pattern coincides with potential paths of the vortices and therefore with the location of the Meiyu rain belt (Ding and Chan, 2005; Wang, 2006). The SWVs develop over the southwestern part of the Tibetan plateau forced by enhanced radiative input. Afterwards, the vortices travel within the Meiyu belt often causing heavy rainfall events.

Relative vorticity and vertical velocity refer to geostrophic and ageostrophic processes, respectively. The statistical link found between both dynamical patterns and local precipitation comes with a physical meaning. Locally available precipitable water is not sufficient for the generation of heavy rainfall events (Trenberth et al., 2003). Therefore, other processes acting on a specific time scale have to play a crucial role for their generation. One of these important processes for heavy precipitation events in the Poyang catchment are the SW vortices. This relation is made clear by the performance of statistical models linking observed precipitation occurrence and predictors that quantify the strength of SW vortices.

The SWVs can also be found in the horizontal windfield at 850 hPa (UV850) by analysing single events (cf. Supplementary Material). However, it was not possible to

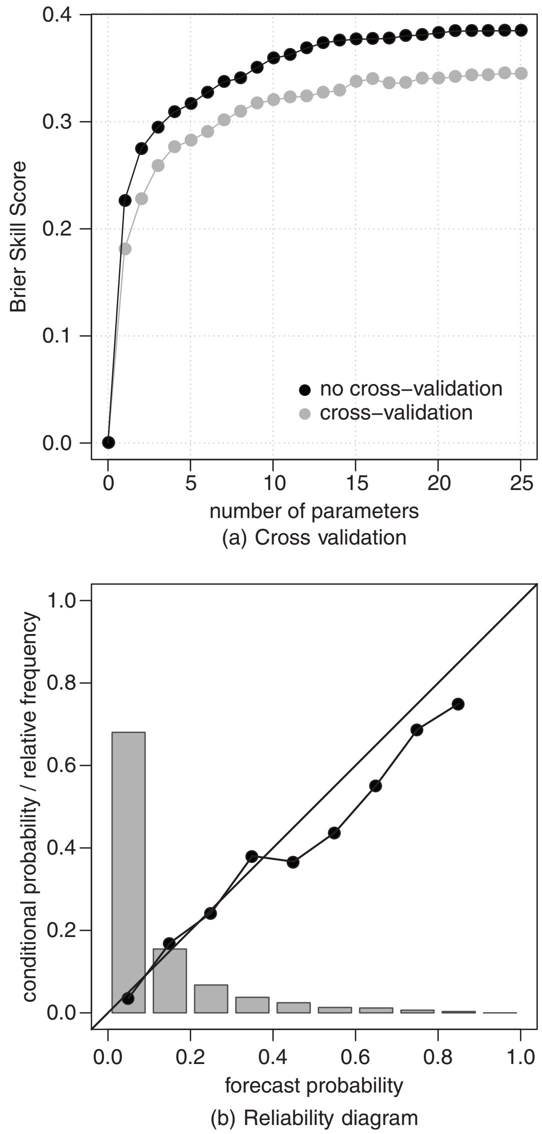

Fig. 9. Validation of the probability of threshold exceedance model, same as in Fig. 5, but with Vo850 and W500 as input variables of the VARIMAX rotated EOF analysis. The predicted was calculated from the precipitation observations at Yushan (No. 58634) with the threshold $u = 25$ mm [cf. eq. (1)].

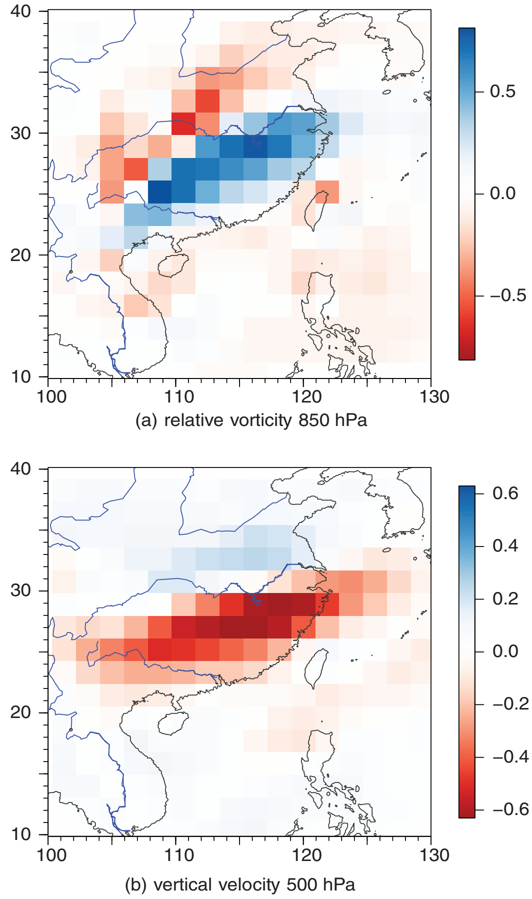

Fig. 10. The second vEOF mode of ERA-40 output variables relative vorticity at 850 hPa and vertical velocity at 500 hPa. Explained variance 6.3%.

extract a SWV-like pattern from UV850 by an EOF analysis. The leading EOF mode of UV850 (explained variance of 23.3%) is related to the suptropical high over the western North Pacific and therefore similar to the index of Wang and Fan (1999).

In order to verify the physical meaning of the spatial pattern introduced above, a simple box correlation analysis is applied [cf. Dommenget and Latif (2002)]. The vertical velocity is averaged for the grid boxes covering the Poyang catchment. This area is highlighted by a box in Fig. 11b. The gridpoint-wise correlations of relative vorticity on 850 hPa and vertical velocity on 500 hPa (Fig. 11) exhibit nearly the same pattern as the varimax predictor with a correlation of -0.88 between both patterns. (Note: By construction the sign of the varimax pattern is arbitrary. Therefore, the sign of the correlation is unimportant.) This finding supports the hypothesis that varimax pattern can be linked to the synoptical processes driving (heavy) precipitation events in the Poyang catchment.

What is the drawback of the varimax predictor model, despite its higher physical relevance? After all, the skill score for the one varimax predictor model is slightly less than for the two EOF predictor model. The EASM is a complex system. A model including too many simplifications – like the reduction to one predictor – might not supply enough degrees of freedom to cope with the high dimensionality of the system.

In the end, it comes down to a trade-off between amplitude (rotated EOF) and variability (EOF). A single predictor can only account for variations in the strength of the pattern. This works well with the varimax pattern

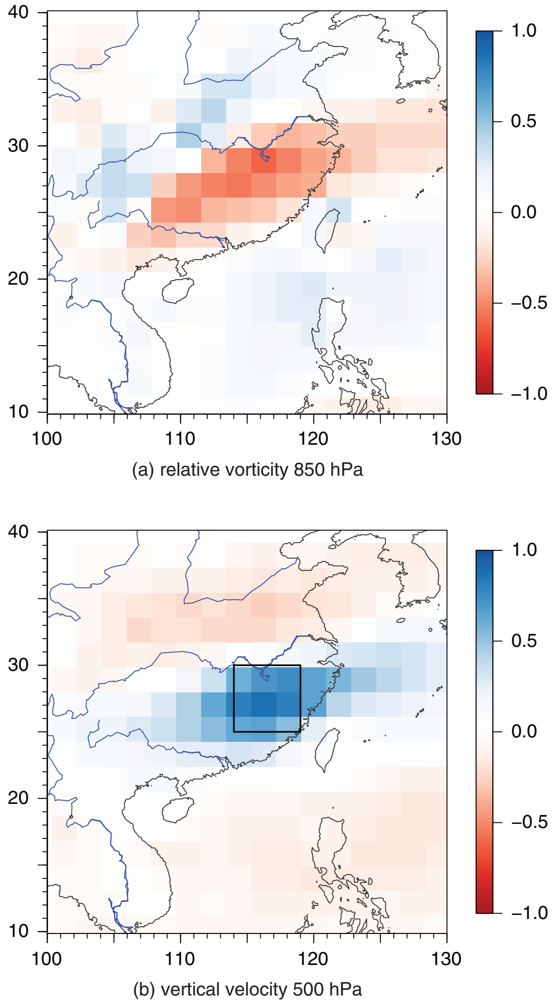

Fig. 11. Gridpoint-wise correlation to the averaged vertical velocity over Poyang (box).

(Fig. 10), as it represents an isolated process. However, a single predictor cannot consider more complex variations like a tilt in the main axis of the rain belt. This variability of the Meiyu belt, which can extend over East Asia with a nearly W–E direction or can be tilted further North in its eastward extension, is described in detail by Ding and Chan (2005). The linear combination of the two EOF patterns (Figs. 6 and 7) can account for such variability as the two convection belts in the EOFs exhibit different angles.

As a conclusion, each of the predictor set comes with its own benefits and drawbacks. This conclusion is corroborated by the correlation between the linear predictor [the right hand side of eq. (2)] of both sets, which does not exceed 0.55. There is a subset for which one method outperforms the other and vice versa: The EOF set is able to cope with the variability of the main axis of the Meiyu belt, but gets disturbed by structures over the SCS, which cannot be associated to processes causing precipitation over the Yangtze valley. Instead, the varimax pattern can be fully interpreted in terms of Meiyu dynamics, but is unable to account for the high dimensional variability in the pattern.

In an application, one would probably neglect the differences in physical interpretation between EOF and rotated EOF predictors and truncate the predictor chain when it reaches its maximum in skill. Note, that if the leading 25 principal components are used as predictors for a model, the skill of the model would be equal to the skill of a model with the 25 modes of the corresponding varimax set. However, one aspect of this study was to show how the physical meaning of the leading predictors depends on the underlying method (EOF vs. rotated EOF). Furthermore, in some applications one might want to keep the physical meaning in order make the application interpretable in terms of EASM dynamics on daily scale.

6. Conclusion

A variety of downscaling techniques have been introduced over the last two decades (e.g. Wilby et al., 1998; Benestad, 2004; Friederichs and Hense, 2007; Vrac and Naveau, 2007). It is now up to the climate research community to select physically meaningful predictors (Maraun et al., 2010; Wilks, 2011). This study presents spatial patterns to explain the dynamics of the EASM on the daily scale. Furthermore, a statistical model for the probability of local precipitation exceeding a certain threshold was set up, taking advantage of these predictors. A cross-validation experiment is performed to verify the overall downscaling scheme – not only the relation between the response and the predictor, but also the generation of the predictor time series, which is the identification of atmospheric processes in the re-analysis output.

It is shown that downscaling procedures should not be treated like a black box, but still require a sensitive analysis of the single steps: Quality assurance of observational data, model selection and predictor selection. This paper discusses two strategies for the latter step. EOF analysis and varimax rotation of the EOF patterns were used to extract predictors from re-analysis output. Though both techniques lead to skilful predictors, the physical meaning of the patterns with major relevance differs from one to the other technique. The EOFs can account for variability of the direction of the Meiyu belt. In contrast, the time series corresponding to the varimax pattern represents the amplitude of an isolated process.

The method presented can be extended to any downscaling of binary events. This can be either a direct binary event like specific complex atmospheric phenomena, which have been observed or not, such as the transition of tropical depressions into tropical cyclones. Similar as in our presentation, any continuous variable can be transferred to a binary time series by applying a threshold. Hereby, the threshold does not necessarily agree with a high quantile, but it can be set to any other user relevant level such as above/below normal, which is important in seasonal forecasting. Even the forecasting of non-meteorological events like the occurrence of certain phenological phases, e.g. the flowering of cherry trees on a specific day in spring, can be treated through logistic regression in combination with pattern-based covariates to predict the event.

7. Acknowledgments

The authors gratefully acknowledge two anonymous reviewers. Their accurate and thorough comments were most helpful in improving the manuscript. This work was funded by the NSFC/DFG-joint funding programme *Land Use and Water Resources Management under Changing Environmental Conditions* (NSFC project number: 40911130506). T. Simon would like to thank the GSP members around Steve Sain and Doug Nychka for fruitful discussions during his visit at the NCAR, which was supported by the CISL visitor programme RSVP.

References

Bachner, S., Kapala, A. and Simmer, C. 2008. Evaluation of daily precipitation characteristics in the clm and their sensitivity to parameterizations. *Meteorolo Z*. **17**(4), 407–419.

Benestad, R. 2004. Empirical-statistical downscaling in climate modeling. *Eos*. **85**(42), 417.

Benestad, R., Nychka, D. and Mearns, L. 2012. Specification of wet-day daily rainfall quantiles from the mean value. *Tellus A*. **64**, 14981. DOI: 10.3402/tellusa.v64i0.14981.

Bentzien, S. and Friederichs, P. 2012. Generating and calibrating probabilistic quantitative precipitation forecasts from the high-resolution nwp model cosmo-de. *Weather Forecast*. **27**, 988–1002.

Bierdel, L., Friederichs, P. and Bentzien, S. 2012. Spatial kinetic energy spectra in the convection-permitting limited-area nwp model cosmo-de. *Meteorol Z*. **21**, 245–258.

Bremnes, J. 2004. Probabilistic forecasts of precipitation in terms of quantiles using nwp model output. *Mon. Weather. Rev.* **132**(1), 338–347.

Bretherton, C., Widmann, M., Dymnikov, V., Wallace, J. and Bladé, I. 1999. The effective number of spatial degrees of freedom of a time-varying field. *J. Climate*. **12**(7), 1990–2009.

Brier, G. 1950. Verification of forecasts expressed in terms of probability. *Mon. Weather. Rev.* **78**(1), 1–3.

Chang, C. 2004. *East Asian Monsoon*. Vol. 2. World Scientific, Singapore.

Chang, C., Yi, L. and Chen, G. 2000. A numerical simulation of vortex development during the 1992 East Asian summer monsoon onset using the navy's regional model. *Mon. Weather. Rev.* **128**(6), 1604–1631.

Chen, S. and Dell'Osso, L. 1984. Numerical prediction of the heavy rainfall vortex over eastern Asia monsoon region. *J. Meteorol. Soc. Jpn*. **62**(5), 730–747.

Cooley, D., Nychka, D. and Naveau, P. 2007. Bayesian spatial modeling of extreme precipitation return levels. *J. Am. Stat. Assoc.* **102**(479), 824–840.

Ding, Y. and Chan, J. 2005. The East Asian summer monsoon: an overview. *Meteorol. Atmos. Phys*. **89**(1), 117–142.

Ding, Y., Zhang, Y., Ma, Q. and Hu, G. 2001. Analysis of the large-scale circulation features and synoptic systems in East Asia during the intensive observation period of game/hubex. *J. Meteorol. Soc. Jpn*. **79**(1B), 277–300.

Dommenget, D. and Latif, M. 2002. A cautionary note on the interpretation of EOFs. *J. Climate*. **15**(2), 216–225.

Ebell, K., Bachner, S., Kapala, A. and Simmer, C. 2008. Sensitivity of summer precipitation simulated by the clm with respect to initial and boundary conditions. *Meteorol. Z*. **17**(4), 421–431.

Efron, B. and Tibshirani, R. 1993. *An Introduction to the Bootstrap*. Vol. 57. Chapman & Hall/CRC, London.

Frei, C., Schöll, R., Fukutome, S., Schmidli, J. and Vidale, P. 2006. Future change of precipitation extremes in Europe: Intercomparison of scenarios from regional climate models. *J. Geophys. Res*. **111**(D6), D06105.

Friederichs, P. and Hense, A. 2007. Statistical downscaling of extreme precipitation events using censored quantile regression. *Mon. Weather Rev*. **135**(6), 2365–2378.

Gao, X., Shi, Y., Song, R., Giorgi, F., Wang, Y. and co-authors. 2008. Reduction of future monsoon precipitation over China: Comparison between a high resolution rcm simulation and the driving gcm. *Meteorol. Atmos. Phys*. **100**(1), 73–86.

Gneiting, T., Balabdaoui, F. and Raftery, A. 2007. Probabilistic forecasts, calibration and sharpness. *J. Roy. Stat. Soc. B* **69**(2), 243–268.

Guo, Q. 1983. The summer monsoon index in East Asia and its variation (in Chinese). *Acta Geogr Sin*. **38**, 208–217.

Hannachi, A., Jolliffe, I. and Stephenson, D. 2007. Empirical orthogonal functions and related techniques in atmospheric science: a review. *Int. J. Climatol*. **27**(9), 1119–1152.

Hastie, T., Tibshirani, R. and Friedman, J. 2008. *The Elements of Statistical Learning*. 2nd ed. Springer, Series in Statistics, Berlin.

Jolliffe, I. 2002. *Principal Component Analysis*. 3rd ed. Springer, Series in Statistics, New York.

Kron, W. 2009. Flood insurance: from clients to global financial markets. *J. Flood Risk Manage*. **2**(1), 68–75.

Kuo, Y., Cheng, L. and Bao, J. 1988. Numerical simulation of the 1981 Sichuan flood: Part i. evolution of a mesoscale southwest vortex. *Mon. Weather Rev*. **116**(12), 2481–2504.

Li, J. and Zeng, Q. 2002. A unified monsoon index. *Geophys res lett*. **29**(8), 115–1.

Lindau, R. and Simmer, C. 2013. On correcting precipitation as simulated by the regional climate model cosmo-clm with daily rain gauge observations. *Meteorol. Atmos. Phys*. **119**, 31–42.

Maraun, D., Wetterhall, F., Ireson, A., Chandler, R., Kendon, E. and co-authors. 2010. Precipitation downscaling under climate change: recent developments to bridge the gap between dynamical models and the end user. *Rev. Geophys.* **48**(3), RG3003.

McCullagh, P. and Nelder, J. 1989. *Generalized Linear Models*. Chapman & Hall/CRC, London.

Mesinger, F. and Veljovic, K. 2013. Limited area nwp and regional climate modeling: a test of the relaxation vs eta lateral boundary conditions. *Meteorol. Atmos. Phys.* **119**, 1–16.

Michaelsen, J. 1987. Cross-validation in statistical climate forecast models. *J. Clim. Appl. Meteorol.* **26**(11), 1589–1600.

Murphy, J. 1999. An evaluation of statistical and dynamical techniques for downscaling local climate. *J. Climate.* **12**(8), 2256–2284.

Neelin, J., Battisti, D., Hirst, A., Jin, F., Wakata, Y. and co-authors. 1998. Enso theory. *J. Geophys. Res.* **103**(C7), 14261–14290.

Orlowsky, B., Bothe, O., Fraedrich, K., Gerstengarbe, F. and Zhu, X. 2010. Future climates from bias-bootstrapped weather analogs: An application to the Yangtze river basin. *J. Climate.* **23**(13), 3509–3524.

Park, E., Hong, S. and Kang, H. 2008. Characteristics of an east–Asian summer monsoon climatology simulated by the regcm3. *Meteorol. Atmos. Phys.* **100**(1), 139–158.

Piao, S., Ciais, P., Huang, Y., Shen, Z., Peng, S. and co-authors. 2010. The impacts of climate change on water resources and agriculture in China. *Nature* **467**(7311), 43–51.

R Development Core Team. 2011. R foundation for statistical computing. Vienna, Austria. ISBN 3-900051-07-0. Online at: http://www.R-project.org

Roeckner, E. 2003. The atmospheric general circulation model ECHAM 5. Part 1: model description. Max-Plank-Institut für Meteorologie, Report 349, 127 pp.

Schölzel, C. and Hense, A. 2011. Probabilistic assessment of regional climate change in southwest Germany by ensemble dressing. *Clim. Dynam.* **36**(9), 2003–2014.

Skamarock, W. 2004. Evaluating mesoscale nwp models using kinetic energy spectra. *Mon. Weather Rev.* **132**(12), 3019–3032.

Tao, S. and Ding, Y. 1981. Observational evidence of the influence of the Qinghai-Xizang (Tibet) plateau on the occurrence of heavy rain and severe convective storms in China. *B. Am. Meteorol. Soc.* **62**(1), 23–30.

Trenberth, K., Dai, A., Rasmussen, R. and Parsons, D. 2003. The changing character of precipitation. *B. Am. Meteorol. Soc.* **84**(9), 1205–1218.

Uppala, S., Kållberg, P., Simmons, A., Andrae, U., Bechtold, V. and co-authors. 2005. The era-40 re-analysis. *Q. J. Roy. Meteor. Soc.* **131**(612), 2961–3012.

Von Storch, H. and Zwiers, F. 2002. *Statistical Analysis in Climate Research*. Cambridge Univ Pr.

Vrac, M. and Naveau, P. 2007. Stochastic downscaling of precipitation: from dry events to heavy rainfalls. *Water Resour. Res.* **43**, W07402.

Wang, B. 2006. *The Asian Monsoon*. Springer Verlag, Berlin.

Wang, B., Ding, Q., Fu, X., Kang, I., Jin, K. and co-authors. 2005. Fundamental challenge in simulation and prediction of summer monsoon rainfall. *Geophys. Res. Lett.* **32**(15), L15711.

Wang, B. and Fan, Z. 1999. Choice of south Asian summer monsoon indices. *B. Am. Meteorol. Soc.* **80**, 629–638.

Wang, B. and Orlanski, I. 1987. Study of a heavy rain vortex formed over the eastern flank of the Tibetan plateau. *Mon Weather Rev.* **115**(07), 1370–1393.

Wang, B., Wu, R. and Fu, X. 2000. Pacific-East Asian teleconnection: How does enso affect East Asian climate? *J. Climate.* **13**(9), 1517–1536.

Wang, B., Wu, Z., Li, J., Liu, J., Chang, C. and co-authors. 2008. How to measure the strength of the East Asian summer monsoon. *J. Climate.* **21**(17), 4449–4463.

Webster, P. and Yang, S. 1992. Monsoon and ENSO: selectively interactive systems. *Q. J. Roy. Meteor. Soc.* **118**(507), 877–926.

Wilby, R. and Wigley, T. 2000. Precipitation predictors for downscaling: observed and general circulation model relationships. *Int. J. Climatol.* **20**(6), 641–661.

Wilby, R., Wigley, T., Conway, D., Jones, P., Hewitson, B. and co-authors. 1998. Statistical downscaling of general circulation model output: A comparison of methods. *Water Resour. Res.* **34**(11), 2995–3008.

Wilks, D. 2011. *Statistical Methods in the Atmospheric Sciences*. Vol. 100. Academic Press, Boston.

Winkler, R. 1994. Evaluating probabilities: asymmetric scoring rules. *Manage Sci.* **40**, 1395–1405.

Zhai, P., Zhang, X., Wan, H. and Pan, X. 2005. Trends in total precipitation and frequency of daily precipitation extremes over China. *J. Climate.* **18**(7), 1096–1108.

Zhang, Q., Sun, P., Singh, V. and Chen, X. 2012. Spatial-temporal precipitation changes (1956–2000) and their implications for agriculture in China. *Global Planet Change* **82**, 86–95.

Zhao, C., Wang, Y., Yang, Q., Fu, R., Cunnold, D. and co-authors. 2010a. Impact of East Asian summer monsoon on the air quality over China: view from space. *J. Geophys. Res.* **115**, D09301.

Zhao, P., Zhu, Y. and Zhang, Q. 2010b. A summer weather index in the East Asian pressure field and associated atmospheric circulation and rainfall. *Int. J. Climatol.* **32**, 375–386.

Zong, Y. and Chen, X. 2000. The 1998 flood on the Yangtze, China. *Nat. Hazards.* **22**(2), 165–184.

BONNER METEOROLOGISCHE ABHANDLUNGEN

Herausgegeben vom Meteorologischen Institut der Universität Bonn durch Prof. Dr. H. FLOHN (Hefte 1-25), Prof. Dr. M. HANTEL (Hefte 26-35), Prof. Dr. H.-D. SCHILLING (Hefte 36-39), Prof. Dr. H. KRAUS (Hefte 40-49), ab Heft 50 durch Prof. Dr. A. HENSE.

Heft 1-39: siehe `http://www2.meteo.uni-bonn.de/bibliothek/bma.html`

Heft 40: ***Hermann Flohn***: Meteorologie im Übergang Erfahrungen und Erinnerungen (1931-1991). 1992, 81 S. + XII. € 23

Heft 41: ***Adnan Alkhalaf and Helmut Kraus***: Energy Balance Equivalents to the Köppen-Geiger Climatic Regions. 1993, 69 S. + IX. € 19

Heft 42: ***Axel Gabriel***: Analyse stark nichtlinearer Dynamik am Beispiel einer rei- bungsfreien 2D-Bodenkaltfront. 1993, 127 S. + XIV. € 30

Heft 43: ***Annette Münzenberg-St.Denis***: Quasilineare Instabilitätsanalyse und ihre Anwendung auf die Strukturaufklärung von Mesozyklonen im östlichen Weddellmeergebiet. 1994, 131 S. + XIII. € 33

Heft 44: ***Hermann Mächel***: Variabilität der Aktionszentren der bodennahen Zirkulation über dem Atlantik im Zeitraum 1881-1989. 1995, 188 S. + XX. € 48

Heft 45: ***Günther Heinemann***: Polare Mesozyklonen. 1995, 157 S. + XVI. € 46

Heft 46: ***Joachim Klaßen:*** Wechselwirkung der Klima-Subsysteme Atmosphäre, Meereis und Ozean im Bereich einer Weddellmeer-Polynia. 1996, 146 S. + XVI. € 43

Heft 47: ***Kai Born***: Seewindzirkulationen: Numerische Simulationen der Seewind- front. 1996, 170 S. + XVI. € 48

Heft 48: ***Michael Lambrecht***: Numerische Untersuchungen zur tropischen 30-60-tägigen Oszillation mit einem konzeptionellen Modell. 1996, 48 S. + XII. € 15

Heft 49: ***Cäcilia Ewenz***: Seewindfronten in Australien: flugzeuggestützte Messungen und Modellergebnisse. 1999, 93 S. + X. € 30

Heft 50: ***Petra Friederichs***: Interannuelle und dekadische Variabilität der atmosphärischen Zirkulation in gekoppelten und SST-getriebenen GCM-Experimenten. 2000, 133 S. + VIII. € 25

Heft 51: ***Heiko Paeth***: Anthropogene Klimaänderungen auf der Nordhemisphäre und die Rolle der Nordatlantik-Oszillation. 2000, 168 S.+ XVIII. € 28

Heft 52: ***Hildegard Steinhorst***: Statistisch-dynamische Verbundsanalyse von zeitlich und räumlich hoch aufgelösten Niederschlagsmustern: eine Untersuchung am Beispiel der Gebiete von Köln und Bonn. 2000, 146 S. + XIV. € 25

Heft 53: ***Thomas Klein***: Katabatic winds over Greenland and Antartica and their interaction with mesoscale and synoptic-scale weather systems: three-dimensional numerical models. 2000, 146 S. + XIV. € 25

Heft 54: ***Clemens Drüe***: Experimentelle Untersuchung arktischer Grenzschichtfronten an der Meereisgrenze in der Davis-Straße. 2001, 165 S. + VIII. €

Heft 55: ***Gisela Seuffert***: Two approaches to improve the simulation of near surface processes in numerical weather prediction models. 2001, 128 S. + VI. € 25

Heft 56: ***Jochen Stuck***: Die simulierte axiale atmosphärische Drehimpulsbilanz des ECHAM3-T21 GCM. 2002, 202 S. + VII. € 30

Heft 57: ***Günther Haase***: A physical initialization algorithm for non-hydrostatic weather prediction models using radar derived rain rates. 2002, 106S. + IV. € 25

Heft 58: ***Judith Berner***: Detection and Stochastic Modeling of Nonlinear Signatures in the Geopotential Height Field of an Atmospheric General Circulation Model. 2003, 157 S. + VIII. € 28

Heft 59: ***Bernd Maurer***: Messungen in der atmosphärischen Grenzschicht und Validation eines mesoskaligen Atmosphärenmodells über heterogenen Landoberflächen. 2003, 182 S. + IX. € 30

Heft 60: ***Christoph Gebhardt***: Variational reconstruction of Quaternary temperature fields using mixture models as botanical – climatological transfer functions. 2003, 204 S. + VIII. € 30

Heft 61: ***Heiko Paeth***: The climate of tropical and northern Africa – A statistical-dynamical analysis of the key factors in climate variability and the role of human activity in future climate change. 2005, 316 S. + XVI. € 15

Heft 62: ***Christian Schölzel***: Palaeoenvironmental transfer functions in a Bayesian framework with application to Holocene climate variability in the Near East. 2006, 104 S. + VI. € 15

Heft 63: ***Susanne Bachner***: Daily precipitation characteristics simulated by a regional climate model, including their sensitivity to model physics, 2008, 161 S. € 15

Heft 64: ***Michael Weniger***: Stochastic parameterization: a rigorous approach to stochastic three-dimensional primitive equations, 2014, 148 S. + XV. open access[1]

Heft 65: ***Andreas Röpnack***: Bayesian model verification: Predictability of convective conditions based on EPS forecasts and observations, 2014, 152 S. + IV. open access[1]

Heft 66: ***Thorsten Simon***: Statistical and Dynamical Downscaling of Numerical Climate Simulations: Enhancement and Evaluation for East Asia, 2014, 48 S. + LXXVII. open access[1]

[1] Available at `http://hss.ulb.uni-bonn.de/fakultaet/math-nat/`

Meteorologisches Institut
Mathematisch Naturwissenschaftliche Fakultät
Universität Bonn